

© Copyright by Shaowei Song 2019

All Rights Reserved

Nanomaterials to Enhance the Performance of Thermoelectric Materials and Catalysts
for Water Splitting

A Dissertation

Presented to

the Faculty of the Program of Materials Science and Engineering

University of Houston

In Partial Fulfillment

of the Requirement for the Degree

Doctor of Philosophy

In Materials Science and Engineering

By

Shaowei Song

May 2019

Nanomaterials to Enhance the Performance of Thermoelectric Materials and Catalysts for
Water Splitting

Shaowei Song

Approved

Chair of the Committee
Zhifeng Ren, Professor,
Dept. of Physics and TcSUH

Committee members:

Alamgir Karim, Professor,
Dept. of Materials Science and
Engineering

Shuo Chen, Assistant Professor,
Dept. of Physics and TcSUH

Jiming Bao, Associate Professor,
Dept. of Electrical and Computer
Engineering

Paul Ruchhoeft, Associate Professor,
Dept. of Electrical and Computer
Engineering

Suresh Khator, Associate Dean,
Cullen College of Engineering

Alamgir Karim, Program Director,
Materials Science and Engineering

Acknowledgements

I really would like to thank my supervisor Prof. Ren in department of Physics and TcSUH for giving me the opportunity to work in his group and sponsor me for my Ph.D. study. He is not only a mentor for scientific research, and also a guider in my life. He helps me become who I am now. Prof. Ren is always patient, comprehensive and positive to instruct and inspire my study. Whatever the difficulty I encounter in my life or my research, Prof. Ren is always be kind and helpful.

My wife Yaxi Li is always supportive to me in past eleven years. I think I am the luckiest person to have her in my life. She brings happiness and luck to me every day. I really appreciate what she has done. I also want to thank my parents and my litter brother for their unconditional support and love.

I also want to thank Prof. Qingyong Zhang and Prof. Yingrong Jin in Xihua University, who instructed me to earn my master's degree. They lead me to the science research field and enlighten my research interests.

I feel so fortunate to work with these smart people in this wonderful group. I would like to thank my current group member Dr. Jun Mao, Dr. Zhensong Ren, Dr. Dan Luo, Dr. Fei Tian, Dr. Lili Jiang, Dr. Luo Yu, Qing Zhu, Wuyang Ren, Wenyu Zhang, Fanghao Zhang and former group members Dr. Hantian Zhu, Dr. Ran He, Dr. Jing Shuai, Dr. Udara Saparamadu, Dr. Jianfa Chen, Prof. Yumei Wang, Prof. Haiqing Zhou, Dr. Jingying Sun, Dr. Yizhou Ni, Dr. Qing Jie, Dr. Jing Jiang, Ting Zhou and Li You. I want to express my gratitude to Prof. Shuo Chen for her active discussion and kind help in my life. I would like to thank our research professor Dr. Dezhi Wang and our lab manager Hui Wang.

I would like to thank the committee member: Prof. Zhifeng Ren, Prof. Alamgir Karim, Prof. Shuo Chen, Prof. Jiming Bao, and Prof. Paul Ruchhoeft for their kind help during my graduation.

Nanomaterials to Enhance the Performance of Thermoelectric Materials and Catalysts
for Water Splitting

An Abstract

of a

Dissertation

Presented to

the Faculty of the Program of Materials Science and Engineering

University of Houston

In Partial Fulfillment

of the Requirement for the Degree

Doctor of Philosophy

In Materials Science and Engineering

By

Shaowei Song

May 2019

Abstract

Solutions to the growing energy demand and environment concerns can be increasing the current energy conversion efficiency or seeking alternative energy sources. Thermoelectric materials can directly harvest and convert waste heat from industrial, residential, commercial and transportation to electricity. However, the low conversion efficiency of thermoelectric material severely hinders its mass commercial application in past few decades, because thermoelectric parameters including electrical conductivity, Seebeck coefficient, and electronic thermal conductivity are intimately interdependent on each other by carrier concentration. Nanosized materials exhibit advantages to decouple the thermoelectric parameters. In my work, thermoelectric performances of n-type $\text{Mg}_3\text{Sb}_{1.5}\text{Bi}_{0.5}$ -based compounds are enhanced through grain alignment and carrier concentration optimization. Due to its typical layered crystal structure, partial texturing in the (001) plane is achieved by hot forging. Hall mobility is significantly improved to $105 \text{ cm}^2 \text{ V}^{-1} \text{ s}^{-1}$ in the (001) plane, resulting in higher electrical conductivity, and power factor of $18 \mu\text{W cm}^{-1} \text{ K}^{-2}$ at room temperature. Additionally, all of the Mg vacancies in $\text{Mg}_3\text{Sb}_{1.5}\text{Bi}_{0.5}$ -based compounds are almost eliminated by simple Y doping, and n-type conduction was successfully achieved without adding extra Mg in the initial composition. The carrier concentration is optimized through the combination of Y and Mg, leading to a record peak ZT of ~ 1.8 at 773 K in $\text{Mg}_{3.02}\text{Y}_{0.02}\text{Sb}_{1.5}\text{Bi}_{0.5}$.

Electrochemical water splitting is capable of converting electricity to chemical energy stored as hydrogen, which is considered to be one of the most promising energy alternatives. Oxygen evolution reaction (OER) as one-half reaction of water splitting suffers from multiple steps of proton-coupled electron transfer and displays a sluggish

kinetic process, it is challenging to develop efficient OER catalysts in order to match well with hydrogen evolution reaction for overall water splitting. We develop a new route to synthesize highly efficient and robust bulk catalyst of $\text{Ni}_{1-x}\text{Fe}_x$ layered double hydroxide ($\text{Ni}_{1-x}\text{Fe}_x\text{-LDH}$) for OER by ball milling and sintering. The nano-sheet catalysts achieve 100, 500, and 1000 mA cm^{-2} at overpotentials of 244, 278, and 300 mV, respectively, as well as a low Tafel slope of 58 mV dec^{-1} in 1 M KOH.

Table of Contents

Acknowledgements.....	v
Abstract	viii
Table of Contents.....	x
List of Figures.....	xiv
Chapter 1 Introduction	1
1.1 Background	1
1.2 Introduction to thermoelectric materials	3
1.3 Strategies for thermoelectric performance improvement.....	5
1.3.1 Nano engineering on charge carrier transportation	5
1.3.1.1 Optimization of carrier concentration	5
1.3.1.2 Energy filtering	8
1.3.1.3 Band convergency	10
1.3.1.4 Resonate states	13
1.3.2 Nano effect on phonon transport.....	14
1.4 Electrochemical water splitting.....	17
1.4.1 Introduction of water splitting.....	17
1.4.2 Strategies to improve efficiency of water electrolysis	21
1.4.2.1 Energy barrier and resistance	21
1.4.2.2 Large electrochemical active surface area (ECSA).....	22

1.4.2.3 Free energy of adsorption and desorption	23
Chapter 2 Characterization	26
2.1 Thermoelectric materials	26
2.1.1 Thermoelectric properties characterization	26
2.1.2 Phase and microstructure characterization	27
2.2 Water splitting	28
2.2.1 Electrochemical activity characterization	28
2.2.2 Electrochemical impedance spectroscopy	29
2.2.3 iR compensation	31
2.2.4 X-ray Photoelectron Spectroscopy	34
2.2.4 Raman Spectroscopy	34
Chapter 3 Achieving high thermoelectric performance of Mg ₃ Sb ₂ -based compounds by grain alignment and carrier concentration optimization.	35
3.1 Background	35
3.2 Grain alignment promotes the thermoelectric performance of n-type Mg ₃ Sb _{1.5} Bi _{0.5} compounds	36
3.2.2 Introduction	36
3.2.3 Experiment	38
3.2.3.1 Synthesis	38
3.2.3.2 Rietveld refinement and rocking curve	40

3.2.3.4 Results and discussion.....	40
3.2.3.5 Conclusions	47
3.3 Achieving high thermoelectric performance of n-type $\text{Mg}_3\text{Sb}_{1.5}\text{Bi}_{0.5}$ -based compounds by effective donor	47
3.3.1 Introduction	47
3.3.2 Experimental section	49
3.3.2.1 Synthesis.....	49
3.3.2.2 Neutron diffraction	49
3.3.2.3 Sound velocity measurement	49
3.3.3 Results and discussion.....	50
3.3.3.1 Realizing n-type conductivity by Y doping in $\text{Mg}_{3-x}\text{Y}_x\text{Sb}_{1.5}\text{Bi}_{0.5}$	50
3.3.3.2 Enhancement of thermoelectric performance by adding extra Y as $\text{Mg}_{3.0}\text{Y}_x\text{Sb}_{1.5}\text{Bi}_{0.5}$	57
3.3.3.3 Joint effect of Y and Mg in $\text{Mg}_{3.0+\delta}\text{Y}_{0.02}\text{Sb}_{1.5}\text{Bi}_{0.5}$	60
3.3.4 Conclusions	66
Chapter 4 A new way to synthesize robust and porous $\text{Ni}_{1-x}\text{Fe}_x$ layer double hydroxide for efficient electrocatalytic oxygen evolution	67
4.1 Introduction	67
4.2 Experiments.....	69
4.2.1 Synthesis.....	69

4.2.2 Electrochemical characterization	70
4.2.3 Materials characterization	70
4.2.4 Density functional perturbation theory (DFPT) lattice dynamics of β -Ni(OH) ₂	71
4.3 Results and discussion.....	72
4.3.1 Effects of Ni/Fe ratio on the performance of oxygen evolution reaction	72
4.3.2 V-doped Ni _{0.75} Fe _{0.25} -LDH for highly efficient OER.....	78
4.3.3 Conclusions	85
Chapter 5 Summary	86
References.....	88
List of Publications	109

List of Figures

Figure 1 (a) Schematic of Seebeck effect and (b) Peltier effect. (c) Schematic of thermal generator and refrigerator.	4
Figure 2 Carrier concentration dependence of thermoelectric parameters.	6
Figure 3 Schematic of energy barrier between nano inclusion and matrix.....	8
Figure 4 Relative position of light valence band and heavy valence band dependent on dopant element and temperature in PbTe/Se.	10
Figure 5 Resonate states was produced when Fermi level aligns with local distorted density of states.	12
Figure 6 All-scale hierarchical structure for full-wavelength phonon scattering.	14
Figure 7 Schematic of water splitting in electrolysis cell.	17
Figure 8 Pourbaix diagram for water at standard temperature and pressure.	19
Figure 9 The distribution of charge resistances in the water splitting.	20
Figure 10 Schematic of measurement principle of Seebeck coefficient and electrical conductivity.....	26
Figure 11 Schematic of double layer structure and the corresponded equivalent circuit during water splitting.	28
Figure 12 Nyquist plots fitting with simplifying Randles equivalent circuit.....	29
Figure 13 Three electrode configuration system for electrochemical measurement.	30
Figure 14 Schematic of equivalent circuit of three-electrodes configuration measurement in electrolysis cell.	31
Figure 15 Current interruption for iR compensation.	32

Figure 16 Crystal structure of Mg ₃ Sb ₂ -based Zintl compounds.	37
Figure 17 Schematic of hot pressing and hot forging.	39
Figure 18 (a) XRD patterns of as-pressed and textured Mg _{3.1} Nb _{0.1} Sb _{1.5} Bi _{0.49} Te _{0.01} . (b) Rocking curves of the (002) plane in as-pressed and the 2nd re-pressed samples.	41
Figure 19 SEM images of the freshly fractured surface of the as-pressed sample (a) and textured sample (b) in the plane parallel to the press direction.	42
Figure 20 Temperature dependence of electrical conductivity (a), Seebeck coefficient (b) and power factor (c) of Mg _{3.1} Nb _{0.1} Sb _{1.5} Bi _{0.49} Te _{0.01} with and without texture.	44
Figure 21 Temperature dependence of thermal conductivity (a) and <i>ZT</i> (b) of Mg _{3.1} Nb _{0.1} Sb _{1.5} Bi _{0.49} Te _{0.01} with and without texture. Data of Tamaki et al. (Mg _{3.2} Sb _{1.5} Bi _{0.49} Te _{0.01}) were also included for comparison.	45
Figure 22 (a) X-ray diffraction patterns of hot-pressed Mg _{3.0-x} Y _x Sb _{1.5} Bi _{0.5} compounds with the standard Mg ₃ Sb ₂ (PDF# 03-0375, solid blue) and YSb (PDF#15-0847, solid red). (b) Lattice parameters as a function of Y.	50
Figure 23 (a) Temperature dependence of the Seebeck coefficient of Mg _{3-x} Y _x Sb _{1.5} Bi _{0.5} (<i>x</i> = 0, 0.05, 0.1). (b) Room temperature carrier concentration and Hall mobility, (c) Temperature dependence of the electrical conductivity.	51
Figure 24 Temperature dependence of (a) electrical conductivity, (b) Seebeck coefficient, (c) power factor, (d) thermal conductivity, (e) specific heat capacity, and (f) <i>ZT</i> for Mg _{3-x} Y _x Sb _{1.5} Bi _{0.5} (<i>x</i> = 0.125, 0.15, and 0.2).	52
Figure 25 Temperature dependence of electronic thermal conductivity of Mg _{2.85} Y _{0.15} Sb _{1.5} Bi _{0.5} in comparison with that of Mg _{3.2} Sb _{1.5} Bi _{0.49} Te _{0.01}	53

Figure 26 (a) TEM image of microstructure morphology of $\text{Mg}_{2.9}\text{Y}_{0.1}\text{Sb}_{1.5}\text{Bi}_{0.5}$. (b) High-resolution TEM image shows the lattice fringes with 0.733 nm spacing, with SAED pattern (inset) indexed to be trigonal phase along the [010] zone axis.....	54
Figure 27 (a) (HAADF)-STEM image of $\text{Mg}_{2.9}\text{Y}_{0.1}\text{Sb}_{1.5}\text{Bi}_{0.5}$ (the inset shows the EDX mapping). (b)-(e) EDX mapping of the bright areas. (f) High-resolution TEM image taken from the bright areas with the corresponding SAED pattern (inset).....	55
Figure 28 X-ray diffraction patterns of hot-pressed $\text{Mg}_{3.0}\text{Y}_x\text{Sb}_{1.5}\text{Bi}_{0.5}$ ($x = 0.03, 0.035, 0.04$) compounds with standard Mg_3Sb_2 pattern (PDF# 03-0375, solid blue).....	57
Figure 29 Temperature dependence of (a) electrical conductivity, (b) Seebeck coefficient (inset is temperature dependence of power factor), (c) thermal conductivity, and (d) ZT of $\text{Mg}_{3.0}\text{Y}_x\text{Sb}_{1.5}\text{Bi}_{0.5}$ ($x = 0.03, 0.035, \text{ and } 0.04$).....	59
Figure 30 Temperature dependence of (a) electrical conductivity, (b) Seebeck coefficient, (c) power factor, (d) thermal conductivity, (e) specific heat capacity, and (f) ZT of $\text{Mg}_{3+x}\text{Y}_{0.02}\text{Sb}_{1.5}\text{Bi}_{0.5}$ ($x = 0.015, 0.02, \text{ and } 0.04$).	61
Figure 31 Powder neutron diffraction and Rietveld refinement analysis of $\text{Mg}_{3.0+x}\text{Y}_{0.02}\text{Sb}_{1.5}\text{Bi}_{0.5}$. (a) $\text{Mg}_{3.0}\text{Y}_{0.02}\text{Sb}_{1.5}\text{Bi}_{0.5}$, (b) $\text{Mg}_{3.02}\text{Y}_{0.02}\text{Sb}_{1.5}\text{Bi}_{0.5}$, and (c) $\text{Mg}_{3.04}\text{Y}_{0.02}\text{Sb}_{1.5}\text{Bi}_{0.5}$	62
Figure 32 Highly reproducible thermoelectric performances of $\text{Mg}_{3.02}\text{Y}_{0.02}\text{Sb}_{1.5}\text{Bi}_{0.5}$ (Each color stands for each independent experiment).	64
Figure 33 X-ray diffraction patterns of sintered $\text{Ni}_{1-x}\text{Fe}_x\text{Se}_{1.15}$ ($x = 0.2, 0.25, \text{ and } 0.3$) compounds in comparison with those of standard $\text{Ni}_{0.85}\text{Se}$ (solid blue, PDF # 18-0888) and NiSe (solid red, PDF # 020892).....	72

Figure 35 (a) and (b) SEM images of the as-prepared $\text{Ni}_{0.75}\text{Fe}_{0.25}\text{Se}_{1.15}$. (c) and (d) SEM images of $\text{Ni}_{0.75}\text{Fe}_{0.25}\text{Se}_{1.15}$ after oxidation in electrolyte. (e) and (f) TEM images of $\text{Ni}_{0.75}\text{Fe}_{0.25}\text{Se}_{1.15}$ after oxidation in electrolyte.	73
Figure 34 Photograph of $\text{Ni}_{0.75}\text{Fe}_{0.25}\text{Se}_{1.15}$ after oxygen evolution reaction.	73
Figure 34 (a) Raman spectrum of $\text{Ni}_{0.75}\text{Fe}_{0.25}\text{Se}_{1.15}$ after water electrolysis. (Atoms: grey - Ni, red - O, and white - H). (b)-(f) High-resolution XPS spectra of as-prepared $\text{Ni}_{0.71}\text{V}_{0.04}\text{Fe}_{0.25}\text{Se}_{1.15}$ (upper panels) and post-OER (lower panels).	74
Figure 35 (a) Linear sweep voltammetry curves and (b) the corresponding Tafel plots of $\text{Ni}_{1-x}\text{Fe}_x\text{Se}_{1.15}$ ($x = 0.2, 0.25, \text{ and } 0.3$) compounds after stabilization in 1 M KOH solution.....	75
Figure 36 X-ray diffraction patterns of as-prepared $\text{Ni}_{0.71}\text{V}_{0.04}\text{Fe}_{0.25}\text{Se}_{1.15}$ and post-OER $\text{Ni}_{0.71}\text{V}_{0.04}\text{Fe}_{0.25}\text{Se}_{1.15}$	78
Figure 37 SEM image of the as-prepared $\text{Ni}_{0.71}\text{V}_{0.04}\text{Fe}_{0.25}\text{Se}_{1.15}$ and EDS composition analysis of two spots and one area shown in the image.....	79
Figure 38 TEM image of $\text{Ni}_{0.71}\text{V}_{0.04}\text{Fe}_{0.25}\text{Se}_{1.15}$ after OER and EDS composition analysis over the whole image area	80
Figure 39 (a) The LSV curves of $\text{Ni}_{0.75-y}\text{V}_y\text{Fe}_{0.25}\text{Se}_{1.15}$. (b) The corresponding Tafel slopes. (c) Nyquist plots of $\text{Ni}_{0.75-y}\text{V}_y\text{Fe}_{0.25}\text{Se}_{1.15}$. (d) The overpotential comparison at current density of 50 mA cm^{-2} . (e) and (f) Durability tests.	81
Figure 40 LSV curves of commercial Ni foam. (b) Linear fitting of the capacitive currents as a function of scan rate. (c) Double-layer capacitance (C_{dl}) measurement of $\text{Ni}_{0.75}\text{Fe}_{0.25}\text{Se}_{1.15}$ and (d) $\text{Ni}_{0.71}\text{V}_{0.04}\text{Fe}_{0.25}\text{Se}_{1.15}$	83

Chapter 1 Introduction

1.1 Background

“Global warming of 1.5 °C” raises humanity alerts about the environment concerns and weather extreme in 2018. This predication with high confidence asks for every person’s contribution to control the anthropogenic emission, which would give chance to keep the global warming below 1.5 °C by the end of this century.^[1] Fossil fuel, as one of main energy sources, has been contributing to the world development and society evolution since the pre-industry period.^[2] Amounts of conflicts and problems stand between huge energy demanding and sustainable development. Research community have made enormous efforts to seeking for new clean, cost-effective and ecofriendly energy instead of current energy configuration.^[3] Though solar, wind, tide, and hydropower have been well adopted and benefit humanity, these kinds of energy conversion are accompanying with some disadvantages, such as complicated design, high-maintenance cost, and collateral environment pollution.^[4]

In past few decades, thermoelectric materials offer a feasible solution to predicament. Thermoelectric generator, as solid-state energy conversion, exhibits superior advantages than traditional energy conversion, such as no-moving parts, nonchemical reaction, low-cost maintenance, quiet operation, and zero emission *etc.*^[5] The tricky situation for application is its low conversion efficiency. The performance of thermoelectric materials was governed by dimensionless figure of merit ZT , which was struggling with 1 till the end of last centuries.^[6] ZT value 1 of thermoelectric materials indicated 10% conversion efficiency from heat to electric power under ideal working condition, that’s not good enough to commercialize it in large scale.^[7] The target figure of

merit for mass production and application should be beyond 3.^[8] The emerging of nanotechnology totally changed this situation. Advanced theories and concept including quantum well, energy filtering, resonate states, and band engineering are proposed, and figure of merit ZT was brought up to 2 by combing these theories with innovative fabrication process in past twenty decades, such as, ball milling, spinning, spark plasma sintering, and molecular beam epitaxy (MBE) *etc.*^[9]

In addition to increasing current utilization rate of energy circulation, people also try to seek other advanced alternative energy sources. Being the most abundant of elements in the universe and one of the highest energy density values per mass, hydrogen has been considered as the most promising energy alternatives to replace fossil fuel and change the energy configuration in the future.^[10] The combustion of hydrogen is quiet and has no emission but heat and water vapor.^[11] In past few decades, hydrogen mainly is made from fossil fuel and its production is dominated by steam methane reforming of natural gas, followed by partial oxidation and autothermal reforming.^[12] Hydrogen is generally used in refining industry as petrochemical for hydrocracking and desulphurization, ammonia production, metal refining, methanol production, food processing and electronics sectors in existing industry. Electrochemical water splitting is another well-established commercial technology to convert electricity into chemical energy stored by hydrogen.^[13] This method principally relies on the electrode catalysts. Water splitting is composed of hydrogen evolution reaction (HER) on cathode and oxygen evolution reaction (OER) on anode. Noble metels (Pt, Ir, Ru) and their oxides (IrO_2 and RuO_2) have been traditionally acknowledged as the most efficient catalysts for HER and OER, respectively.^[14] However, their high cost and scarcity severely hinder large-scale applications. Lately based on

cutting-edge characterization methods, like high resolution transmission electron microscopy, in-situ X-ray absorption spectroscopy *etc.*^[15] the mechanism of water electrolysis are further disclosed. It turns out that nanostructure are beneficial for exposing more active sites and improving the electrodes durability.^[16] Transition metal-based catalysts with different morphologies displays comparable, even better efficiency than that of noble metals, such as metal selenide,^[17] metal phosphide,^[18] Ni/Fe hydroxides,^[19] Ni/Fe double layer hydroxides,^[20] MoNi₄^[21] *etc.* On January 17, 2019, South Korea government announces “Roadmap to Become the World Leader in the Hydrogen Economy” in next 20 years, which laid out its goals of leading hydrogen technology worldwide, including hydrogen vehicles, production and refueling stations. As the dilemma between increasing energy demanding and environment concerns related to global warming constantly are becoming intense, more global attention was paid to hydrogen production in recent years. Though water electrolysis has been known for 200 years, the large-scale application was still limited by high costs from noble metal catalysts (Pt/Ir) and proton exchange membrane in acid electrolyte, or low conversion efficiency in alkaline electrolyte.^[22] Developing non-noble metal catalyst with high efficiency is essential to promote large-scale hydrogen technology development.^[23]

1.2 Introduction to thermoelectric materials

This energy conversion from waste heat to electric power by thermoelectric materials (TE) depends on Seebeck effect, which was discovered by Thomas J. Seebeck in 1821.^[8] As shown in Fig. 1(a), when the junctions connecting two dissimilar metal wires was given to temperature difference, voltage drop can be generated at the ends of wires. The reversal process of Seebeck effect is Peltier effect, which was discovered by Jean C.

A. Peltier in 1834. In Fig. 1(b) Peltier effect was described as a presence of heating or cooling at the junction connecting by two dissimilar metals when a current was injected into a circuit. The general thermoelectric power generator and refrigerator was individually relied on Seebeck and Peltier effect, respectively. Fig. 1(c) presents the common schematic of thermoelectric generator and refrigerator, which is consisted of n-type and p-type

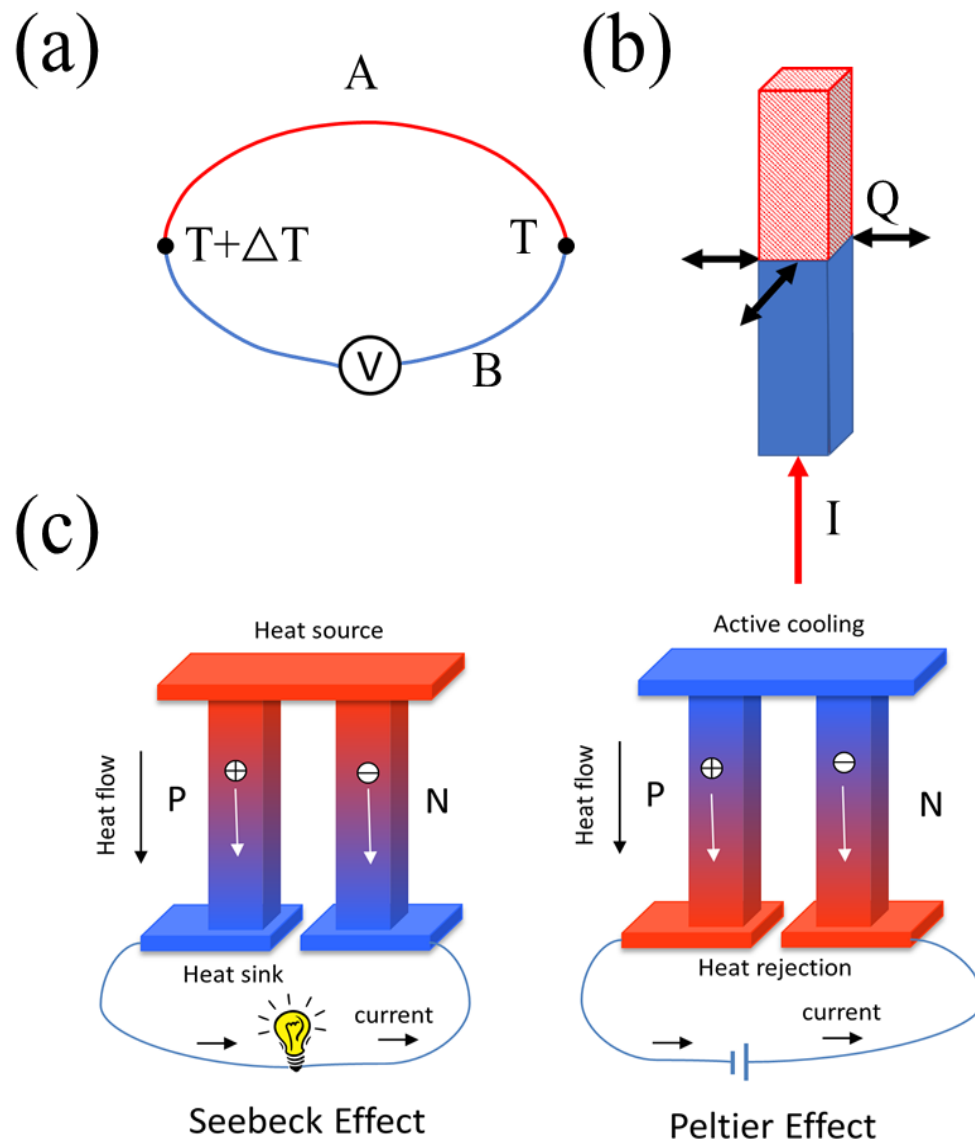


Figure 1 (a) Schematic of Seebeck effect and (b) Peltier effect. (c) Schematic of thermal generator and refrigerator.

thermoelectric elements wired electrically in series and thermally in parallel.^[24] The conversion efficiency of thermoelectric generator was evaluated by

$$\eta = \left(\frac{T_H - T_C}{T_H} \right) \frac{\sqrt{(1+ZT)} - 1}{\sqrt{(1+ZT)} + \frac{T_C}{T_H}}, \quad (1.1)$$

where T_H and T_C are the temperature of hot side and cold side of thermoelectric generator, respectively.^[25] And ZT is denoted as figure of merit, which was used for evaluating the performance of thermoelectric materials and is expressed by

$$ZT = \frac{\sigma S^2}{\kappa_t} T, \quad (1.2)$$

where S , σ , κ_t and T are the Seebeck coefficient, electrical conductivity, thermal conductivity ($\kappa_t = \kappa_e + \kappa_l$, with κ_e being the electronic part and κ_l the lattice part), and temperature in Kelvin, respectively.^[26] From thermoelectric materials to the generator, it is an extremely complicated engineering work. The process of energy conversion is accompanying with Seebeck effect, Peltier effect, Thomson effect, Joule heating, thermal expansion and contact resistance *etc.*^[27] High figure of merit should be required for high-efficiency energy harvesting in large-scale application.^[28]

1.3 Strategies for thermoelectric performance improvement

1.3.1 Nano engineering on charge carrier transportation

1.3.1.1 Optimization of carrier concentration

Based on the definition of figure of merit, ZT enhancement can be realized by either improving numerator, which means the power factor ($S\sigma^2$), or decreasing the denominator (thermal conductivity).^[29] All of thermoelectric parameters are intrinsic properties of

materials. Seebeck coefficient is defined as the Seebeck voltage per unit temperature difference, which can be described by Mott's equation,

$$S = \frac{\pi^2 k_B}{3 e} k_B T \left\{ \frac{1}{n} \frac{dn(E)}{d(E)} + \frac{1}{\mu} \frac{d\mu(E)}{d(E)} \right\}_{E=E_F}, \quad (1.3)$$

where e , $n(E)$, $\mu(E)$, k_B , T , and E_F are electron charge, carrier concentration at energy E , mobility at energy, Boltzmann constant, temperature and Fermi level.^[30] Electrical conductivity is calculated by

$$\sigma = n\mu e, \quad (1.4)$$

the electronic contribution to thermal conductivity can be estimated Wiedemann-Franz law by

$$k_e = \sigma L T = ne\mu L T, \quad (1.5)$$

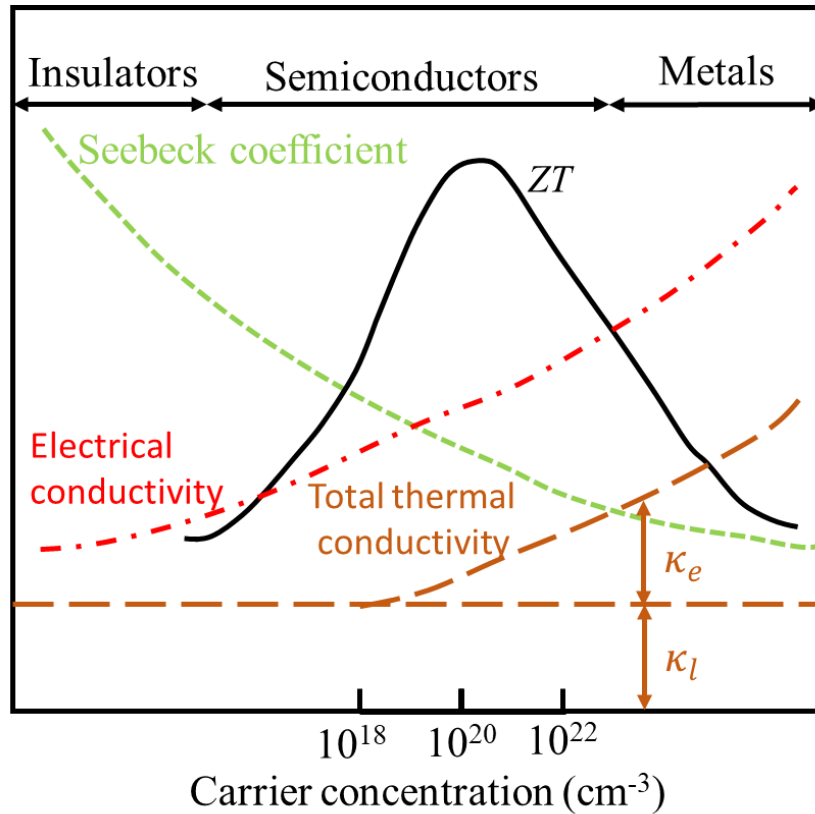


Figure 2 Carrier concentration dependence of thermoelectric parameters.

where L is the Lorenz factor, and referred to $2.4 \times 10^{-8} \text{ J}^2 \text{ K}^{-2} \text{ C}^{-2}$ for free electrons.^[31, 32] It is notable that S , σ , and κ are couple with each other by carrier concentration. Fig. 2 illustrates the strong interdependence of each thermoelectric parameter on carrier concentration. It is extremely difficult to improve one parameter without deteriorating the others. For example, higher electrical conductivity normally leads to higher thermal conductivity and poor Seebeck coefficient. Low thermal conductivity results in low electrical conductivity and large Seebeck coefficient. However, it turns out that the maximum of ZT value typically locates at the range of carrier concentration, around 10^{20} cm^{-3} , which is corresponding to heavily doped or degenerate semiconductors.^[33] Enlighten by this, tuning carrier concentration later was proved to be the most efficient approach to enhance thermoelectric performance. For example, it was demonstrated that alkaline metals were effective dopant to adjust the carrier concentration in PbTe/Se compounds.^[34]^{35]} Subgroup III and lanthanide elements are very effective donor for n-type Mg_3Sb_2 -based Zintl compounds.^[36] Though the efforts that carrier concentration contributes to thermoelectric performance enhancement is important, the biggest challenge of high-efficient thermoelectric materials is to decouple interplay of charge carrier in thermoelectric parameters. In 1993, Hicks and Dresselhaus introduced that quantum confinement of charge carriers in low-dimensional materials, which enable manipulating power factor independently and dramatically increase ZT value beyond 1.^[37, 38] When nano-structure based concepts were introduced into thermoelectric field, significant achievements and innovative breakthrough were made in past two decades. Based on optimized carrier concentration, nano technology is capability of precisely engineering band structure,^[39] and tuning phonon and electron transport.^[40] For example, thermal

conductivity can be effectively suppressed with minimizing influences on power factor, or Seebeck coefficient was improved without deteriorating electrical conductivity.

1.3.1.2 Energy filtering

Improving power factor usually is one of the approaches to boost TE efficiency, and simultaneously give rise to high output power.^[41] Power factor is the product of electrical conductivity and Seebeck coefficient. Improvement of power factor should result from the straight increase of Seebeck coefficient as opposed to good electrical conductivity, because Seebeck coefficient dose not straight affect thermal conductivity, while manipulating electrical conductivity would inevitably influence the electronic part of thermal conductivity.^[42] From Mott's equation, Seebeck coefficient is determined by carrier density of states (DOS) near Fermi level and average energy of charge carrier, which suggest that either high DOS or higher average energy of charge carrier can give rise to improved Seebeck coefficient.^[43] The typical case is the superlattice, which is formed by alternating materials with thickness of 3 nm. Quantum-well structure created by superlattice lead to confinement of in-plane charge carrier, and the DOS in each well structure was enhanced sharply, resulting in substantial improvement of Seebeck

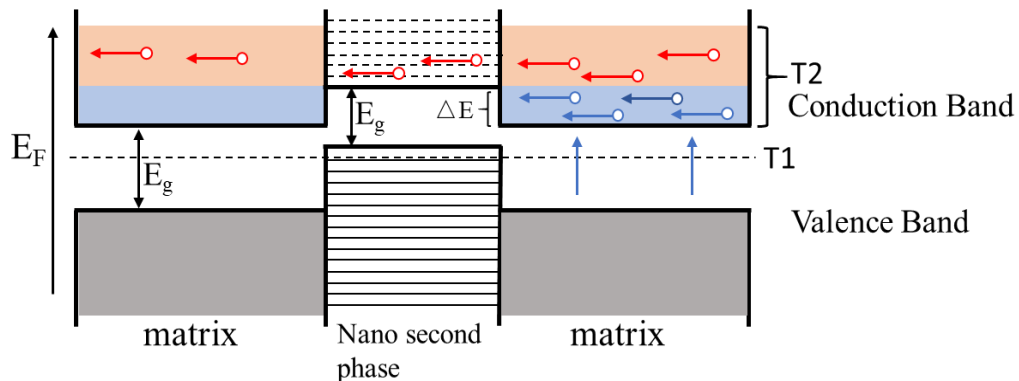


Figure 3 Schematic of energy barrier between nano inclusion and matrix.

coefficient and power factor. When it comes to ZT value, superlattice presents its drawback that heat not only flow through in-plane well, but also out plane, which offset the enhancement of Seebeck coefficient. The transfer of charge carrier is confinement in two-dimensional space, but heat flow embodies bulk phenomena. Though thinner well was tried to make up this disadvantage, tunneling effect between adjacent quantum well normally mitigate the improved power factor.^[44]

Inspired by the effect of quantum well in superlattice, energy filtering was introduced into bulk materials by compositing the second nanosized phase within bulk materials.^[45] Due to the difference of band structure, energy barrier will be created cross the gran boundary. Fig. 3 presents a typical band engineering design for energy filtering. Electrons with low energy normally were trapped or filtered by the barrier, and carriers with high energy will flow through, resulting in increased average energy of charge carrier and higher Seebeck coefficient. Though reduced carrier concentration servicing in transportation would jeopardize electrical conductivity, dramatically improved Seebeck coefficient will mitigate this loss, leading to enhancement of power factor.^[46] It was demonstrated that energy filtering was created at the coherent grain boundaries when full-Heusler nano inclusions of $Zr_{0.25}Hf_{0.75}Ni_2Sn$ were dispersed into half-Heusler nano materials of $Zr_{0.25}Hf_{0.75}NiSn$. Normally, the carrier concentration was expected to be increased if the matrix was composited with metal inclusions, but obviously carrier density was decreased by 40% at room temperature. It was claimed that the improvement of Seebeck coefficient mainly benefits from the filtering of low-energy carrier involving the transportation at low temperature. It's unexpected to observe the mobility was improved dramatically, which compensate the loss of carrier concentration, finally leading to the

power factor increased by 60% at room temperature compared to the pure matrix $Zr_{0.25}Hf_{0.75}Ni_2Sn$. At high temperature, low carrier concentration compared to undoped matrix did not induce bipolar effect, and carrier concentration rise rapidly with temperature, which was attributed to the participation of low energy carrier, which access energy channel by gaining sufficient energy from the thermal energy.

It should be spell out that energy filtering couldn't be correctly introduced by simply compositing nanosized inclusion with matrix.^[8] The phases separated by boundaries should be coherent or structural similarity to guarantee lattice matching at the boundaries, which can promise the boundaries thermally stable and low-energy. Otherwise both high energy and low energy carrier would be scattered simultaneously. The achievable amount of Seebeck coefficient improvement, and carrier concentration reduction is strongly dependent on energy barrier ΔE , which can be manipulated by precisely controlling nano-inclusion size, boundary tilt angle and inclusion dispersion.^[47]

1.3.1.3 Band convergency

In heavily doped semiconductors or degenerate semiconductors, Mott equation is simplified as

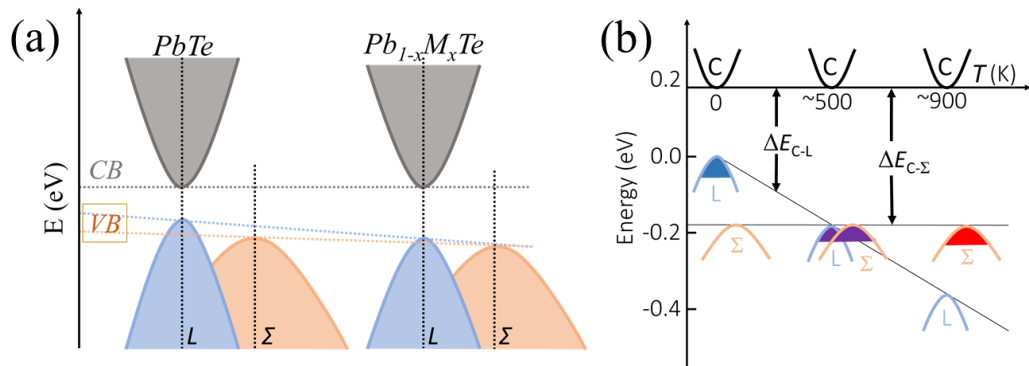


Figure 4 Relative position of light valence band and heavy valence band dependent on dopant element and temperature in PbTe/Se.

$$S = \frac{8\pi^2 k_B^2 T}{3eh^2} m^* \left(\frac{\pi}{3n}\right)^{2/3}, \quad (1.6)$$

where h is the Plank constant, m^* is the effective mass. It can be observed that effective mass is another option to improving Seebeck coefficient. Multiband convergence has the advantage of producing large m^* without explicitly reducing the mobility.^[48] Specifically, band convergence of high symmetry crystal structures like PbTe(Se),^[49] (Bi,Sb)₂Te₃,^[50] and SnTe^[51] can be realized by tuning band offset between the light and heavy valence band. The light-hole valence band locate at L points of the highly symmetric Brillouin zone, and the heavy band defined as heavy-hole valence band exists at the Σ points.^[52] The difference of light band and heavy band is ascribed to the different effective mass of charge carrier.^[39] As shown in Fig. 4, there is an energy offset between two separated valence band, which is materials dependent. The value in PbTe normally is ~ 0.15 eV, and ~ 0.3 eV in SnTe at 300 K. The band convergence was described as the redistribution of charge carrier between two valence bands when the L and Σ band edges are moving closer. Normally, only charge carriers in the light-band takes part in transportation. After band converging, the overall effective mass would be enhanced due to participation of heavy-effective mass from the heavy valence band, leading to intense improvement of Seebeck coefficient. The effective mass after carrier redistribution can be calculated by

$$m^* = N_v^{2/3} m_b^*, \quad (1.7)$$

where N_v stands for the number of degenerate valleys, and m_b^* is the average (single valley) density of states effective mass of degenerate valley.^[52] Room-temperature TE materials (Bi,Sb)₂Te₃ displays substantial band degeneracy, with $N_v = 6$ for conduction band and valence band.^[50] It also find out that PbTe has band degeneracy 4 for L band and 12 for Σ band.^[53]

Band convergency can be produced at desired temperature or by proper dopant. Fig. 4(a) presents typical relative energy of valence bands of $\text{PbTe}_{0.85}\text{Se}_{0.15}$.^[54] As the temperature rises to 500 K, L band and Σ band start to converge, leading to transportation contributions from both L band and Σ band, which is beneficial for keeping Seebeck coefficient increasing at high temperature. Combining with strong phonon scattering, ZT value of 1.8 is reached at ~ 800 K. Band convergency also could be realized by doping in the matrix, for example, $\text{Pb}_{1-x}\text{M}_x\text{Se}$ ($M = \text{Mg}, \text{Mn}$). With increasing content of Mg or Mn in the matrix, the energy level of both L and Σ band begin to reduce, but L band reduces much faster than Σ band, resulting in decreased energy offset between L and Σ band. Finally, a high ZT value of 1.6 at 700 K and 2.0 at 873 K was achieved by Mn and Mg doped PbTe, respectively.^[55]

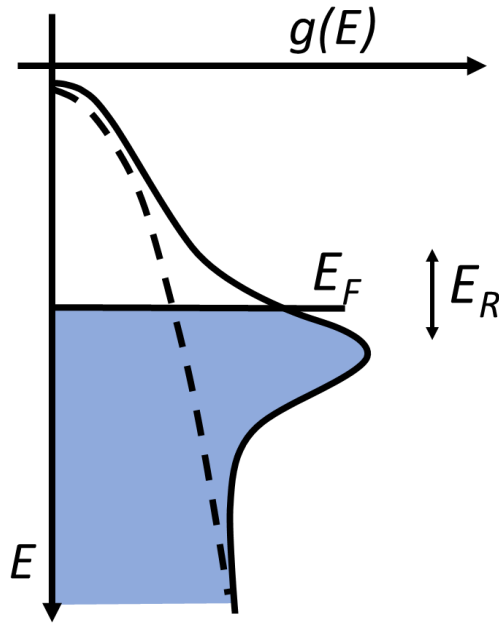


Figure 5 Resonate states was produced when Fermi level aligns with local distorted density of states.

1.3.1.4 Resonate states

As aforementioned strategy for Seebeck coefficient enhancement, improving density of states near the Fermi level is another feasible approach. Based on Mahan-Sofo theory, DOS can be increased when the Fermi level of a semiconductor aligns properly within the range of the excess DOS in the band (Fig. 5). This situation occurs that when a local impurity energy level was created by the proper dopant in the semiconductor and valence or conduction band can resonates with it.^[51, 56, 57] It has been demonstrated that TI impurity level produced a distortion of the electronic DOS and enhance the Seebeck coefficient, leading to peak ZT of ~ 1.5 at 773 K in p-type PbTe.^[56]

The band convergence or resonate states can be traced by the deviation of dependance of Seebeck coefficient on the carrier concentration, which was named as Pisarenko curves. The theoretic Pisarenko curves for thermoelectric materials can be calculated by a simple parabolic band model (SPB) as shown in following equation,

$$S = \pm \frac{k_B}{e} \left(\frac{(5/2+r)F_{3/2+r}(\eta)}{(3/2+r)F_{1/2+r}(\eta)} - \eta \right) \text{ and} \quad (1.8)$$

$$n = 4\pi \left(\frac{2m^*k_B T}{h^2} \right)^{3/2} \frac{F_{1/2}(\eta)}{R_H}, \quad (1.9)$$

where r and R_H is the scattering parameter, and Hall coefficient, respectively. $F_i(\eta)$ is the Fermi integral and η is the reduced Fermi energy.^[58] Zhang *et al.* investigate Al doping effect on n-type PbSe. Compared with the situation of Cl and I doping matching well with Pisarenko curves, Al doping exhibit enhanced Seebeck coefficient at the same concentration, which is 40% higher that of SPB model. The synergistic effect of enhanced Seebeck coefficient and low thermal conductivity from nanosized phonon scattering results in ZT of 1.3 at 850 K.^[59]

1.3.2 Nano effect on phonon transport

Thermal conductivity in thermoelectric materials is contributed by lattice part and electronic part. Only the lattice part is independent on the carrier concentration, so reducing the lattice thermal conductivity is a direct approach to enhance figure of merit in thermoelectric materials.^[60] Phonons as the quantized energy unit for lattice vibration are the carrier for thermal transport in the lattice. Distracting phonon transport or enhance phone scattering is helpful for reducing lattice thermal conductivity. Phonon normally encounter scattering from different source such as defects, inclusion, and boundaries, which has a size distribution, from nano to micro meters.^[1, 61] Fig. 6 illustrates the all-scale hierarchical structure for full-wavelength phonon scattering. Energy waves transporting in lattices have a spectrum of wavelengths, which is corresponding to different mean free path (MFP) for phonon. Strong and efficient scattering can be expected when the size of defects, inclusion and boundaries are comparable with the mean free path.^[62, 63, 64] The advantage

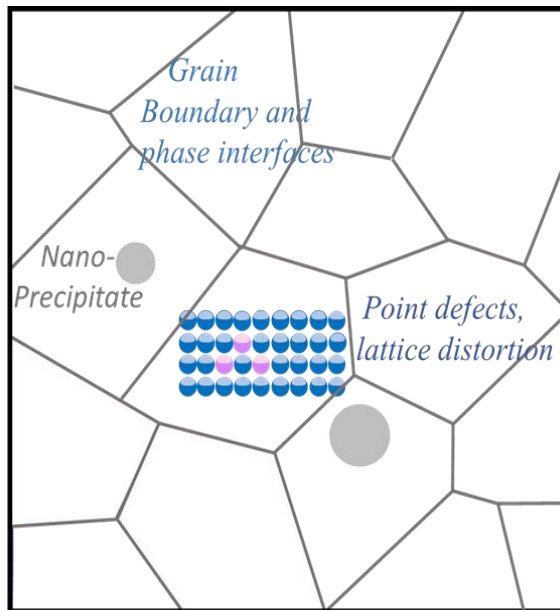


Figure 6 All-scale hierarchical structure for full-wavelength phonon scattering.

of nanomaterials is to produce more boundary interfaces to enhance phonon scattering. It should be emphasized that ball milling and cold pressing is one of the most popular and efficient methods to synthesize nano-size thermoelectric compounds.^[65, 66] Amounts of nanosized defects and grain boundaries are created, leading to strong scattering of short and intermediate MFP phonon. Benefiting from largely reduced lattice thermal conductivity, ZT value of p-type Bi_2Te_3 compounds achieved 1.4 at 373 K.^[67] Subsequently, all spectrum of wavelength scattering is also proposed, and the corresponding materials design was named as all-scale hierarchical architectures. The based principle of all-scale hierarchical architectures is to build different size of scattering source corresponding to different MFP phonons.^[35] For example, point defects or atomic-scale lattice disorder for short MFP phonons, grain boundaries, dislocation, lamellar/multilayers for medium MFP phonons, and mesosized grains or precipitation for long wavelength.^[49, 54] In order to realize all-scale hierarchical architecture scattering, advanced fabrication process is adopted. Point defects and atomic-scale lattice disorder usually are introduced by doping.^[68] Mass fluctuation or strain field phonon scattering can be realized by solid-solution alloying.^[41, 69] Multiple boundaries, dislocation and precipitation can be obtained by ball milling, melt spinning, and annealing.^[42, 70, 71] By taking these approaches, high ZT value of 2.2 at 915 K is achieved in p-type PbTe , which is attributed to atomic lattice disorder and nanosized endotaxial precipitates.^[53] It was demonstrated that high thermoelectric figure of merit of 2.2 is achieved in Na doped $\text{Pb}_{0.97}\text{Eu}_{0.03}\text{Te}$ by effectively suppressing lattice thermal conductivity through combining scattering effect of point defects, lattice dislocations, and nanosized interfaces.

“Phonon-glass electron-crystal” (PGEC) was another pursued conceptual approach for thermoelectric performance enhancement.^[72] PGEC thermoelectric materials possess a desirable single crystal structure for good electronic properties, and a disordered atomic arrangement akin to amorphous material for extremely low thermal conductivity. Of interest is the fact that PGEC system possess features in common with Skutterudites and clathrates, which originates from its crystal structure. Binary skutterudites has a normal formula MX_3 ($M = \text{Fe, Ni, Co, Rh, Ir}$ and $X = \text{P, As, Sb}$), and crystalized a distorted symmetric cubic structure. The unit cell is composed of eight cubes of M occupying the 8c sites ($\frac{1}{4}, \frac{1}{4}, \frac{1}{4}$), with six of these cube fillers with square rectangle of X occupying 24g (0, y, z) sites. There are two remaining voids left in the unit cell, the diameter of which was estimated to range from 0.17 to 0.2 nm.^[73, 74, 75] The main approach of obtaining phonon-glass thermal conductivity is to create “rattling” effect by filling the voids with small diameter, large-mass interstitials such as trivalent rare-earth ions. These filled “rattlers” usually produce local vibrational modes and disorder, which can strongly scatter phonons, leading to large reduction in the lattice thermal conductivity.^[76, 77]

Advanced technologies were employed to reduce the thermal conductivity further approaching to the amorphous limit, but the figure of merit improvement still was impeded by the interdependence of thermoelectric parameters. It turns out that material with intrinsically low thermal conductivity also displays potential for high thermoelectric performance, which normally has quite complicated atomic arrangement.^[78, 79, 80, 81] For example, Zintl phase, BiCuSeO, and liquid-like materials. Thermal conductivities of polycrystalline BiCuSeO are reported as $\sim 0.9 \text{ W m}^{-1} \text{ K}^{-1}$ at room temperature and $\sim 0.45 \text{ W m}^{-1} \text{ K}^{-1}$ at high temperature.^[82] AgSbTe display a very low thermal conductivity in the

temperature range of 300 K ($0.3 \text{ W m}^{-1} \text{ K}^{-1}$) and 673 K ($0.39 \text{ W m}^{-1} \text{ K}^{-1}$).^[83, 84] Liquid materials mainly refer to copper based chalcogenides, in which Se forms a rigid face-center cubic lattice, and copper ions are randomly distributed around Se sublattice, and behavior with liquid-like mobility.^[85] The Se cubic sublattice provide a crystalline pathway for charge transfer, and liquid-like Cu ions results in extremely low thermal conductivity. Their combination effect leads to peak ZT of ~ 1.5 at 1000 K in Cu_{2-x}Se compounds.^[86]

1.4 Electrochemical water splitting

1.4.1 Introduction of water splitting

Water splitting is described as water's dissociation into hydrogen and oxygen. This process contains two separate reaction, hydrogen evolution reaction (HER) and oxygen evolution reaction (OER).^[87] It's well known that water is one of the most stable substances on earth, so the dissociation process always an energy-cost process, which is capable of

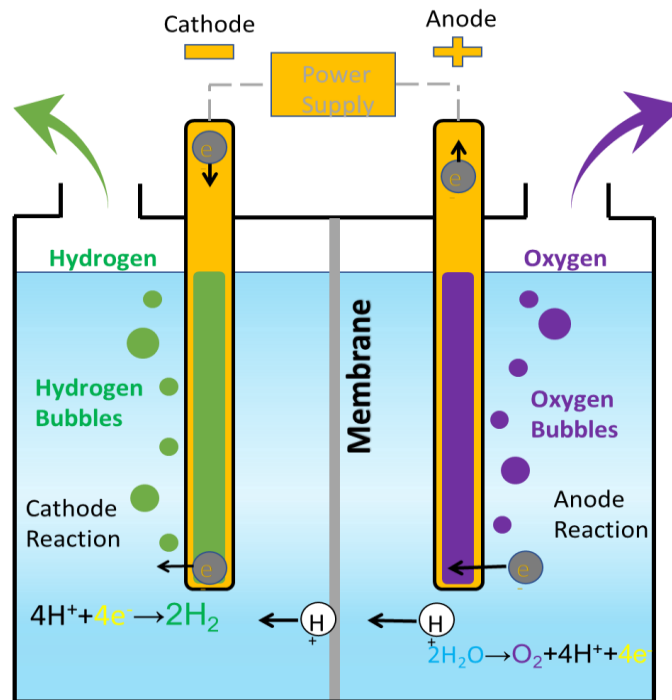
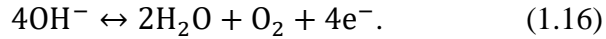
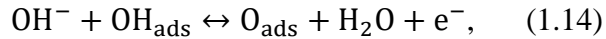
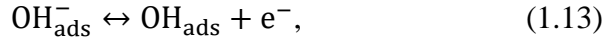


Figure 7 Schematic of water splitting in electrolysis cell.

converting electricity to chemical energy storage as hydrogen.^[12] As shown in Fig. 7, a electrolysis cell is composed of an anode, a cathode, a power source and electrolyte. When a DC potential is applied, electron will flow away from the negative electrode towards the cathode, where hydrogen ions consumed the electron to form hydrogen. Meanwhile, hydroxide ions driven by the electric field between negative and positive electrode move through the electrolyte and reach the anode, where hydroxide ions give away electrons to form oxygen. And these electrons go back to the positive terminal of the power source.^[12, 23, 88] The half reactions occurring on cathode are described as follows:^[13]



where H_{ads} is adsorbed hydrogen on the active site. The other half reaction occurring on the anode are as following:^[23]



These steps involve four proton-coupled electron transfers and oxygen-oxygen bond formation. This whole process can be conducted in alkaline solution, acid solution and neutral solution. However, alkaline and acid solution provide better charge transfer in the solution than that of neutral solution, and most of metal electrodes endure electrochemical corrosion for a longer time in alkaline solution than that in acid solution.^{[88,}

^{89]} Another disadvantage of conducting water splitting in acid solution is that the cathode

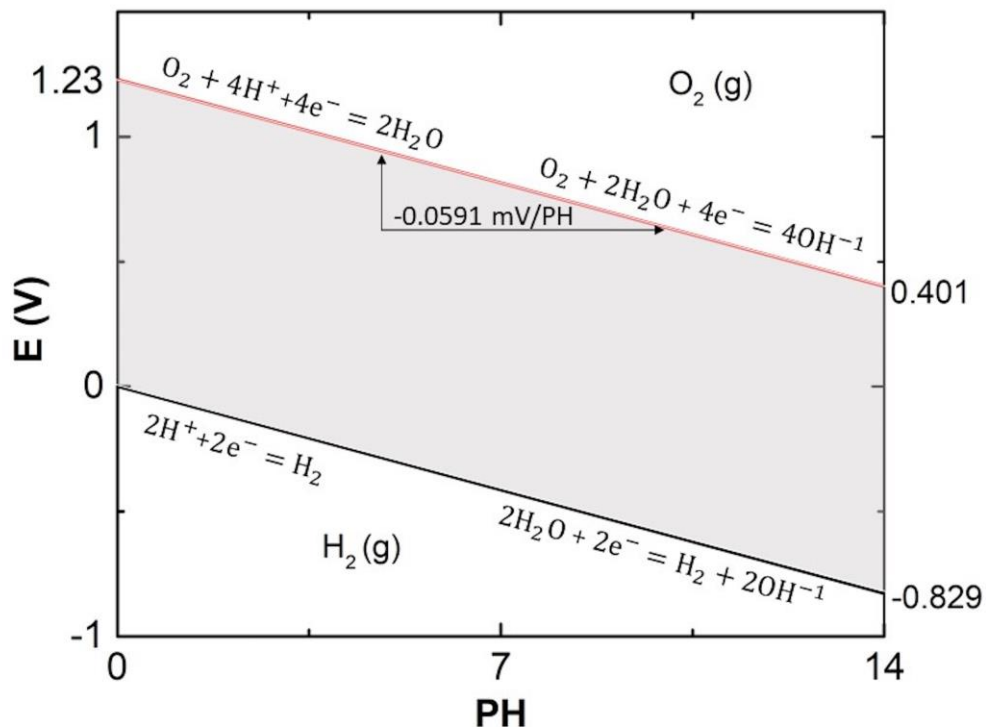


Figure 8 Pourbaix diagram for water at standard temperature and pressure.

must be noble metal because its relatively high kinetics and better electrochemical stability.^[90]

Kinetically, the whole reaction is uphill process and requires an energy input of 286 KJ mol⁻¹ at room temperature and 1 atm pressure. Iridium/Ruthenium dioxide is the state-of-the-art OER electrocatalysts.^[91] The standard potential for OER at PH 0 is 1.23 V vs. standard hydrogen electrode, which is the biggest obstacle for water electrolysis. As the reaction proceed in acid or alkaline solution, the potential increases by shifting 59 mV for each rising PH unit according to the Nernst equation

$$E = E^\circ - \frac{RT}{nF} \ln \frac{[Red]}{[Ox]}, \quad (1.17)$$

where E, E[°], R, T, n, F, [Red], and [Ox] are the potential, potential at standard conditions, ideal gas constant, working temperature in Kelvin, number of moles of electrons

participating in each mole of reaction, Faraday constant, concentration of reduced molecules and concentration of oxidized molecules.^[12] Fig. 8 shows Pourbaix diagram, and the stability region for water was limited by the solid red and black lines in a shadow region. The solid red and black lines are referred to the oxygen evolution reaction and hydrogen evolution reaction, respectively. The potential E is always changing with PH value regardless of the highly reducing condition (HER, $E = -0.0591\text{PH}(\text{V})$) or highly oxidizing conditions (OER, $E = 1.23\text{V} - 0.0591\text{PH}(\text{V})$). Reversible hydrogen electrode (RHE) was introduced to avoid requirement of measured potential changing with the PH value, so the theoretical potential for OER is always 1.23 V vs. RHE and HER is 0 V vs. RHE at all PH values.

Cell efficiency usually is defined as the ratio of energy directly used for hydrogen and oxygen production to the total energy input, and it can be approximated that the

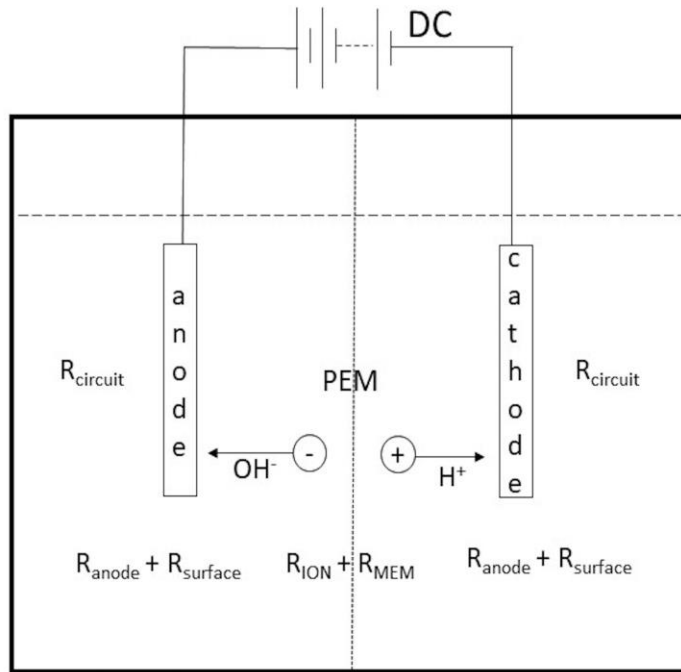


Figure 9 The distribution of charge resistances in the water splitting.

percentage of effective voltage for water dissociation in the whole voltage applied on electrolysis cell. Equation was as Faradic efficiency,

$$\eta_F = \frac{E_{\Delta G}}{E_{cell}}, \quad (1.18)$$

where $E_{\Delta G}$ and E_{cell} are Gibbs free energy change and cell voltage input. In order to get higher efficiency, energy loss should be avoided as much as possible, which primarily come from Joule's heat from the resistance in Fig. 9.

Good catalysts could protect water splitting from the large energy consumption. It has been proposed that catalysts for widespread application should satisfy requirements as following: a) low overpotential for large current density, b) chemical stability in the electrolyte, c) robust mechanical strength and no peeling off, d) long time durability and no potential drift with time, e) simple and eco-friendly preparation process at a low cost.^[92]^[93] Noble metal (Pt, Ir, and Ru) and their oxides (IrO_2 and RuO_2) display low onset potential and highly efficient performance for HER and OER, but high cost and extreme scarcity restricts their application, and lead to few percentage share of worldwide hydrogen production by water splitting.^[94] Good catalysts could be synthesized by well controlling three critical factors, as many active sites as possible by increasing the surface area, superior electrical conductivity of electrode, and suitable absorption energy of hydrogen ions. The strategies of optimizing three factors will be talked in next part.

1.4.2 Strategies to improve efficiency of water electrolysis

1.4.2.1 Energy barrier and resistance

Electrons constantly flow along the whole circuit during the electrochemical reaction, indicating charge transfer involved every single process of water electrolysis. It

must overcome the resistance and the barrier to form hydrogen and oxygen by virtue of applied potential. As shown in Fig. 9, the resistance includes the resistance of the electrolyte ($R_{\text{ION}} + R_{\text{MEM}}$), which refers to the ions transfer in the electrolyte, resistance of circuit ($R_{\text{electrode}} + R_{\text{circuit}}$), and interface resistance between electrode and electrolyte (R_{surface}), which mainly refer to the ions exchange between the electrolyte and the active sites.^[95] The lower resistance in the circuit and electrode avoid high-energy loss from the joule heat and promote electron transfer efficiency. The major concerns involve the resistance of anode and cathode. The catalysts normally grow on or bind with the support materials as the electrodes, good contact guarantee electron transfer between electrode and active site. It should be mentioned that bubbles covering on the actives site also lead to high resistance on the surface, so it's imperative to get rid of these bubbles instantly from the active site after H_2 or O_2 forming.^[96] Xu. *et al.* studied S-doped effect on HER performance of MoSe_2 nanosheet, and found out S effectively reduced the charge transfer resistance from 145.02Ω to 35.66Ω , which contributes to faster HER kinetics.^[97]

1.4.2.2 Large electrochemical active surface area (ECSA)

Large ECSA can provide more positions and edges to expose active sites for adsorption and desorption of hydrogen, hydroxide and intermediates.^[98, 99] The straight way to enhance ECSA is to produce nano-structured catalysts, such as nanowires,^[100, 101] core shell,^[102] nanosheets,^[103] and sandwich structures^[98] *etc.* Most well-investigated NiSe_2 for HER has been formed in different structures like nanosheets, nanoparticle, and nanowires, which are responsible for their reported large ECSA, leading to highly efficient performance.

Three-dimensional structure metal substrates such as metal foam and metal sheet are also adopted as support, and efficient catalysts can be grown on by hydrothermal or chemical vapor transport, or able to bound with them to increase the active catalysts. Zhou *et al.* have devoted lots of efforts to synthesize good catalysts on Ni foam for HER and OER, including NiSe₂/Ni,^[17] WSSe/NiSe₂,^[29] Ni₂P/CoP/Ni,^[104] NiFeOOH/Ni^[92] *etc.* Many of them exhibit remarkable achievement. For example, 3D structure NiFeOOH synthesized based on Ni foam using simple room-temperature stirring method, reaches current density of 1000 mA/cm² at a potential of 258 mV, and also exhibit excellent durability.^[92]

Electrochemical active surface area of electrodes usually is proportional to the double layer capacitance (C_{dl}), which can be extracted from the cyclic voltammetry (CV) in the potential range where no Faradaic current is observed. The difference of positive current at oxidation and negative current at reduction is linearly dependent on the different CV scanning rate. The half value of the fitting slope was considered as the double-layer capacitance.

1.4.2.3 Free energy of adsorption and desorption

The free energy of adsorption normally indicates the intrinsic properties of the catalyst, which commonly are suggested by the Tafel slope and exchange current density.

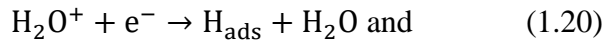
The Tafel equation can be written as

$$\eta = a + b \log i, \quad (1.19)$$

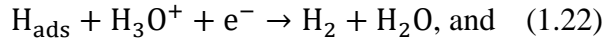
where $a = \frac{2.3RT}{\alpha F} \log i_0$, and $b = \frac{-2.3RT}{\alpha F}$, i , i_0 , α , F , R , and T refer to the current density, exchange current density, transfer coefficient (its value lies between 0 and 1 for one-electron reaction), Faraday constant, gas constant and working temperature in Kelvin.^[105]

The Tafel slope are obtained by the linear relationship between the overpotential and

logarithm of current density and exchange current density i_0 , which is the current of the reversible water splitting reaction and can be acquired by the interception of slope with x axis. Tafel slope and exchange current density are the indication of the kinetics of catalysts and rate-determining step in the whole electrolysis process.^[21, 106] A small Tafel slope and large exchange current density are preferred as active kinetics and low overpotential barrier. It has been proposed that HER in acid solution contains four possible steps, Volmer step



Heyrovsky step



Tafel step



where H_{ads} and H_{ads}^* denotes adsorbed hydrogen and active adsorbed hydrogen on the catalyst site. Eqn. 1.21 is the Volmer equation, wherein α is assumed to be 0.5, and Tafel slope for this step was estimated to be 120 mV dec^{-1} ($b = 2.3 \frac{RT}{\alpha F}$). The step describes H^+ is absorbed onto the active site of the surface *via* electrochemical discharge step. Eqn. 1.22 is proposed to be the spill-over process, which mainly present the migration of unstable adsorbed H_{ads}^* to a stable site. Tafel slope for this step is estimated to be around 60 mV . Eqn. 1.23 and Eqn. 1.24 are identified as Heyrovsky and Tafel reactions, respectively.^[107, 108] And the Tafel slope are associated with these two steps are 40 mV dec^{-1} and 30 mV dec^{-1} , respectively. H_2 is generated through electrochemical desorption. Tafel slope of 120 , 40 , and 30 mV dec^{-1} , are referred to be Volmer, Heyrovsky and Tafel step. For example, Volmer step would be the rate-determining step when the Tafel slope is around 120 mV

dec^{-1} . Rate determining step may involve into the Volmer-spillover-Heyrovsky process when the Tafel slope is fall in the range of 50-60 mV dec^{-1} . Noble metal Pt normally exhibit 30 mV dec^{-1} of Tafel slope, which suggest that Volmer-Tafel reaction process is the rate-determining step.

Low Tafel slope is strongly correlated with the free energy of hydrogen or hydrogen oxide ions adsorbed to the catalysts surface. It is always an effective way to obtain low Tafel slope by changing the electronic structure and lowering the free energy of hydrogen adsorption. First principle density function theory often was hired to evaluate the ΔG_{H} , which is a quantitative parameter to gauge the bonding strength of hydrogen and metal.^[13] CoP has been experimentally demonstrated to be a bifunctional catalyst for overall water splitting. DFT calculation displays that it is not stable for Hydrogen ion adsorbed at P site, and ΔG_{H} is nearly -0.14 eV once hydrogen was adsorbed by Co, which is much larger than that of Pt, -0.009 eV. However, this value can be suddenly lowered to -0.088 eV at Co site when partial Co was substituted by Fe, giving rise to weakened H-Co binding strength and promote ΔG_{H} toward zero accordingly.^[109] Hou. *et al.* also investigate the effect of vacancies and P displacement of Se in cobalt phosphoselenide on electronic structure. It was claimed that the weakest H-bond was obtained after P substituting due to the longest length of H bond. Besides, P-Co bond induced one of Co atoms transition from oxidation state to the reduction states, which is helpful to lower the Coulombic potential for atom hydrogen adsorption and shorten the distance between two neighboring H atoms for hydrogen desorption in HER. The synergistic effects of vacancies and P substitution lead to 10 mA cm^{-2} at overpotential 150 mV.^[110]

Chapter 2 Characterization

2.1 Thermoelectric materials

2.1.1 Thermoelectric properties characterization

The electric resistance and the Seebeck coefficient were measured by a commercial system ZEM3 (ZEM3, ULVAC) with dimensions of about $2\text{ mm} \times 2\text{ mm} \times 12\text{ mm}$. Fig. 10 shows the schematic of resistance and Seebeck coefficient measurement in ZEM3. Electric resistance was tested by direct current (DC) four-probe method. When a current was injected into the sample from the blocks, potential ΔV between the two thermocouple-sample contact points can be read from thermocouple probes. Seebeck was obtained by static DC method. When a temperature difference was applied on the sample through the heater concealed in the bottom block, a thermal electromotive force dV was subtracted from two thermocouple probes. Thermal conductivity was calculated by $\kappa = DC_p\rho$, where D is

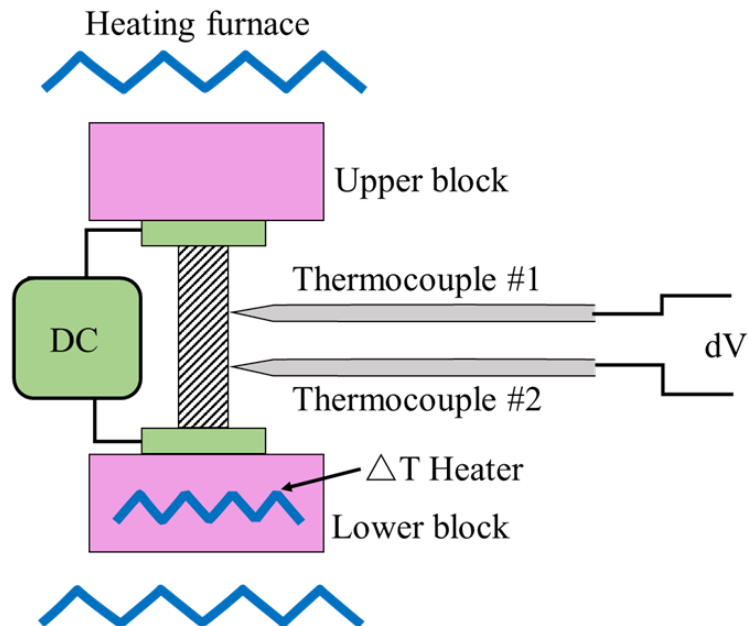


Figure 10 Schematic of measurement principle of Seebeck coefficient and electrical conductivity.

the thermal diffusivity determined by Laser flash technology (LFA 457, Netzsch). For most of thermoelectric semiconductor, pellets with diameter 12.7 mm and thickness 1.5 mm or lower are prepared for the diffusivity measurement. The specific heat C_p was obtained by differential scanning calorimetry thermal analyzer (DSC 404C, Netzsch), and density ρ was measured by Archimedes method. Hall coefficient R_H at room temperature was measured by a Physical Properties Measurement System (PPMS D060, Quantum Design) with four-probe configuration. Thickness of samples was controlled below 0.4 mm, and the magnetic field sweeping is controlled between +3 T and -3 T. The Hall carrier concentration n_H and mobility μ_H were calculated by $n_H = \frac{1}{eR_H}$ and $\mu_H = \sigma R_H$.

2.1.2 Phase and microstructure characterization

X-ray diffraction spectra analysis of pellets and powder were conducted on a PANalytical multipurpose diffractometer with an X'celerator detector (PANalytical X'Pert Pro). Microstructures were characterized by scanning electron microscopy (SEM Leo 1525 Gemini FEG, Zeiss and FE-SEM, LEO 1525) and transmission electron microscope (JEOL 2010F). Microstructure characterization was also carried out by JEM-ARM 200F TEM. This microscope was equipped with a Cold FEG source for STEM and double-sextupole Cs correctors for TEM and STEM, respectively. Samples of thermoelectric materials for the TEM were prepared by a standard procedure, including mechanical polish, dimpling, followed by ion-beam milling. Specimens of electrochemical water splitting for TEM was peeled off by ultrasonic or blades, and then dispersed on copper grid by ethanol.

2.2 Water splitting

2.2.1 Electrochemical activity characterization

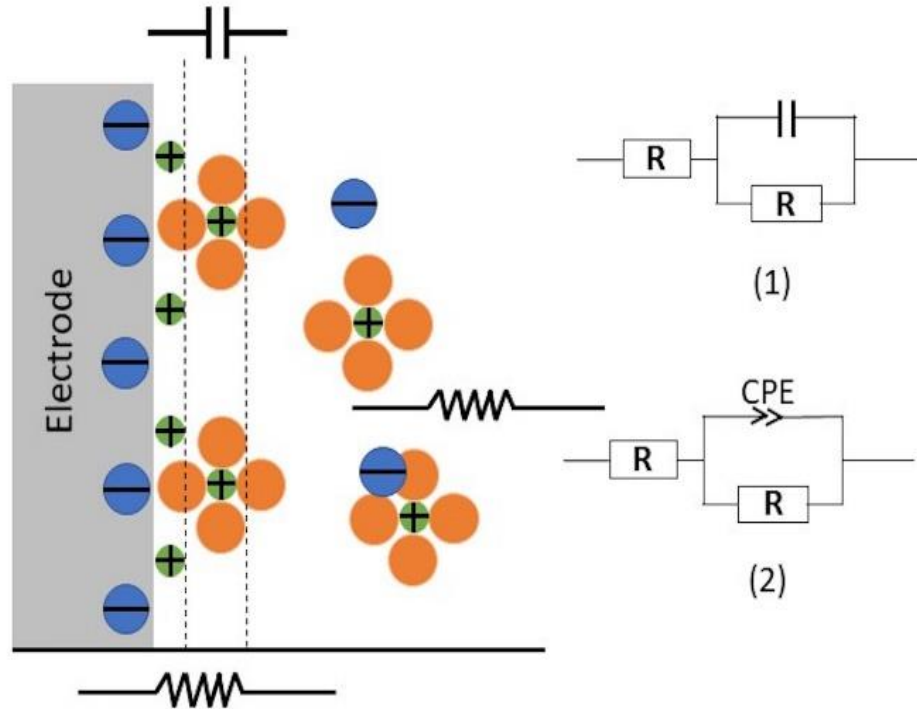


Figure 11 Schematic of double layer structure and the corresponded equivalent circuit during water splitting.

The electrochemical tests were performed via typical three-electrode configuration in 100 mL 1 M KOH electrolyte. Pt and Hg/HgO were adopted as counter and reference electrode, respectively. The measured potentials vs. Hg/HgO was converted to RHE by Nernst equation,

$$E_{\text{RHE}} = E_{\text{Hg/HgO}} + 0.059\text{pH} + \varphi_{\text{HgO}}^{\ominus}, \quad (2.1)$$

where $E_{\text{Hg/HgO}}$, and $\varphi_{\text{HgO}}^{\ominus}$ are the measured potential and standard potential of HgO. The polarization curves for HER and OER were recorded by linear sweep voltammetry with a scan rate of 2.0 mV s^{-1} in the range $0.075 \sim 0.425 \text{ V vs. RHE}$ / $1.125 \sim 1.625 \text{ V vs. RHE}$,

respectively. And the scan rate for activation was set to 50 mV s^{-1} . Besides, all the electrocatalytic measurements are performed at room temperature and iR error was compensated by current interruption method. To evaluating electrochemical test system, commercial Ni foam was adopted as a reference for the polarization curves.

2.2.2 Electrochemical impedance spectroscopy

Electrochemical impedance spectroscopy (EIS) specifically is related to internal charge-transfer resistance of electrode and charge transfer resistance at the electrode/electrolyte interface in the electrochemical cell. When a voltage is applied on electrodes in the electrolyte, two layers of ions with opposing polarity form, which is the double layer. One layer is at the surface of electrode and the other locates in the electrolyte. The structure of the double layer is similar with an electrical condenser constituted by two

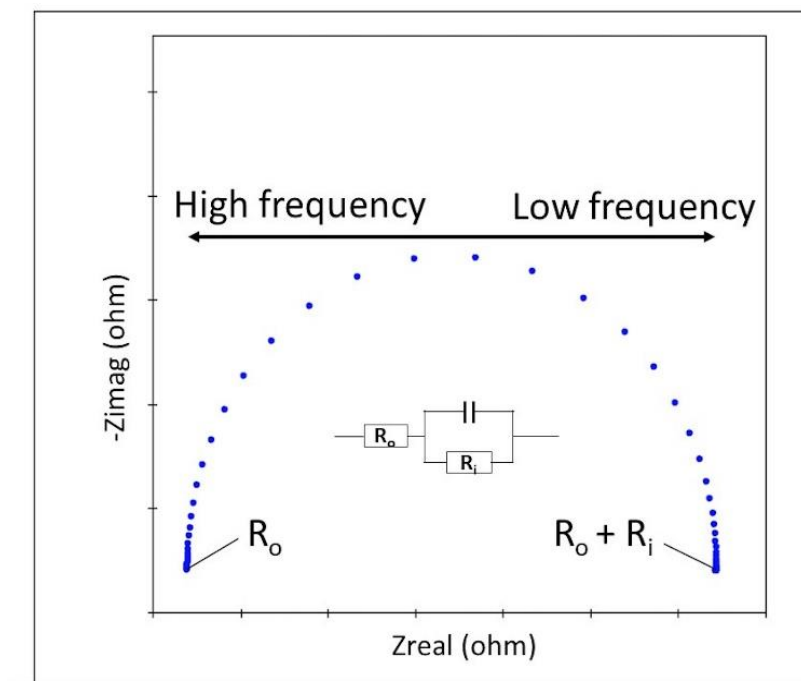


Figure 12 Nyquist plots fitting with simplifying Randles equivalent circuit.

charged areas separated by a dielectric. Formed two-double layer functionally equals to a capacitance, which plays an important role

The equivalent circuit was shown in Fig. 11, where the capacitance and the resistance are corresponding to the double layer, and an additional resistance equals to the ohmic drop due to the electron transfer resistance from the electrolyte. Electrochemical impedance is usually applied an AC potential with changed frequency to an electrochemical cell and measure the resistance through the cell. The frequency normally ranges between 100 KHz to 0.1 Hz (Fig. 12). Equivalent circuit (1) in Fig. 12 just describes the ideal situation of capacitor, but the capacitance of double layer was possibly changed with ion concentration, surface morphology and temperature electrolyte. The constant phase element usually was recommended to substitute the capacitor in the equivalent circuit.

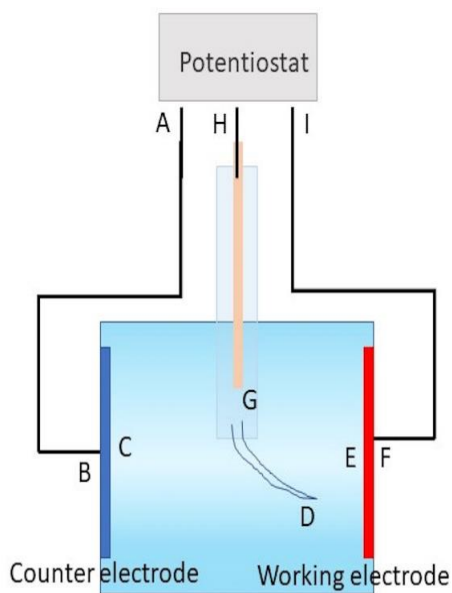


Figure 13 Three electrode configuration system for electrochemical measurement.

EIS data is presented through the Nyquist Plot, then matched with the equivalent circuit by the model fitting until the curve generated fit well with the measured data. The internal charge-transfer resistance of electrode, charge transfer resistance at the electrode/electrolyte interface, and the capacitance of double layer can be obtained.

2.2.3 iR compensation

iR compensation is used for correcting voltage drop induced by complicated electrochemical system in electrolysis cell, especially for the situation where we have large current and unregular geometry shape. Fig.13 shows the normal electrolysis cell, and its equivalent circuit was presented in Fig. 14. During the electrolysis process, we want to control and measure the voltage between E and F, which can be expressed as

$$V_{f-e} = V_f - V_e = V_{measure} - I_{cell} \times R_o - V_{oc}, \quad (2.2)$$

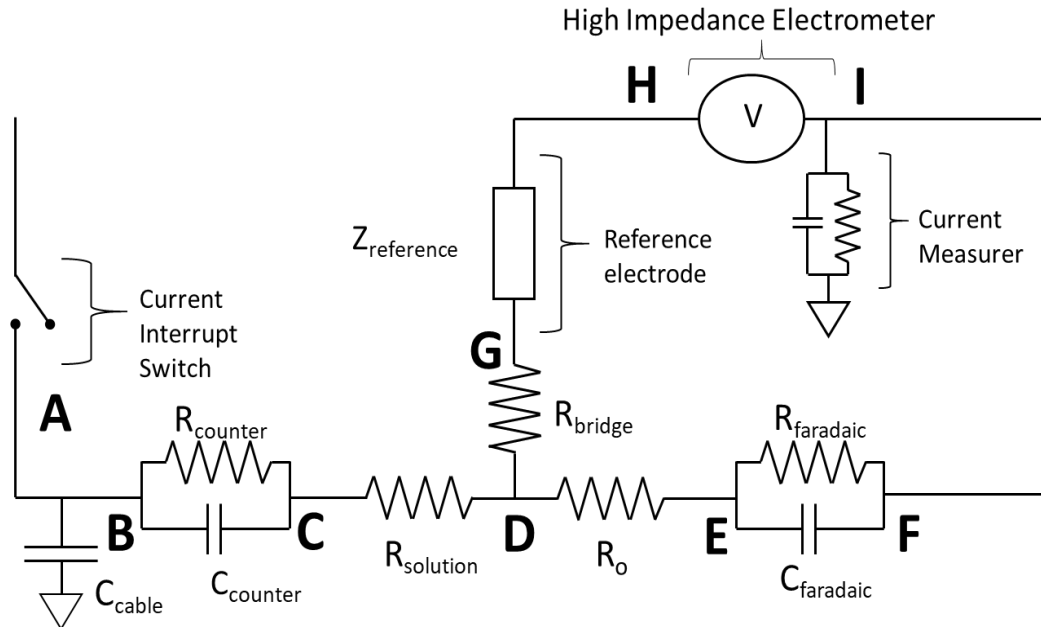


Figure 14 Schematic of equivalent circuit of three-electrodes configuration measurement in electrolysis cell.

where V_e , and V_f are the voltage of electrolyte surface and metal surface of the working electrode, respectively. V_{measure} is voltage of working electrode that we pursue, and V_{oc} , known as open-circuit voltage, is a constant offset voltage caused by the potential difference between working electrode and reference electrode. I_{cell} and R_o are the current flowing through the circuit and resistance between the tip of the Luggin capillary and the electrolyte surface of the working electrode. In the equation, V_{measure} , I_{cell} , and V_{oc} can be read by the equipment, and iR compensation stands for the $I_{\text{cell}} \times R_o$. From the equation, it can be concluded that iR compensation applies an enormous influence on the output voltage, but it is very difficult to correct this existed error instantaneously during electrolysis because of sophisticated chemical and physical situation. Fortunately, there are two classic methods offered by most of electrochemical workstation to carry out iR compensation, known as current interrupt iR compensation (CI), and positive feedback iR compensation (PF). CI propose an instantaneous method to obtain the voltage drop across

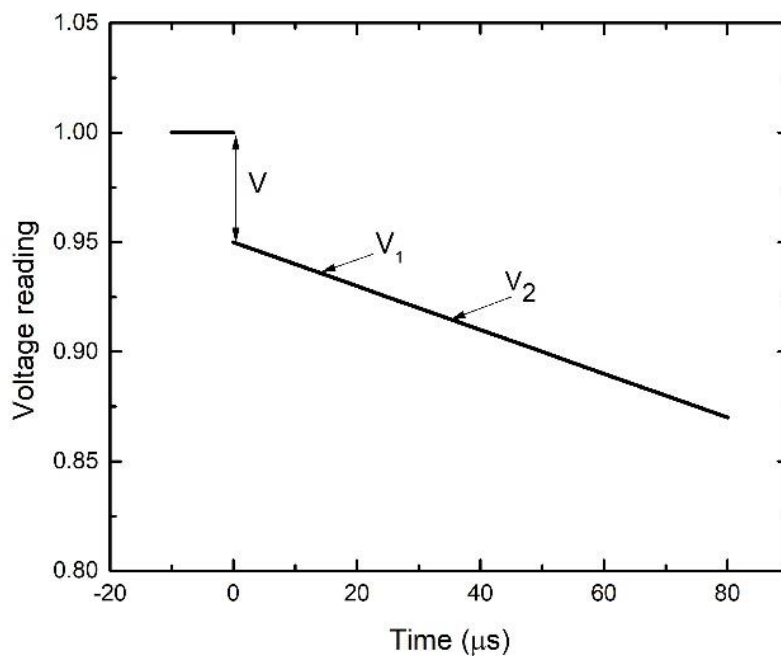


Figure 15 Current interruption for iR compensation.

the R_o . The moment that current in the electrolyte cell is cut off and put back (duration is about $10 \mu\text{s}$ to $30000 \mu\text{s}$), the cell voltage will be read immediately before and after this current interruption. Due to the Faradaic capacitor's characteristics in the equivalent circuit (solid back square), the signal of cell voltage was presented in Fig. 15, which is referred to the voltage drop by R_o . The estimated V_o is calculated by

$$V_o = V_1 + (V_1 - V_2), \quad (2.3)$$

Table 1 Advantages and disadvantages of current interruption and positive feedback.

iR compensation	Advantages	Disadvantages
Current Interruption	<ul style="list-style-type: none"> • No prior knowledge of R_o is required • R_o can change during an experiment • Compensation is independent of the current range • Scan parameters such as ramp limits and scan rates are corrected automatically 	<ul style="list-style-type: none"> • Need for a large faradiac capacitance • Time-per-point limitations • Rfaradiac should be larger than R_o • Value of R_o must be less than a limit
Positive Feedback	<ul style="list-style-type: none"> • Reasonable in very fast measurement • Scan parameters such as ramp limits and scan rates are corrected 	<ul style="list-style-type: none"> • R_o needs to be known before beginning test • Error occur if R_o changes during the measurement • The current range must not change during the experiment • PF can lead to potentiostat oscillation

It can be observed that the system is very sensitive and precise from the equation and the figure due to the extremely short interval, like from a few millivolts to a few hundred millivolts, from which the voltage reading is also small. There is a big possibility of the

noise of circuit or from the cell will affect the results. Another concern is related to the capacitance. The delay of Faradaic capacitor of working electrode during the interval would lead to voltage offset. So fast sampling speed is recommended to avoid the voltage drift. It should be mentioned that cable capacitance, which usually cause the overestimated V_o . Discharging of capacitance of cable before testing or taking a log(time) scale to confirm all the cell cables discharged would be helpful.

PF iR compensation are more applicable for fast phenomena. This technique is an additional analog feedback path in potentiostat. R_o is acquired by EIS before conducting measurement by assuming the cell impedance at high frequency is R_o . During PF iR compensation, output voltage is corrected according to the R_o and cell current. The advantages and disadvantages of CI and PF iR compensation was listed as following

2.2.4 X-ray Photoelectron Spectroscopy

The X-Ray Photoelectron Spectroscopy (XPS) was conducted to investigate the surface chemical state and elemental composition of samples. X-ray photoelectron spectra were collected with PHI Quantera XPS scanning microprobe with an Al monochromatic K_α source (15 KV, 20 mA). The chamber pressure was well controlled above 5×10^{-8} Torr.

2.2.4 Raman Spectroscopy

Raman spectra was used for identifying the hydroxides and (oxy) hydroxides molecular due to its high sensitivity to oxygen vibration. The spectra were collected using a Renishaw inVia Raman spectroscope employing a He-Ne laser with an excitation wavelength of 633 nm. The laser power was set at 1 mW and the spot size of the beam on the surface was around 1-2 μm . The total acquisition time was 60 s. Before the

measurements were taken, the spectra shifts were calibrated by the silicon phonon mode (520.7 cm^{-1}).

Chapter 3 Achieving high thermoelectric performance of Mg_3Sb_2 -based compounds by grain alignment and carrier concentration optimization.

3.1 Background

Mg_3Sb_2 -based Zintl compounds are among the most promising thermoelectric materials for mid-temperature (500-800 K) applications because of their abundance, nontoxicity, and low cost.^{[111] [112]} Over the past two decades, most of the studies on Mg_3Sb_2 have been focused on achieving higher p-type performance while the n-type counterparts were considered to be impossible to make. Recently, n-type $\text{Mg}_{3.2}\text{Sb}_{1.5}\text{Bi}_{0.49}\text{Te}_{0.01}$ with a peak ZT of ~ 1.5 at 723 K was reported by Tamaki *et al.*^[79] The excess Mg in the initial composition was considered critical for suppressing the Mg vacancies and lifting the Fermi level upward to the conduction band. N-type Mg_3Sb_2 was also realized by doping of chalcogens (Te, S, Se) at the Sb site based on $\text{Mg}_3\text{Sb}_{1.5}\text{Bi}_{0.5}$ solid solution without extra Mg.^[113, 114] Compared to the p-type Mg_3Sb_2 compounds, the n-type counterparts exhibit much better electrical conductivity with higher carrier concentration and larger N_V/m^* (N_V is the number of valleys and m^* refers to band effective mass), which are beneficial for higher thermoelectric performance.^[115]

Mg_3Sb_2 has a trigonal crystal structure of anti- La_2O_3 ($P\bar{3}m1$) type at room temperature. It can be observed in Fig. 16 that an anionic $[\text{Mg}_2\text{Sb}_2]^{2-}$ layer and a cationic Mg^{2+} sheet stack along the c direction, which gives rise to a typical layered structure. Mg^{2+} has two inequivalent positions. The first Mg^{2+} site in the cationic layer is bonded with six

equivalent Sb^{3-} atoms to form MgSb_6 octahedra, where all the Mg-Sb bond lengths are 0.312 nm.^[112, 116] The second Mg^{2+} is bonded with four equivalent Sb^{3-} atoms to form MgSb_4 tetrahedra. There are three short length of 0.285 nm and one long length of 0.296 nm. It is also observed that there is a big empty space located in the $[\text{Mg}_2\text{Sb}_2]^{2-}$ layer, which was proposed to be an interstitial site, and can be filled with “rattling” element to produce PGEC effect. However, it is still a controversial concept, because it was claimed that it needed a large formation energy to take this interstitial site. The consequence of this complicated structure is the low thermal conductivity in the whole working temperature range. It has been reported that the thermal conductivity of n-type Mg_3Sb_2 Zintl compounds normally range between 1 ~ 1.2 $\text{W m}^{-1} \text{K}^{-1}$ at room temperature.^[117]

By the advantages of intrinsic high N_V/m^* and low thermal conductivity, n-type Mg_3Sb_2 Zintl compounds has achieved significant result, ZT value of 1.5 ~ 1.6 at 773 K.^[40] Further improvement is still required for possible commercialization. Grain alignment and effective donor are introduced to enhance the thermoelectric performance of n-type $\text{Mg}_3\text{Sb}_{1.5}\text{Bi}_{0.5}$ based compounds in the following part.

3.2 Grain alignment promotes the thermoelectric performance of n-type $\text{Mg}_3\text{Sb}_{1.5}\text{Bi}_{0.5}$ compounds

3.2.2 Introduction

Thermoelectric materials with the layered structure, such as SnSe ,^[118] Bi_2Te_3 ,^[119] BiCuSeO ,^[80] and Mg_3Sb_2 ,^[120] the lattice thermal conductivities are intrinsically lower in the direction perpendicular to the layer due to stronger phonon scattering and also lower carrier mobility in this direction. Higher carrier mobility can be obtained parallel to the layer where materials usually exhibit higher power factor and higher output power

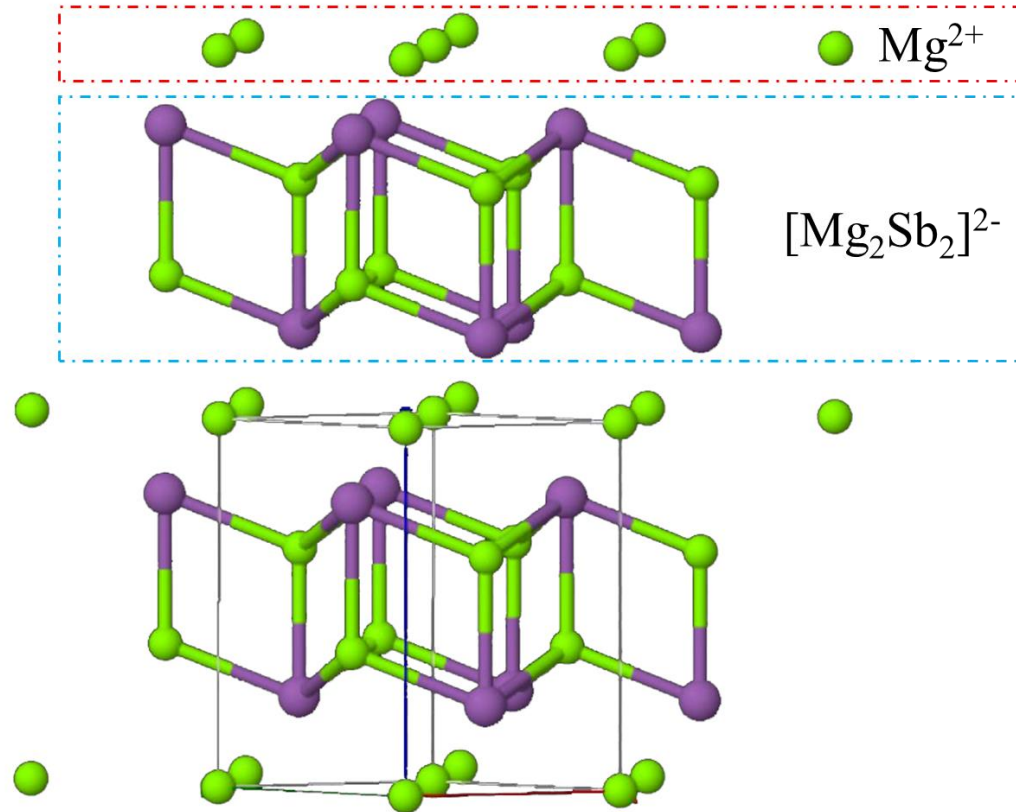


Figure 16 Crystal structure of Mg₃Sb₂-based Zintl compounds.

density.^[121] Therefore, it is possible to enhance the power factor and ZT of layered materials through manipulation of the grain orientation. It has been demonstrated that the performances of thermoelectric materials with the layered structure are improved by texturing to partially align a specific direction during hot forging.^[122] The majority carrier would encounter less scattering in the layer, leading to higher mobility and electrical conductivity and therefore power factor. Layered materials, such as Bi₂Te₃,^[123] BiCuSeO,^[124] and SnSe, showed significantly enhanced thermoelectric performances as a result of enhanced Hall mobility. For example, the Hall mobility of textured Bi₂Te₃ was significantly increased from 152 cm² V⁻¹ s⁻¹ to 683 cm² V⁻¹ s⁻¹ with increased temperature.^[123] Sui *et al.* doubled the Hall mobility from 2 cm² V⁻¹ s⁻¹ to 4 cm² V⁻¹ s⁻¹ after texturing was obtained in BiCuSeO, which boosted ZT to 1.4 at 923 K.^[124] Recently, the n-

type $\text{Mg}_{3.2}\text{Sb}_{1.5}\text{Bi}_{0.49}\text{Te}_{0.01}$ Zintl phase with high performance was fabricated successfully by Tamaki *et al.*, where the power factor was only $5 \mu\text{W cm}^{-1} \text{K}^{-2}$ at room temperature due to the low electrical conductivity. Then, it was reported that the power factor was improved to $14 \mu\text{W cm}^{-1} \text{K}^{-2}$ in $\text{Mg}_{3.1}\text{Nb}_{0.1}\text{Sb}_{1.5}\text{Bi}_{0.49}\text{Te}_{0.01}$ due to the suppression of ionized impurity scattering, leading to a noticeably improved Hall mobility from $19 \text{ cm}^2 \text{V}^{-1} \text{s}^{-1}$ to $77 \text{ cm}^2 \text{V}^{-1} \text{s}^{-1}$. According to the recent investigation on the deformation mechanism of Mg_3Sb_2 , the weak ionic bond between Mg^{2+} and $[\text{Mg}_2\text{Sb}_2]^{2-}$ layers can lead to easy slipping between the different $[\text{Mg}_2\text{Sb}_2]^{2-}$ layers under shear deformation.^[120]

In this paper, we studied hot forging on $\text{Mg}_{3.1}\text{Nb}_{0.1}\text{Sb}_{1.5}\text{Bi}_{0.49}\text{Te}_{0.01}$ to improve the grain alignment degree in the (00l) plane and therefore to reduce the carrier scattering factor. Our results indeed showed that some texturing was achieved in n-type $\text{Mg}_{3.1}\text{Nb}_{0.1}\text{Sb}_{1.5}\text{Bi}_{0.49}\text{Te}_{0.01}$ to further improve thermoelectric properties. The Hall mobility was more than 50% higher than that of the materials without texturing. Consequently, the power factor of the textured samples was increased to $18 \mu\text{W cm}^{-1} \text{K}^{-2}$ at room temperature, leading to also improved average ZT .

3.2.3 Experiment

3.2.3.1 Synthesis

Materials of high purity Magnesium turnings (Alfa Aesar, 99.9%), Niobium powder (Alfa Aesar, 99.9%), Bismuth chunks (Sigma Aldrich, 99.999%), Tellurium chunks (Sigma Aldrich, 99.999%), and Antimony chunks (Sigma Aldrich, 99.999%) were weighed according to the nominal stoichiometry of $\text{Mg}_{3.1}\text{Nb}_{0.1}\text{Sb}_{1.5}\text{Bi}_{0.49}\text{Te}_{0.01}$. All the weighed materials were loaded directly into a stainless-steel vial (Spex 8007, stainless steel grinding vial) with the oxygen level less than 0.1 ppm and then ball milled for 10 h. Then,

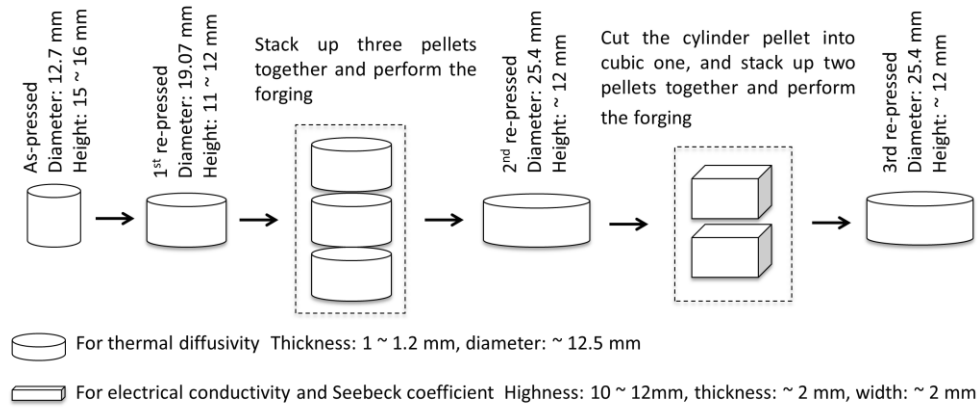


Figure 17 Schematic of hot pressing and hot forging.

the powders were pressed into dense pellets by DC hot pressing followed by hot forging. The powder was put into a graphite die with inner diameter of 12.7 mm and consolidated at 650 °C under 65 MPa pressure, named as “as-pressed.” The as-pressed ingot was then loaded into a graphite die with inner diameter of 19.05 mm and forged at 675 °C under 65 MPa for the first forging, named as “1st re-pressed.” (Fig. 17) Then, it was placed into a die with inner diameter of 25.4 mm at 700 °C under the same pressure for the second time forging, named as “2nd re-pressed.” A third time forging was also carried out under the same conditions as used in the 2nd forging, named as “3rd re-pressed”. The bar and coin-shaped samples for measurements were cut in the plane perpendicular and parallel to the press direction for electrical and thermal property characterizations. For simplicity, the perpendicular and parallel to the press directions were abbreviated as “⊥P” and “∥P”, respectively. Correspondingly, the as-pressed samples are defined as “⊥P as-pressed” and “∥P as-pressed”, and samples with texture by 2nd re-pressed are referred to as “⊥P textured” and “∥P textured.”

3.2.3.2 Rietveld refinement and rocking curve

PXRD was also performed with Standard Reference Material (powder Si, $a = 0.5431179 \pm 0.000008$ nm, NIST) for Rietveld refinement, which was used for calibration of diffraction line positions and line shapes. Si (15%, volume ratio) were mixed with as-pressed sample and partially 2nd re-pressed sample's powder, respectively, and the data was collected from 20° to 130° with step 0.015° . The lattice parameters were refined by Fullprof 2010. Rocking curve was performed on Geigerflex D/max-B diffractometer (Rigaku), ω angle was collected from 3° to 22° degree with the 2θ was fixed at 24.4° .

3.2.3.4 Results and discussion

The X-ray diffraction patterns of the pellet samples in the plane perpendicular to the press direction are presented in Fig. 18(a). All the major diffraction peaks can be indexed as the anti-La₂O₃ structure except some minor peaks, which are identified as Nb impurities. It is noticeable that the relative intensity of the peak indexed as (001) is significantly stronger after hot forging. The ratio of the relative intensities of the (002) plane to that of the (101) plane is increased from 52% to 143% and that of the (004) plane is increased by three times, from 5.5% to 17.3% compared with that of the as-pressed samples, which indicates that reorientation of the (001) plane of the grains was realized by forging processing. To further demonstrate the achieved texturing, the rocking curve measurements of the (002) peak of the as-pressed and 2nd re-pressed samples were carried out. As shown in Fig. 18(b), the rocking curves of the (002) plane in the 2nd re-pressed samples showed a much stronger intensity and smaller Full Width at Half Maximum (FWHM) value in comparison with that of the as-pressed samples. The ratio of the integrated intensity of the rocking curves of the 2nd re-pressed/as-pressed is 2.5/1. Clearly, there is a significant

texturing of (002) by re-pressing. Besides, the PXRD was performed with Standard Reference Materials, and the lattice parameters of the as-pressed sample without texture ($a = 4.58377$, $c = 7.27362$) and the 2nd re-pressed sample with texture ($a = 4.58378$, $c = 7.27407$) show almost identical values, indicating that hot forging did not lead to atomic structure changes. Moreover, the ratio of (002) / (101) integrated intensity of the as-pressed and 2nd re-pressed powder samples is 1.265 and 1.293, respectively. The barely changed relative intensity in powder samples demonstrates that the relative intensity changes of the (002) / (101) plane in the 2nd re-pressed pellets result from the hot forging, rather than the

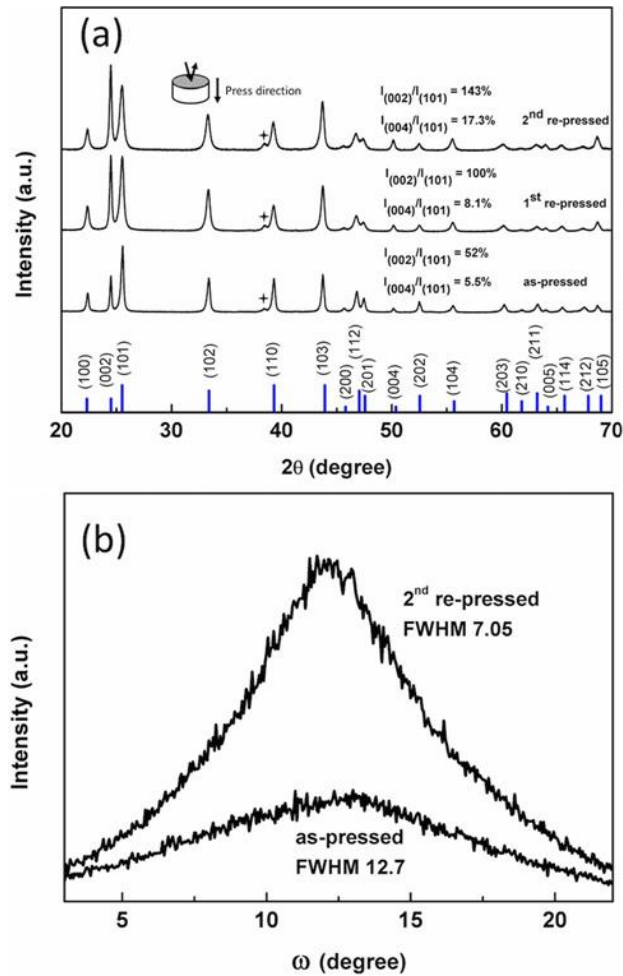


Figure 18 (a) XRD patterns of as-pressed and textured $\text{Mg}_{3.1}\text{Nb}_{0.1}\text{Sb}_{1.5}\text{Bi}_{0.49}\text{Te}_{0.01}$. (b) Rocking curves of the (002) plane in as-pressed and the 2nd re-pressed samples.

changes of Mg vacancies. Figures 19(a) and 19(b) show the SEM images of the freshly fractured surfaces of both the as-pressed sample and the textured sample in the plane parallel to the press direction, respectively. It seems that there is some orientation

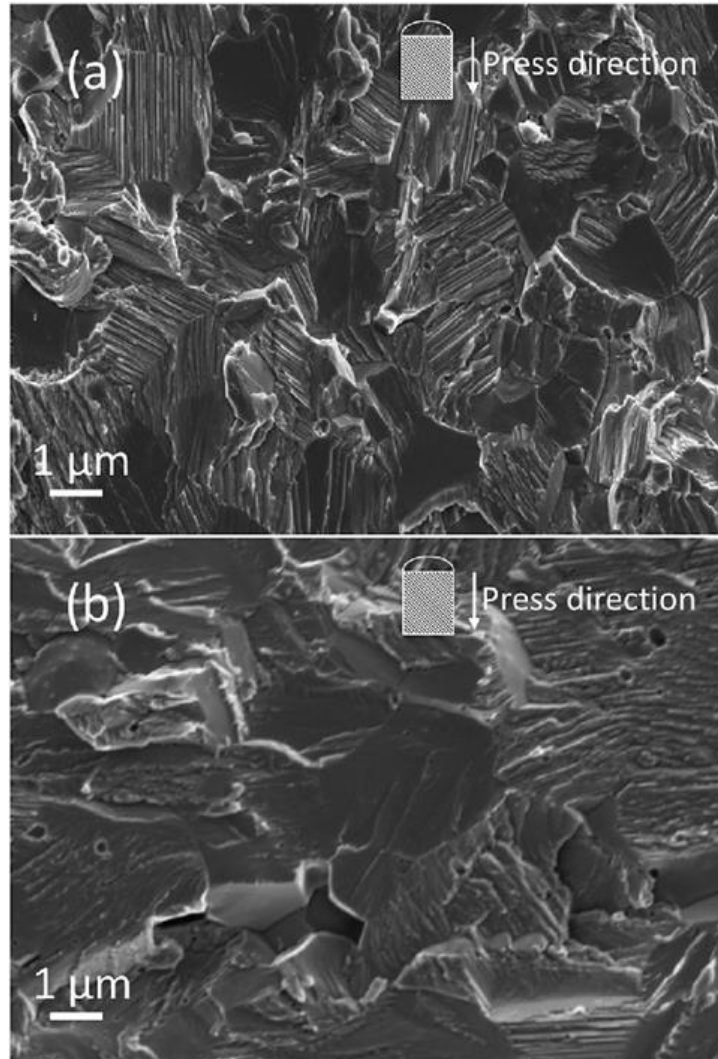


Figure 19 SEM images of the freshly fractured surface of the as-pressed sample (a) and textured sample (b) in the plane parallel to the press direction.

realignment in the textured samples, but not pronouncedly different, consistent with the XRD patterns.

Fig. 20 shows the temperature dependence of the electrical properties in the direction perpendicular and parallel to the press directions of samples with and without texture. Significant changes of electrical conductivity are observed in Fig. 20(a) below 473 K. The electrical conductivity of as-pressed samples shows obvious anisotropy below 473 K. Due to the intrinsic layered structure, carriers encounter less scattering in the (001) plane, resulting in larger mobility and electrical conductivity in the (001) plane (Table 2). It is interesting to find that the temperature-dependent electrical conductivities of the as-pressed samples are different from those of re-pressed samples at low temperature, which present noticeable mixed scattering by ionized impurities and acoustic phonons. According to our recent reports, the thermoelectric performances of n-type Mg_3Sb_2 -based Zintl compounds are very sensitive to the fabrication process due to the Mg vacancies.^[125, 126] The origin of ionized impurity scattering mainly comes from the Mg vacancies, which could be significantly suppressed by the re-pressing process. The weakened ionized scattering partly contributes to the improved mobility along in and out of the (001) plane and also higher electrical conductivity, which might be the main reason that textured samples exhibit higher electrical conductivity in both directions than those without texture. Another important factor that needs to be taken into account is the enlarged grain size, which was estimated by PXRD Rietveld refinement. The average grain size in the textured sample was increased more than 5% after hot forging. It is reported that the larger grain size shows the similar influences on the scattering mechanism at low temperature.^[127, 128] Besides, preferential grain alignment in the (001) plane contributes to the higher mobility in textured samples. As shown in Table 2, the Hall effect measurements confirm that mobility in the plane perpendicular to the hot press direction in the textured sample reached $105 \text{ cm}^2 \text{ V}^{-1}$

s^{-1} , almost 50% larger than that without texture. In the plane parallel to the hot press direction, mobility also reached $87 \text{ cm}^2 \text{ V}^{-1} \text{ s}^{-1}$, increased by 92% compared to that of the

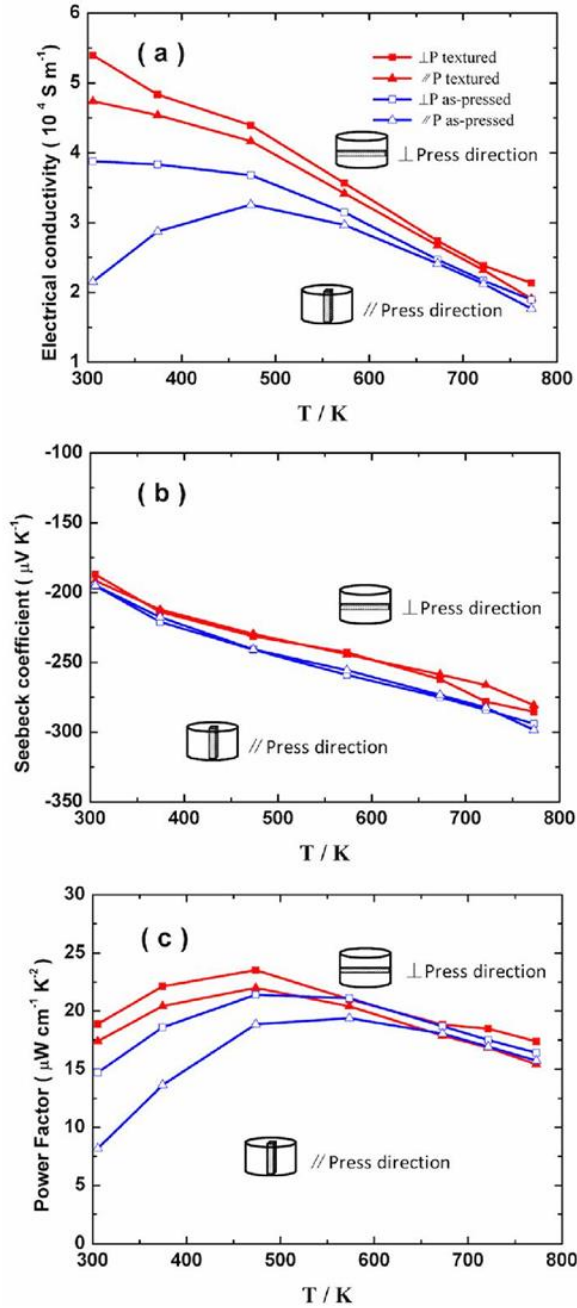


Figure 20 Temperature dependence of electrical conductivity (a), Seebeck coefficient (b) and power factor (c) of $\text{Mg}_{3.1}\text{Nb}_{0.1}\text{Sb}_{1.5}\text{Bi}_{0.49}\text{Te}_{0.01}$ with and without texture.

same direction without texture. Benefitting from the higher Hall mobility at room temperature, the electrical conductivities in the plane perpendicular and parallel to the hot press direction are increased by 40% and 100% compared to un-textured samples, respectively.

Table 2 Comparison of the Hall carrier concentration and mobility between the as-pressed and textured specimens.

	⊥P textured	∥P textured	⊥P as-pressed	∥P as-pressed
Hall carrier concentration (10^{19} cm^{-3})	3.2	3.4	3.3	3.4
Hall mobility ($\text{cm}^2 \text{ V}^{-1} \text{ s}^{-1}$)	105	87	71	40

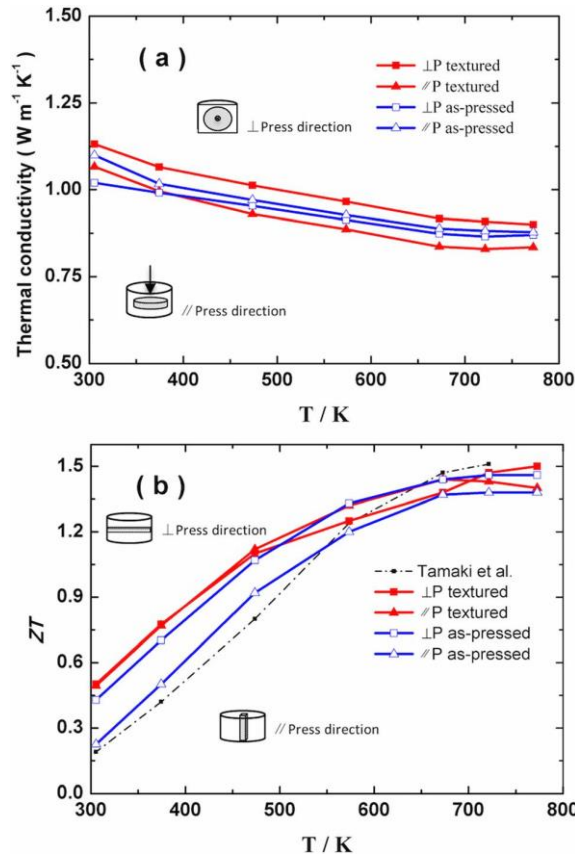


Figure 21 Temperature dependence of thermal conductivity (a) and ZT (b) of $\text{Mg}_{3.1}\text{Nb}_{0.1}\text{Sb}_{1.5}\text{Bi}_{0.49}\text{Te}_{0.01}$ with and without texture. Data of Tamaki et al. ($\text{Mg}_{3.2}\text{Sb}_{1.5}\text{Bi}_{0.49}\text{Te}_{0.01}$) were also included for comparison.

All Seebeck coefficients are negative over the whole temperature range, indicating that electrons are the majority carrier of electrical transport. Moreover, Seebeck coefficients are independent of the grain orientation, which is consistent with the calculated results. The calculated power factor ($S^2\sigma$) as a function of temperature is shown in Fig. 20(c). The textured sample in the plane perpendicular to the press direction shows a higher power factor, $18 \mu\text{W cm}^{-1} \text{K}^{-2}$ at room temperature and the highest power factor $24 \mu\text{W cm}^{-1} \text{K}^{-2}$ at 473 K, which are ascribed to the enhanced electrical conductivity. The power factor in the plane perpendicular to the press direction at room temperature is increased by 20% compared to that of the sample without texture in the same direction.

Figure 21(a) shows the temperature dependence of the total thermal conductivity along the different orientations. Thermal conductivity of the textured sample in the plane perpendicular to the press direction exhibits a higher value than that of other samples in the whole temperature range, which is mainly attributed to enhanced electrical conductivity. The textured sample from the plane parallel to the press direction exhibits a little higher thermal conductivity than that of the as-pressed sample along the same direction at room temperature due to the weaker ionized impurity scattering at low temperature. The temperature dependences of ZT are shown in Fig. 21(b). Benefitting from the higher power factor, the textured sample in the plane perpendicular to the hot press direction shows the best performance in the entire temperature range. The peak ZT reaches 1.5 at 773 K, which is comparable to the data reported by Tamaki *et al.*, but drastic improvement of ZT at below 600 K is observed in the textured samples in the plane perpendicular to the hot press direction, 0.5 at 300 K, which is 25% higher than that of $\text{Mg}_{3.1}\text{Nb}_{0.1}\text{Sb}_{1.5}\text{Bi}_{0.49}\text{Te}_{0.01}$ without

texture. Due to the better thermoelectric performance in the entire temperature range, the average ZT reaches 1.1 between 300 K and 773 K.

3.2.3.5 Conclusions

Thermoelectric properties of $\text{Mg}_{3.1}\text{Nb}_{0.1}\text{Sb}_{1.5}\text{Bi}_{0.49}\text{Te}_{0.01}$ were compared between the textured and as-pressed samples in the planes perpendicular and parallel to the press directions. Textured structure was obtained after repeated hot forging was applied, which was confirmed by the XRD, rocking curve, and SEM observations. The preferentially oriented grains are favorable to achieve higher mobility, $105 \text{ cm}^2 \text{ V}^{-1} \text{ s}^{-1}$ at room temperature, leading to higher electrical conductivity and thermoelectric properties in the plane perpendicular to the hot press direction at room temperature. The power factor reached $18 \mu\text{W cm}^{-1} \text{ K}^{-2}$ at room temperature, and the ZT reached 0.5 at room temperature and 1.5 at 773 K, leading to an average ZT of 1.1 between 300 K and 773 K. Although the peak ZT was not improved dramatically due to the partial texture, the average ZT was much higher, indicating that further studies on growing single crystals should be pursued.

3.3 Achieving high thermoelectric performance of n-type $\text{Mg}_3\text{Sb}_{1.5}\text{Bi}_{0.5}$ -based compounds by effective donor

3.3.1 Introduction

N-type Mg_3Sb_2 -based Zintl compounds have attracted considerable interest in recent years for their high thermoelectric performance. Mg_3Sb_2 -based compounds inherently have p-type transport properties due to the presence of intrinsic Mg vacancies.^[129, 130] Therefore, eliminating Mg vacancies and increasing the electron concentration are crucial for achieving high performance n-type Mg_3Sb_2 -based materials. It was demonstrated that excess Mg in the initial composition was considered critical for

suppressing the Mg vacancies and lifting the Fermi level upward to the conduction band.^[131, 132]

According to traditional synthesis method, elemental Mg is easily vaporizing during hot pressing or using the spark plasma sintering (SPS) process due to its high vapor pressure, which always leads to Mg deficiency in the final composition.^[125, 133] Under the Mg-poor situation, Mg vacancies are energetically favorable to form as acceptor defects, which pin the Fermi level in the valence band. To realize the n-type conduction in Mg₃Sb₂-based materials, prevention of Mg vacancies is mandatory, which can be achieved by adding extra Mg, or alternatively by choosing a donor at the Mg site to suppress Mg vacancies.^[130]

Here we experimentally demonstrate that subgroup III and lanthanide elements act as strong donors in Mg₃Sb_{1.5}Bi_{0.5} solid solutions. In order to gain further insights, Y was selected for study to elucidate the details. It turns out that Y preferentially goes to the Mg site and prevents formation of Mg vacancies, with the final realization of high-performance n-type Mg_{3+δ}Y_xSb_{1.5}Bi_{0.5} through optimization of the carrier concentration. Neutron diffraction refinements provide strong evidence that Y favorably goes to the Mg (II) site, where most of the Mg vacancies are located. It is clearly shown that Y is a very effective electron donor leading to better n-type thermoelectric properties as compared with those resulting from excess Mg or chalcogen dopants. By studying the sound velocity, it is found that the thermal conductivity suppression by phonon scattering in n-type Mg₃Sb_{1.5}Bi_{0.5} is limited, and that the higher thermoelectric performance in our materials most likely is due to the optimized carrier concentration. In a nominal composition Mg_{3.0}Y_{0.035}Sb_{1.5}Bi_{0.5}, carrier concentration reached $6.5 \times 10^{19} \text{ cm}^{-3}$, contributing to high electrical conductivity

and power factor, and finally a peak ZT of ~ 1.6 at 773 K. When Mg concentration is further tuned, a carrier concentration of $3.6 \times 10^{19} \text{ cm}^{-3}$ is obtained in $\text{Mg}_{3.02}\text{Y}_{0.02}\text{Sb}_{1.5}\text{Bi}_{0.5}$, leading to a higher Seebeck coefficient. By taking advantage of increased mobility, the power factor is enhanced to $\sim 17.2 \mu\text{W cm}^{-1} \text{ K}^{-2}$ at 773 K, and finally a peak ZT of ~ 1.8 at 773 K is obtained.

3.3.2 Experimental section

3.3.2.1 Synthesis

Magnesium turnings (Alfa Aesar, 99.9%), bismuth chunks (Sigma Aldrich, 99.999%), yttrium chunks (Sigma Aldrich, 99.9%), and antimony chunks (Sigma Aldrich, 99.999%) were weighed according to the designed nominal stoichiometry. All the weighed materials were loaded directly into a stainless-steel jar (Spex 8007B) inside a glove box with oxygen level below 0.1 ppm, and then taken out for ball milling for 10 hours. The powders were then hot pressed into dense pellets at 750 °C for 2 min.

3.3.2.2 Neutron diffraction

Neutron powder diffraction data were collected on HB-2A at the High Flux Isotope Reactor at the Oak Ridge National Laboratory. A GE (115) monochromator ($\lambda = 1.54 \text{ \AA}$) was adopted. The data analysis was carried out by Rietveld refinement implemented in Fullprof Suite toolbar.

3.3.2.3 Sound velocity measurement

Sound velocity measurements were carried out by a RITEC Advanced Ultrasonic Measurement System RAM-5000. The system realizes pulse-echo method of time propagation measurements with an accuracy of about 10^{-3} . To generate longitudinal (L)

and shear (S) ultrasonic bulk waves, Olympus transducers V129-RM (10 MHz) and V157-RM (5 MHz) were used. Propylene glycol and SWC (both from Olympus) were used as couplant materials for L and S modes, respectively.

3.3.3 Results and discussion

3.3.3.1 Realizing n-type conductivity by Y doping in $\text{Mg}_{3-x}\text{Y}_x\text{Sb}_{1.5}\text{Bi}_{0.5}$

To initially determine whether n-type conductivity could be achieved by a simple doping of Y at the Mg site, samples with nominal compositions of $\text{Mg}_{3-x}\text{Y}_x\text{Sb}_{1.5}\text{Bi}_{0.5}$ ($x = 0, 0.05, 0.1, 0.125, 0.15, \text{ and } 0.2$) were synthesized. The X-ray diffraction patterns for $\text{Mg}_{3-x}\text{Y}_x\text{Sb}_{1.5}\text{Bi}_{0.5}$ are shown in Fig. 22. The dominant peaks of the samples are indexed to the trigonal CaAl_2Si_2 crystal structure, and the discernable small peaks labeled are the impurity phase YSb when x is larger than 0.05, indicating that Y has a limited solubility in the compound. At the same time, it can be observed in Fig. 22 (b) that lattice parameters for both a and c are almost constant when x is larger than 0.05, further supporting the low solubility claim. The variations of XRD spectra and lattice parameters indicate that 0.05 is

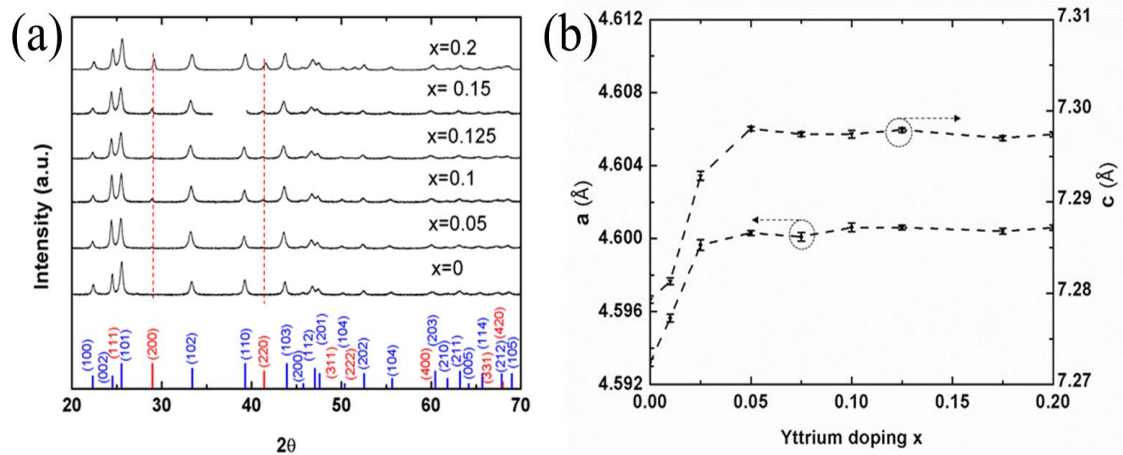


Figure 22 (a) X-ray diffraction patterns of hot-pressed $\text{Mg}_{3.0-x}\text{Y}_x\text{Sb}_{1.5}\text{Bi}_{0.5}$ compounds with the standard Mg_3Sb_2 (PDF# 03-0375, solid blue) and YSb (PDF#15-0847, solid red). (b) Lattice parameters as a function of Y.

close to the solubility of Y in $\text{Mg}_{3-x}\text{Y}_x\text{Sb}_{1.5}\text{Bi}_{0.5}$ solid solution. The actual solubility of Y in $\text{Mg}_3\text{Sb}_{1.5}\text{Bi}_{0.5}$ solid solution is possibly overestimated due to undetectable information from

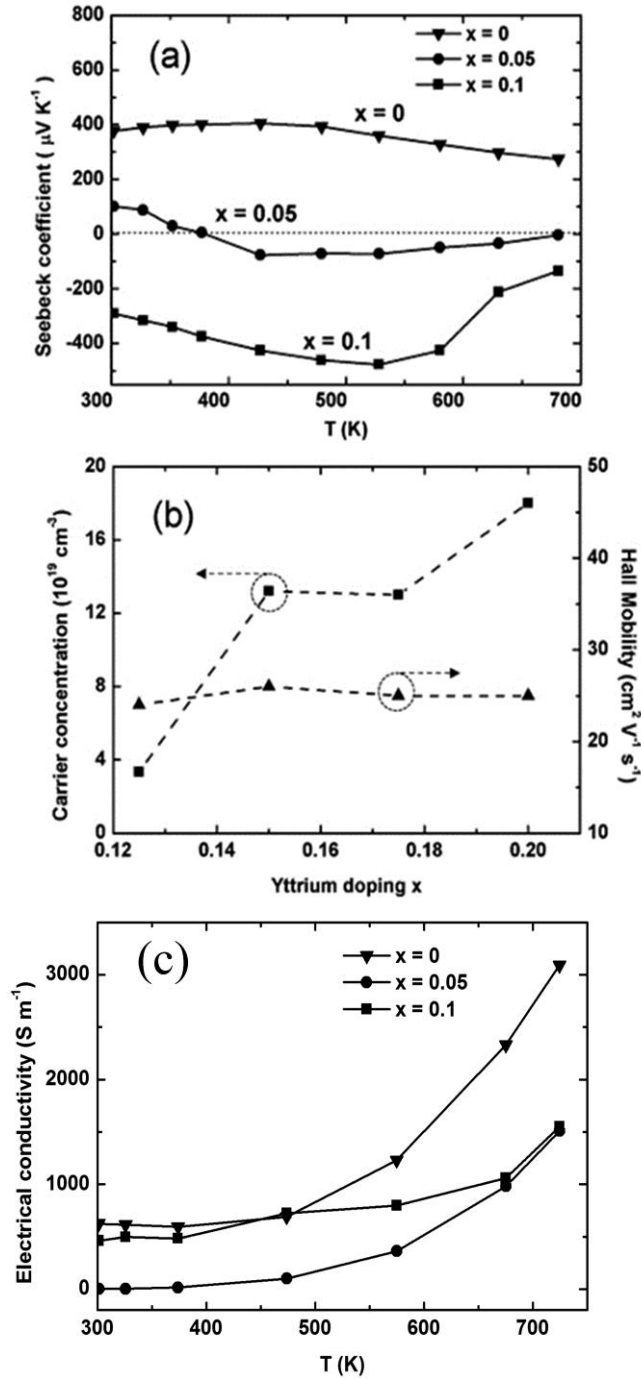


Figure 23 (a) Temperature dependence of the Seebeck coefficient of $\text{Mg}_{3-x}\text{Y}_x\text{Sb}_{1.5}\text{Bi}_{0.5}$ ($x = 0, 0.05, 0.1$). (b) Room temperature carrier concentration and Hall mobility, (c) Temperature dependence of the electrical conductivity.

nano-scale inclusions.

Y is a subgroup III element on the periodic table, and has one more valence electron than Mg. When entering into Mg sites in the lattice, Y is supposed to donate electrons. Fig. 23(a) shows the temperature dependence of the Seebeck coefficient of $\text{Mg}_{3-x}\text{Y}_x\text{Sb}_{1.5}\text{Bi}_{0.5}$ ($x = 0, 0.05, 0.1$). $\text{Mg}_{2.95}\text{Y}_{0.05}\text{Sb}_{1.5}\text{Bi}_{0.5}$ exhibits basically intrinsic transport properties during p/n conduction transition since its positive Seebeck coefficient at room temperature

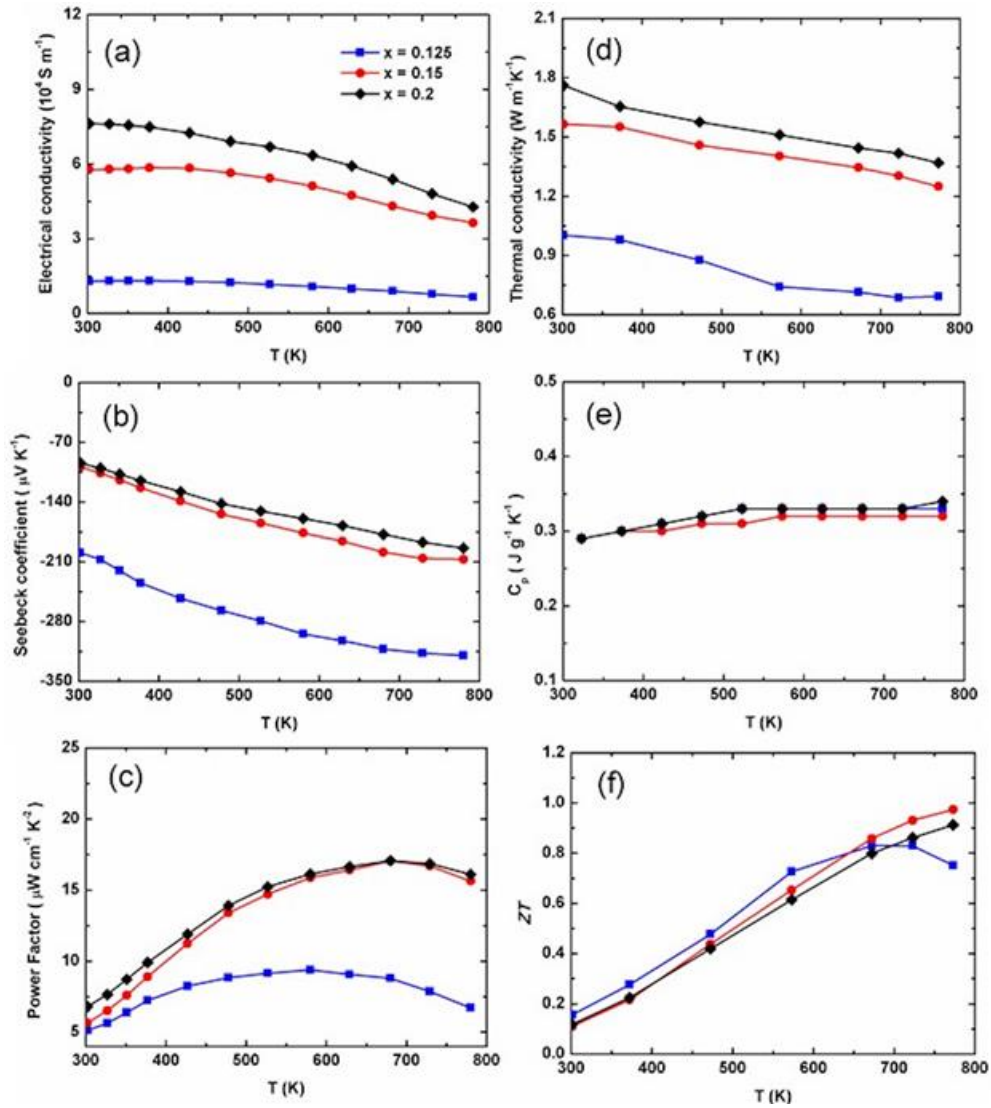


Figure 24 Temperature dependence of (a) electrical conductivity, (b) Seebeck coefficient, (c) power factor, (d) thermal conductivity, (e) specific heat capacity, and (f) ZT for $\text{Mg}_{3-x}\text{Y}_x\text{Sb}_{1.5}\text{Bi}_{0.5}$ ($x = 0.125, 0.15, \text{ and } 0.2$).

reverses sign above 350 K. And a very low electrical conductivity of $\sim 625 \text{ S m}^{-1}$ at room temperature indicates that holes participated in transportation were neutralized by electrons. However, the Seebeck coefficient of $\text{Mg}_{2.9}\text{Y}_{0.1}\text{Sb}_{1.5}\text{Bi}_{0.5}$ in Fig 23 (a) is negative over the entire temperature range and displays high electrical conductivity, exhibiting the characteristics of n-type conduction. The p/n conduction transition between $\text{Mg}_{2.95}\text{Y}_{0.05}\text{Sb}_{1.5}\text{Bi}_{0.5}$ and $\text{Mg}_{2.9}\text{Y}_{0.1}\text{Sb}_{1.5}\text{Bi}_{0.5}$ suggests that significant role that Y plays in $\text{Mg}_{3-x}\text{Y}_x\text{Sb}_{1.5}\text{Bi}_{0.5}$ compounds. The carrier concentration and mobility dependence on Y concentration for $x \geq 0.1$ are presented in Fig. 23(b) (the data for $x < 0.1$ are not shown here because samples with $x < 0.1$ exhibit extremely low carrier concentration, causing large measurement error). It should be noted that the carrier concentration sharply increases to 10^{20} cm^{-3} for $x = 0.15$, while the Hall mobility is almost constant for Y between 0.125 and 0.2. The increased carrier concentration and almost constant mobility are typical characteristics of modulation doping from YSb. As mentioned previously, suppressing Mg

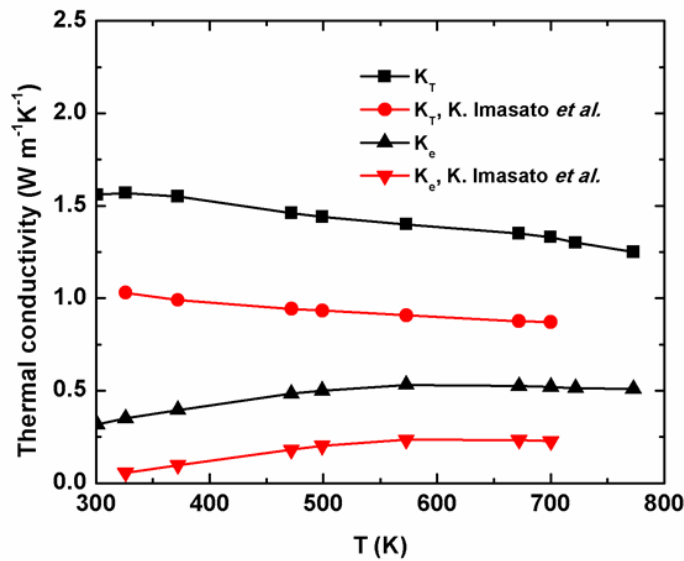


Figure 25 Temperature dependence of electronic thermal conductivity of $\text{Mg}_{2.85}\text{Y}_{0.15}\text{Sb}_{1.5}\text{Bi}_{0.5}$ in comparison with that of $\text{Mg}_{3.2}\text{Sb}_{1.5}\text{Bi}_{0.49}\text{Te}_{0.01}$.

vacancies is essential to realize n-type conduction. It can be speculated that Y ($x < 0.05$) preferentially occupies Mg vacancy sites (as will be further discussed below), which is favorable for lifting the Fermi level up to the conduction band, and metallic YSb simply acts as a modulation electron donor to increase carrier concentration at $x > 0.05$, which makes it possible to achieve good n-type conductivity.

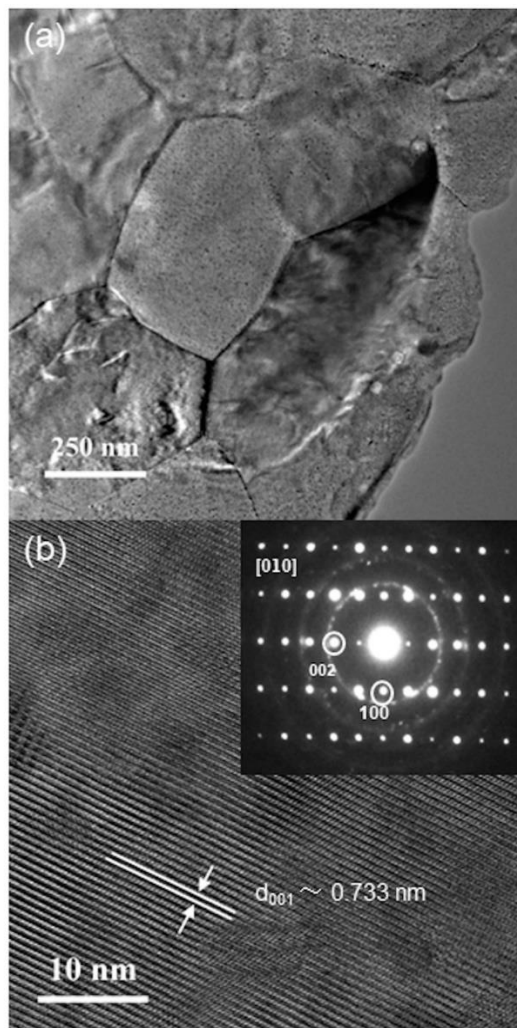


Figure 26 (a) TEM image of microstructure morphology of $\text{Mg}_{2.9}\text{Y}_{0.1}\text{Sb}_{1.5}\text{Bi}_{0.5}$. (b) High-resolution TEM image shows the lattice fringes with 0.733 nm spacing, with SAED pattern (inset) indexed to be trigonal phase along the $[010]$ zone axis.

Thermoelectric performance parameters of $\text{Mg}_{3-x}\text{Y}_x\text{Sb}_{1.5}\text{Bi}_{0.5}$ ($x = 0.125, 0.15,$ and 0.2) can be found in Fig. 24. Both $\text{Mg}_{2.85}\text{Y}_{0.15}\text{Sb}_{1.5}\text{Bi}_{0.5}$ and $\text{Mg}_{2.8}\text{Y}_{0.2}\text{Sb}_{1.5}\text{Bi}_{0.5}$ show decent power factor over the entire temperature range due to the high electrical conductivity, and the maximum power factor reaches $\sim 16.3 \mu\text{W cm}^{-1} \text{K}^{-2}$ at 773 K. However, the thermal

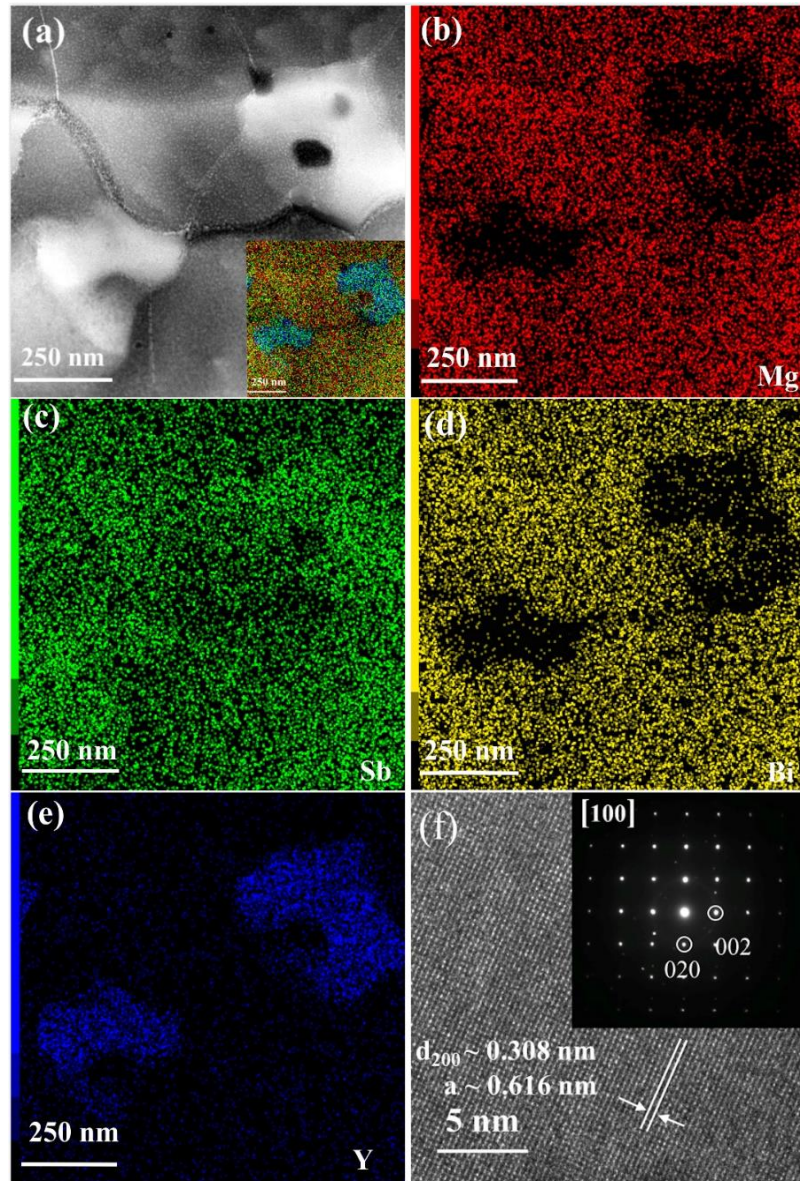


Figure 27 (a) (HAADF)-STEM image of $\text{Mg}_{2.9}\text{Y}_{0.1}\text{Sb}_{1.5}\text{Bi}_{0.5}$ (the inset shows the EDX mapping). (b)-(e) EDX mapping of the bright areas. (f) High-resolution TEM image taken from the bright areas with the corresponding SAED pattern (inset).

conductivity of $\text{Mg}_{2.85}\text{Y}_{0.15}\text{Sb}_{1.5}\text{Bi}_{0.5}$ is much higher than that of $\text{Mg}_{3.2}\text{Sb}_{1.5}\text{Bi}_{0.49}\text{Te}_{0.01}$. The electronic contribution to thermal conductivity of $\text{Mg}_{2.85}\text{Y}_{0.15}\text{Sb}_{1.5}\text{Bi}_{0.5}$ is calculated and compared with that of $\text{Mg}_{3.2}\text{Sb}_{1.5}\text{Bi}_{0.49}\text{Te}_{0.01}$ (Fig. 25). Electronic thermal conductivity of $\text{Mg}_{2.85}\text{Y}_{0.15}\text{Sb}_{1.5}\text{Bi}_{0.5}$ is about 100% larger than that of $\text{Mg}_{3.2}\text{Sb}_{1.5}\text{Bi}_{0.49}\text{Te}_{0.01}$, which indicates that the large increase of thermal conductivity is mainly ascribed to the increased electronic contribution that may be affected by the impurity YSb. Finally, a peak ZT of only ~ 1.0 at 773 K was reached by $\text{Mg}_{2.85}\text{Y}_{0.15}\text{Sb}_{1.5}\text{Bi}_{0.5}$ (Fig. 24).

Fig. 26(a) shows the typical microstructure morphology of Mg_3Sb_2 -based Zintl compounds. The distinguishable grain boundaries are clearly observed with grain size of about 500 nm \sim 1 μm . In Fig. 26(b), the high-resolution transmission electron microscopy (TEM) image displays the lattice fringes with lattice spacing of 0.733 nm, which corresponds to the (001) facet of Mg_3Sb_2 , and the corresponding selected area electron diffraction (SAED) is indexed to be trigonal phase along the [010] zone axis (inset). From the low magnification high angle annular dark field (HAADF)-STEM image shown in Fig. 27(a), it can be seen there are some bright areas with diameters of 300 nm distributed in the matrix. Energy-dispersive X-ray spectroscopy (EDX) mapping was conducted to investigate the composition of these bright areas. Fig. 27(a)-(e) clearly show that all of the elements are distributed uniformly throughout the matrix except in the bright areas, which lack Mg and Bi but are rich in Y and Sb, suggesting the existence of the compound YSb. The high-resolution TEM image of the bright area in Fig. 27(f) shows the lattice fringes with lattice spacing of 0.308 nm, which corresponds to the (200) facet of YSb, and the corresponding SAED pattern from the bright area is successfully indexed to be the [100] zone axis of the cubic phase YSb (inset). By the combined analysis of EDX mapping and

SAED pattern, it was concluded that YSb indeed exists as the impurity phase when Y concentration is larger than 0.05. Asahi *et al.* reported that YSb has a very low formation energy and can form very easily in half-Heusler compounds that contains Y and Sb.^[135] Zhu *et al.* also reported that YSb nanodots contribute electrons to electrical and thermal transport in HfNiSn alloys.^[136] In order to understand the roles YSb plays, pure-phase YSb was synthesized by ball milling and hot pressing and was shown to exhibit much higher electrical conductivity, $1.6 \times 10^6 \text{ S m}^{-1}$ at room temperature, verifying our assumption that YSb acts as a modulation dopant.

3.3.3.2 Enhancement of thermoelectric performance by adding extra Y as $\text{Mg}_{3.0}\text{Y}_x\text{Sb}_{1.5}\text{Bi}_{0.5}$

Even though a simple doping of Y leads to n-type conduction in $\text{Mg}_{3-x}\text{Y}_x\text{Sb}_{1.5}\text{Bi}_{0.5}$ solid solution, the ZT is not as high as those of $\text{Mg}_{3.2-x}\text{M}_x\text{Sb}_{1.5}\text{Bi}_{0.49}\text{Te}_{0.01}$ ($M = \text{Co}, \text{Fe}, \text{Hf}, \text{Ta}, \text{etc.}$) reported by Mao *et al.*^[117, 133] Knowing that YSb induces increased thermal

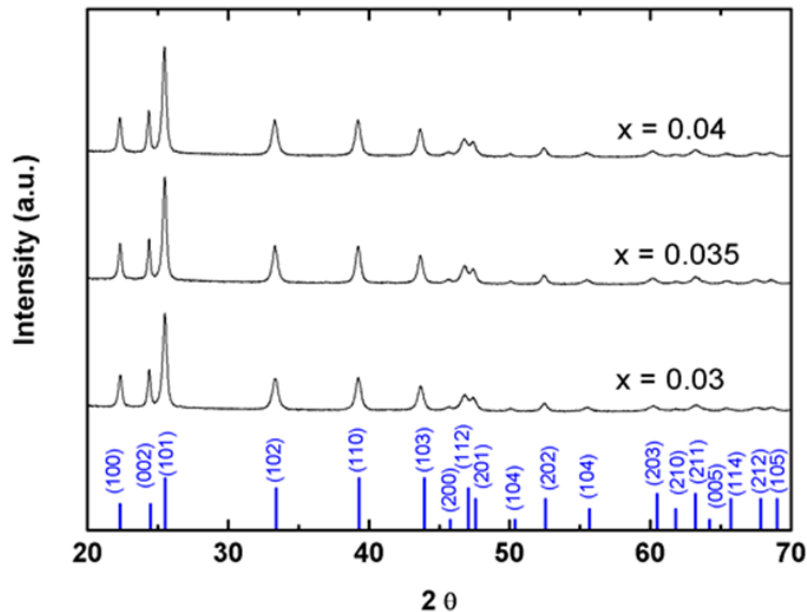


Figure 28 X-ray diffraction patterns of hot-pressed $\text{Mg}_{3.0}\text{Y}_x\text{Sb}_{1.5}\text{Bi}_{0.5}$ ($x = 0.03, 0.035, 0.04$) compounds with standard Mg_3Sb_2 pattern (PDF# 03-0375, solid blue).

conductivity, we also studied the thermoelectric performance effect of Y addition instead of substitution within the Y solubility limit to suppress the thermal conductivity by avoiding the formation of the YSb phase. Bulk pellets of $\text{Mg}_{3.0}\text{Y}_x\text{Sb}_{1.5}\text{Bi}_{0.5}$ ($x = 0.03, 0.035,$ and 0.04) were prepared ($x = 0.02$ is not shown here due to its high electrical resistance and poor performance). The powder X-ray diffraction patterns of the samples are shown in Fig. 28. All of the peaks are well indexed to the trigonal CaAl_2Si_2 crystal structure without discernable impurity phase within the detection limit. The lattice parameters along the a-b plane and c axis increase linearly with the Y concentration, which is expected due to the larger ionic diameter of Y compared to that of Mg (Table 3). It should be noted that the carrier concentration of $\text{Mg}_{3.0}\text{Y}_{0.03}\text{Sb}_{1.5}\text{Bi}_{0.5}$ can reach $3.3 \times 10^{19} \text{ cm}^{-3}$ at room temperature.

Compared with the report by Shuai *et al.*, the nominal composition $\text{Mg}_{3.0}\text{Sb}_{1.5}\text{Bi}_{0.5}$ fabricated by ball milling and hot-pressing leads to the actual composition $\text{Mg}_{2.942}\text{Sb}_{1.5}\text{Bi}_{0.5}$, and finally hole carrier concentration of $7.9 \times 10^{17} \text{ cm}^{-3}$.^[132] The substantial increase of electron concentration most likely is attributed to the strong donor effect of Y in the lattice. Fig. 29 presents the temperature dependence of thermoelectric properties of $\text{Mg}_{3.0}\text{Y}_x\text{Sb}_{1.5}\text{Bi}_{0.5}$ ($x = 0.03, 0.035,$ and 0.04). It is worth noting that higher Y concentration leads to higher carrier concentration, as well as higher electrical conductivity at room temperature [Fig. 29(a)]. The Seebeck coefficients in Fig. 29(b) are negative and the absolute values increase with increasing temperature, features typical of a degenerated semiconductor. $\text{Mg}_{3.0}\text{Y}_{0.035}\text{Sb}_{1.5}\text{Bi}_{0.5}$ and $\text{Mg}_{3.0}\text{Y}_{0.04}\text{Sb}_{1.5}\text{Bi}_{0.5}$ exhibit excellent electrical conductivity and power factor due to higher carrier concentration, which reach $\sim 15.8 \mu\text{W cm}^{-1} \text{ K}^{-2}$ and $\sim 14.9 \mu\text{W cm}^{-1} \text{ K}^{-2}$ at 773 K, respectively. However, low carrier concentration in $\text{Mg}_{3.0}\text{Y}_{0.03}\text{Sb}_{1.5}\text{Bi}_{0.5}$ results in lower electrical conductivity and power factor. Thermal

conductivity of $\text{Mg}_{3.0}\text{Y}_x\text{Sb}_{1.5}\text{Bi}_{0.5}$ compounds is comparable to that of n-type $\text{Mg}_{3.2-x}\text{M}_x\text{Sb}_{1.5}\text{Bi}_{0.5}$ solid solution, which may be partly ascribed to the reduced effect of YSb, while the slightly higher thermal conductivity of $\text{Mg}_{3.0}\text{Y}_{0.04}\text{Sb}_{1.5}\text{Bi}_{0.5}$ over the entire temperature range is probably due to the appearance of the YSb phase. For $\text{Mg}_{3.0}\text{Y}_x\text{Sb}_{1.5}\text{Bi}_{0.5}$ ($x = 0.03, 0.035, \text{ and } 0.04$) without Mg deficiency in the initial composition, the solubility of Y is probably at around 0.04 or even lower. The solubility of Y in $\text{Mg}_{3.0+\delta}\text{Y}_x\text{Sb}_{1.5}\text{Bi}_{0.5}$ compounds might be dependent on whether there is deficiency or extra in Mg in the initial composition. Thermal conductivity of $\text{Mg}_{3.0}\text{Y}_{0.035}\text{Sb}_{1.5}\text{Bi}_{0.5}$

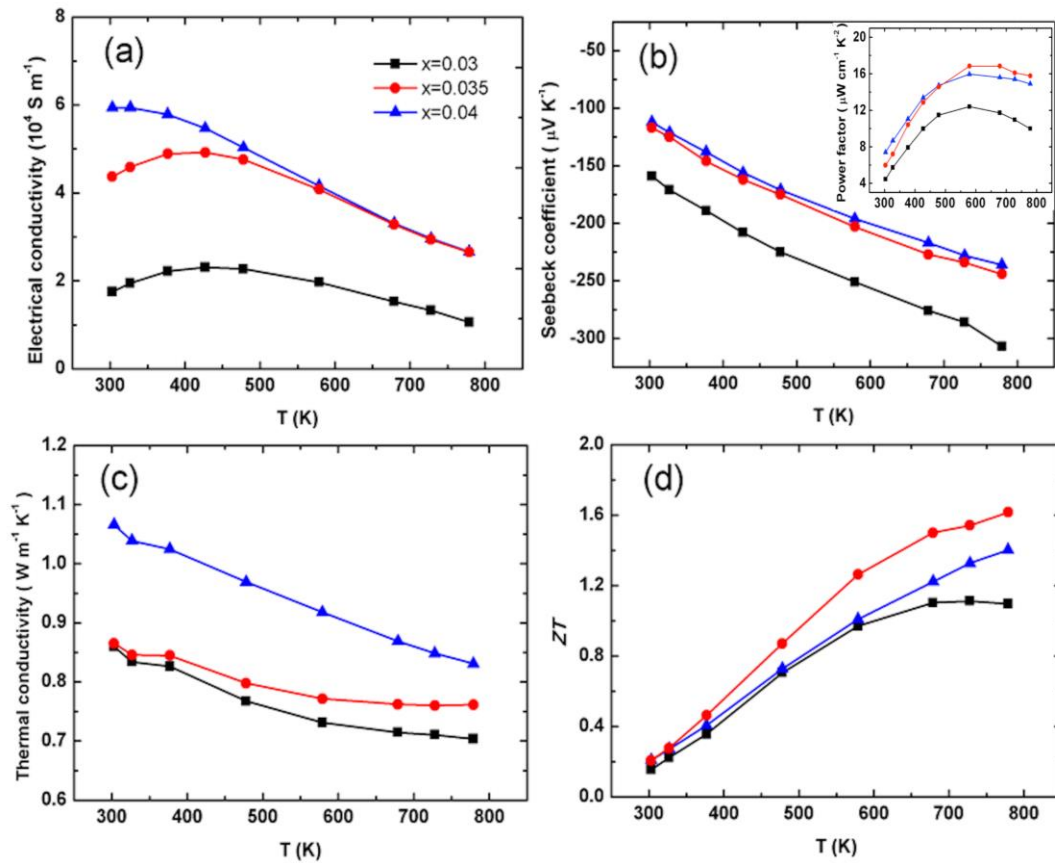


Figure 29 Temperature dependence of (a) electrical conductivity, (b) Seebeck coefficient (inset is temperature dependence of power factor), (c) thermal conductivity, and (d) ZT of $\text{Mg}_{3.0}\text{Y}_x\text{Sb}_{1.5}\text{Bi}_{0.5}$ ($x = 0.03, 0.035, \text{ and } 0.04$).

reached $\sim 0.76 \text{ W m}^{-1} \text{ K}^{-1}$ at 773 K, resulting in a peak ZT of ~ 1.6 , which is comparable with the best ever reported peak ZT in any n-type Zintl compounds.

Table 3. Carrier concentration, Hall mobility, lattice parameters, and density of $\text{Mg}_{3.0}\text{Y}_x\text{Sb}_{1.5}\text{Bi}_{0.5}$ ($x = 0.03, 0.035, 0.04$) compounds.

$\text{Mg}_{3.0}\text{Y}_x\text{Sb}_{1.5}\text{Bi}_{0.5}$	Carrier concentration (10^{19} cm^{-3})	Hall mobility ($\text{cm}^2 \text{ V}^{-1} \text{ s}^{-1}$)	a (nm)	c (nm)	Density (g cm^{-3})	Theoretical value	Relative density
$x = 0.03$	3.33	32.8	0.45818	0.72705	4.47	4.558	98.20%
$x = 0.035$	6.35	41.8	0.45821	0.72790	4.49	4.558	98.60%
$x = 0.04$	9.26	40.4	0.45825	0.72820	4.50	4.560	98.68%

3.4.3 Joint effect of Y and Mg in $\text{Mg}_{3.0+\delta}\text{Y}_{0.02}\text{Sb}_{1.5}\text{Bi}_{0.5}$

With the addition of Y in $\text{Mg}_{3.0}\text{Y}_{0.035}\text{Sb}_{1.5}\text{Bi}_{0.5}$, the peak ZT reaches ~ 1.6 , much higher than that of the Y-doped composition $\text{Mg}_{2.85}\text{Y}_{0.125}\text{Sb}_{1.5}\text{Bi}_{0.5}$. We thus explored whether a slight addition of Mg would further increase the peak ZT in the Y-added compositions $\text{Mg}_{3.0+\delta}\text{Y}_x\text{Sb}_{1.5}\text{Bi}_{0.5}$. Through an extensive optimization of Y concentration, we focused on studying $\text{Mg}_{3.0+\delta}\text{Y}_{0.02}\text{Sb}_{1.5}\text{Bi}_{0.5}$ by keeping Y at 0.02 to avoid any possibility of YSb formation. Samples of $\text{Mg}_{3.0+x}\text{Y}_{0.02}\text{Sb}_{1.5}\text{Bi}_{0.5}$ with $x = 0.015, 0.02, \text{ and } 0.04$ were prepared according to previously described methods and showed at least 98% relative density (Table 4). Temperature dependence of thermoelectric performances of $\text{Mg}_{3.0+x}\text{Y}_{0.02}\text{Sb}_{1.5}\text{Bi}_{0.5}$ ($x = 0.015, 0.02, 0.04$) are displayed in Fig. 30. The optimized carrier concentrations for the best thermoelectric properties in $\text{Mg}_{3.0}\text{Y}_{0.035}\text{Sb}_{1.5}\text{Bi}_{0.5}$ and $\text{Mg}_{3.02}\text{Y}_{0.02}\text{Sb}_{1.5}\text{Bi}_{0.5}$ compounds are different comparatively, and they are $6.35 \times 10^{19} \text{ cm}^{-3}$ and $3.58 \times 10^{19} \text{ cm}^{-3}$, respectively. The lower carrier concentration in $\text{Mg}_{3.02}\text{Y}_{0.02}\text{Sb}_{1.5}\text{Bi}_{0.5}$ is favorable for higher Seebeck coefficient, $\sim 272 \mu\text{V K}^{-1}$ at 773 K. In addition, another

consequence of lower concentration is higher mobility. Hall mobility of $\text{Mg}_{3.02}\text{Y}_{0.02}\text{Sb}_{1.5}\text{Bi}_{0.5}$ is $\sim 85.4 \text{ cm}^2 \text{ V}^{-1} \text{ s}^{-1}$ at room temperature, which is twice that of $\text{Mg}_{3.0}\text{Y}_x\text{Sb}_{1.5}\text{Bi}_{0.5}$ solid solution and leads to good electrical conductivity over the entire

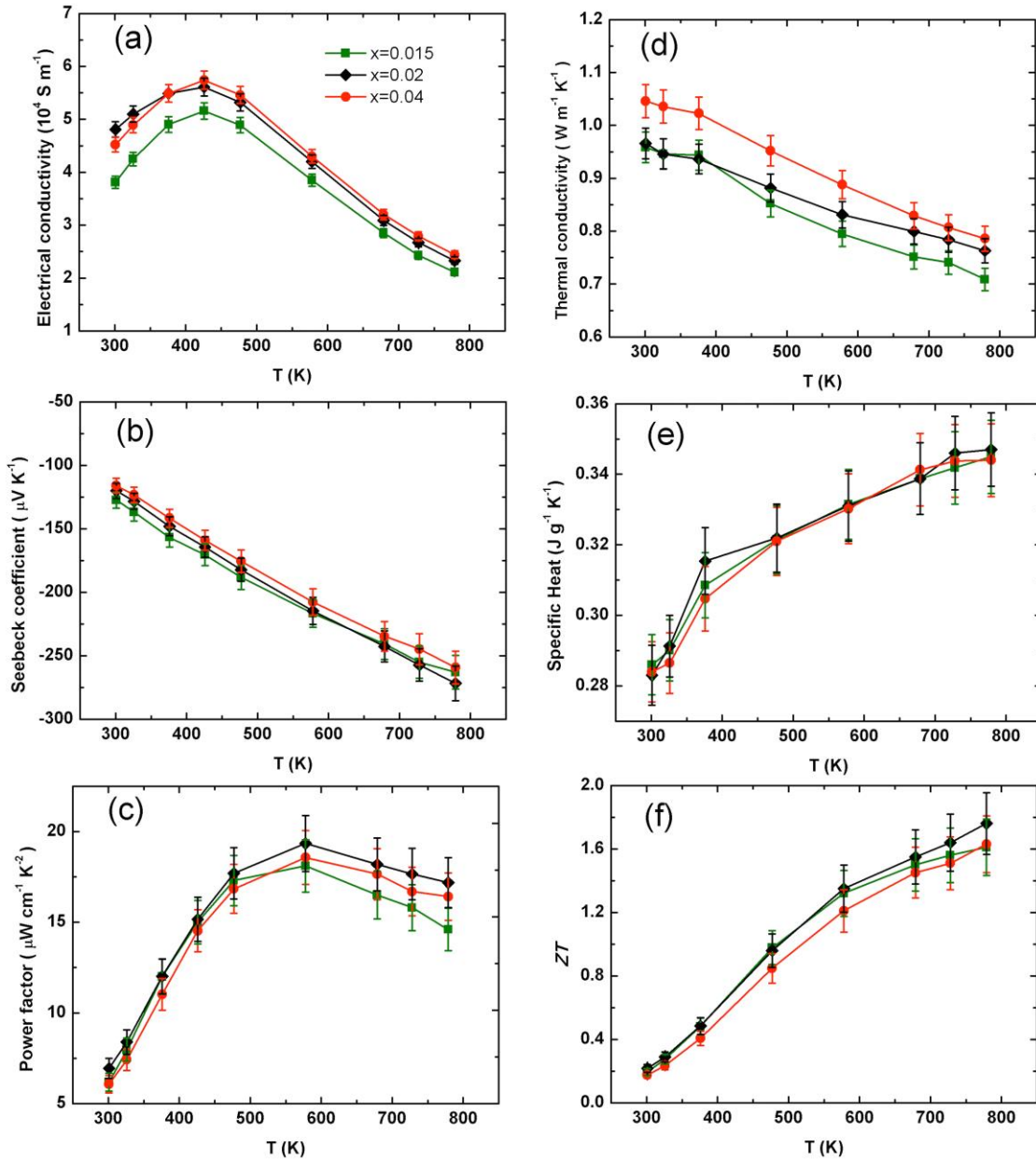


Figure 30 Temperature dependence of (a) electrical conductivity, (b) Seebeck coefficient, (c) power factor, (d) thermal conductivity, (e) specific heat capacity, and (f) ZT of $\text{Mg}_{3+x}\text{Y}_{0.02}\text{Sb}_{1.5}\text{Bi}_{0.5}$ ($x = 0.015, 0.02,$ and 0.04).

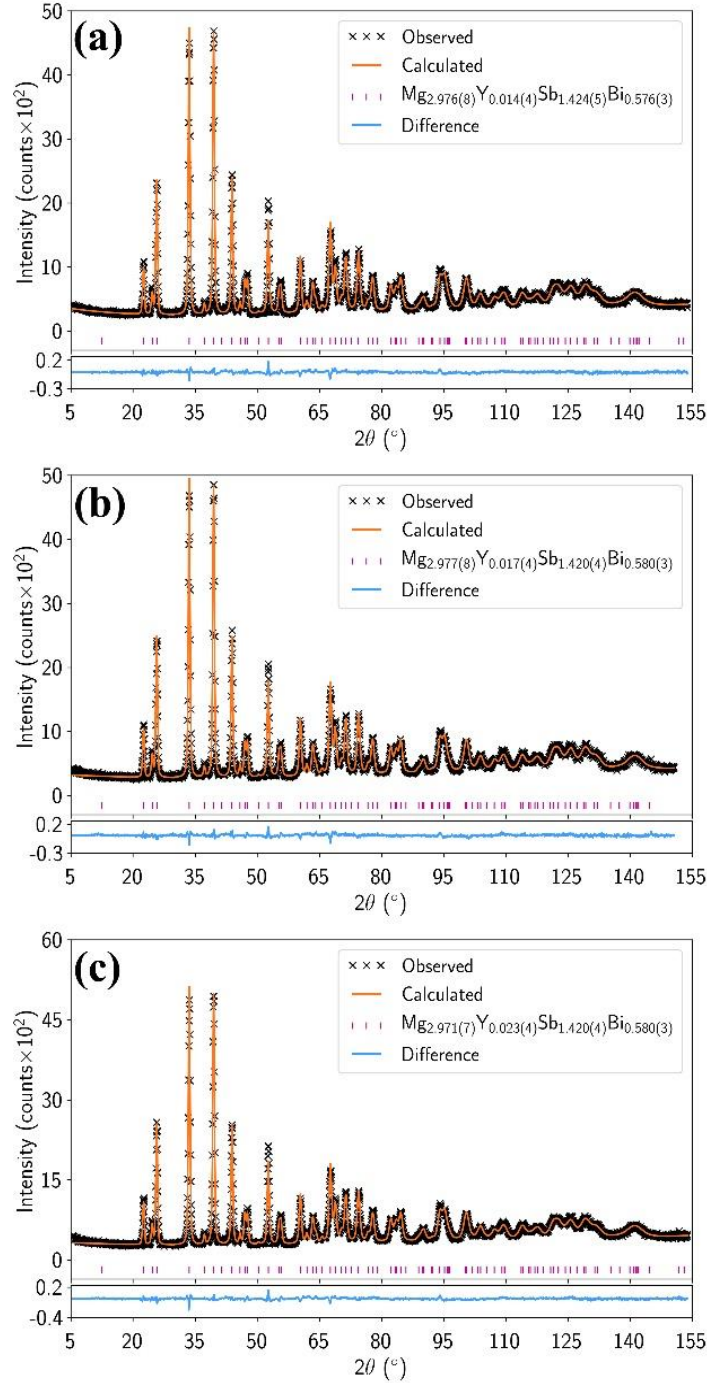


Figure 31 Powder neutron diffraction and Rietveld refinement analysis of $\text{Mg}_{3.0+x}\text{Y}_{0.02}\text{Sb}_{1.5}\text{Bi}_{0.5}$. (a) $\text{Mg}_{3.0}\text{Y}_{0.02}\text{Sb}_{1.5}\text{Bi}_{0.5}$, (b) $\text{Mg}_{3.02}\text{Y}_{0.02}\text{Sb}_{1.5}\text{Bi}_{0.5}$, and (c) $\text{Mg}_{3.04}\text{Y}_{0.02}\text{Sb}_{1.5}\text{Bi}_{0.5}$.

temperature range. Benefiting from the increased Seebeck coefficient and excellent shows

electrical conductivity, $\text{Mg}_{3.02}\text{Y}_{0.02}\text{Sb}_{1.5}\text{Bi}_{0.5}$ the highest peak power factor, $\sim 19.3 \mu\text{W cm}^{-1} \text{K}^{-2}$ at 573 K, which decreases to $\sim 17.2 \mu\text{W cm}^{-1} \text{K}^{-2}$ at 773 K.

To determine where the extra Mg and Y go, powder neutron diffraction was conducted at room temperature (Fig. 31), and the refinement details was similar with the published paper. The refinement results are shown in Table 5. There are five possible defects at these locations: Mg(I), Y(I), Mg(II), Y(II), and Mg(i) (interstitial) are taken into

Table 4 Carrier concentration, Hall mobility, lattice parameters, and density of $\text{Mg}_{3.0+x}\text{Y}_{0.02}\text{Sb}_{1.5}\text{Bi}_{0.5}$ ($x = 0.015, 0.02, 0.04$) compounds.

$\text{Mg}_{3+x}\text{Y}_{0.02}\text{Sb}_{1.5}\text{Bi}_{0.5}$	Carrier concentration (10^{19}cm^{-3})	Hall mobility ($\text{cm}^2 \text{V}^{-1} \text{s}^{-1}$)	a (nm)	c (nm)	Density (g cm^{-3})	Theoretical value	Relative density
$x = 0.015$	2.67	89.1	0.45846	0.72747	4.49	4.552	98.60%
$x = 0.02$	3.58	85.4	0.45849	0.72390	4.50	4.548	98.88%
$x = 0.04$	9.19	30.7	0.45850	0.72520	4.50	4.551	98.88

Table 5. Powder neutron diffraction and Rietveld refinement analysis of $\text{Mg}_{3.0+x}\text{Y}_{0.02}\text{Sb}_{1.5}\text{Bi}_{0.5}$.

Composition	Mg I (1a)	Y I (1a)	Mg II (2d)	Mg II (%)	Sb I (2d)	Bi I (2d)
$\text{Mg}_{3.0}\text{Y}_{0.02}\text{Sb}_{1.5}\text{Bi}_{0.5}$	0.9941	0	1.9822	99.82%	1.4240	0.5760
$\text{Mg}_{3.02}\text{Y}_{0.02}\text{Sb}_{1.5}\text{Bi}_{0.5}$	0.9944	0	1.9898	100.67%	1.4204	0.5796
$\text{Mg}_{3.04}\text{Y}_{0.02}\text{Sb}_{1.5}\text{Bi}_{0.5}$	0.9941	0	2.0013	100.93%	1.4201	0.5799

account in the analysis. It turns out that there are no Mg(i) defects in the matrix, which agrees well with the previous report. In addition, the refinement shows that all of the Y preferentially goes to the Mg(II) sites, which are located in the covalently bonded $[\text{Mg}_2\text{Sb}_2]^{2-}$ layer. Most importantly, there are almost no vacancies left in the lattice. All the Mg vacancies are fully filled with Mg and Y after compensating for the Mg loss during the fabrication process. Compared with Mg, chalcogen and Mg-chalcogen dual doping, Y contributed more carrier concentration with the same doping content. Although attempts were made to put more Mg into the $\text{Mg}_{3.0+x}\text{Y}_{0.02}\text{Sb}_{1.5}\text{Bi}_{0.5}$ solid solutions, the higher electrical transport properties cannot compensate for the large increase of thermal conductivity, resulting in lower ZT .

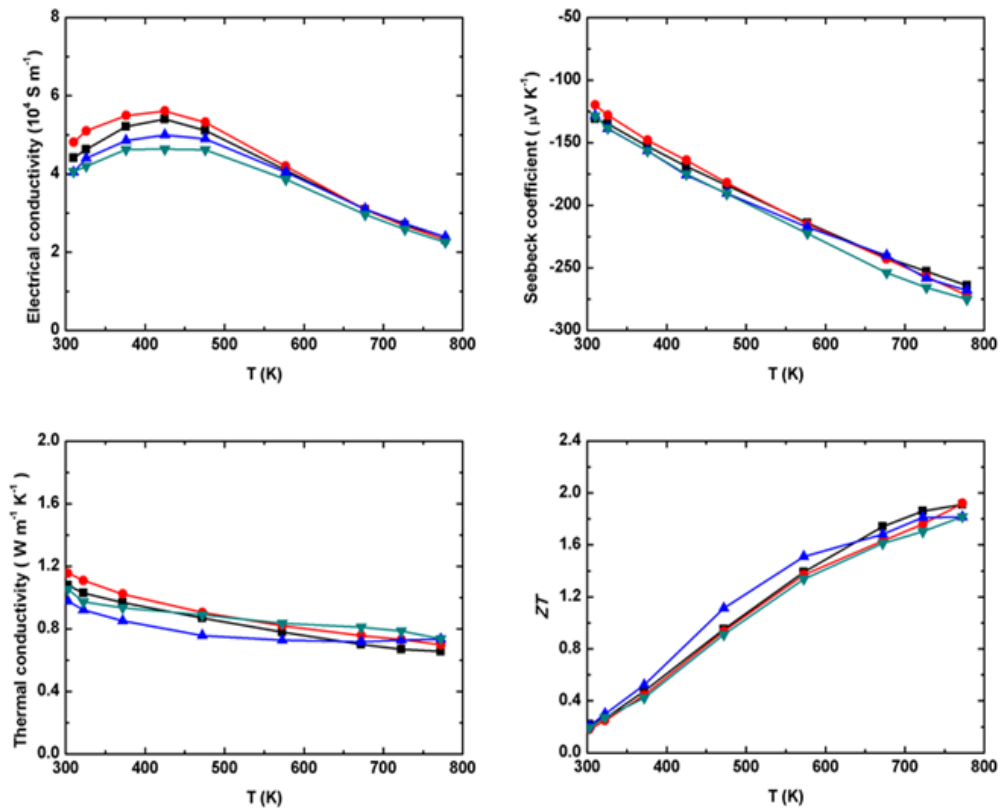


Figure 32 Highly reproducible thermoelectric performances of $\text{Mg}_{3.02}\text{Y}_{0.02}\text{Sb}_{1.5}\text{Bi}_{0.5}$ (Each color stands for each independent experiment).

Table 6 The longitudinal and transverse sound velocities at 300 K, and the glassy limit of the lattice thermal conductivity.

Composition	V_l (m/s)	V_s (m/s)	K_{min} [W/ (m K)]
$Mg_{3.02}Y_{0.02}Sb_{1.5}Bi_{0.5}$	3748.068	1824.68	0.465
$Mg_{3.04}Y_{0.02}Sb_{1.5}Bi_{0.5}$	3777.881	1838.33	0.469

To further study the thermal conductivity, the longitudinal and transverse sound velocities at room temperature were obtained (Table 6). Based on the measured data, the glassy limit of lattice thermal conductivity was calculated by the equation,

$$\kappa_{min} = \frac{1}{2} \left(\frac{\pi}{6} \right)^{\frac{1}{3}} \kappa_B V^{-\frac{2}{3}}, \quad (3.1)$$

where κ_B is the Boltzmann constant, V is the average volume per atom, \mathbf{v}_s and \mathbf{v}_l are the transverse and longitudinal sound velocities, respectively. Although the longitudinal and transverse sound velocities of $Mg_{3.02}Y_{0.02}Sb_{1.5}Bi_{0.5}$ are slightly smaller than those of $Mg_{3.04}Y_{0.02}Sb_{1.5}Bi_{0.5}$, the limited minimums of lattice thermal conductivity ($2\mathbf{v}_s + \mathbf{v}_l$), conductivity were almost identical, $\sim 0.46 \text{ W m}^{-1} \text{ K}^{-1}$. If the scattering mechanism and band structure are assumed to be the same for both samples, the phonon transport in these two samples should be the same, which leads to the conclusion that thermal transport is subject to limited influences from phonon scattering. The total thermal conductivity is mainly subject to the influence of carrier concentration changes. With optimized carrier concentration, $Mg_{3.0+x}Y_{0.02}Sb_{1.5}Bi_{0.5}$ ($x = 0.015, 0.02, 0.04$) exhibit thermal conductivity of ~ 0.71 , ~ 0.74 , and $\sim 0.79 \text{ W m}^{-1} \text{ K}^{-1}$, respectively [Fig. 30(d)]. Benefitting from the improved power factor, $Mg_{3.02}Y_{0.02}Sb_{1.5}Bi_{0.5}$ shows the highest peak ZT of ~ 1.8 at 773 K.

In order to confirm this result, experiments were repeated a few times independently in Fig. 32, and the results were highly reproducible over the entire temperature range.

3.3.4 Conclusions

N-type Mg_3Sb_2 -based Zintl compounds were successfully achieved by a simple Y doping instead of excess Mg and chalcogens. It is well demonstrated by neutron diffraction that Y preferentially goes to the Mg (II) site and almost eliminates the Mg vacancies in the lattice. Therefore, Y serves as a strong electron donor to yield the n-type conductivity in Mg_3Sb_2 -based compounds and supplies a high concentration of electrons to the materials. Further investigation found that subgroup III and lanthanide elements exhibit the same effect on Mg_3Sb_2 -based compounds. Once Mg vacancies were eliminated, the carrier concentration was easily optimized for high thermoelectric performance. By manipulating carrier concentration and suppressing the influences of the YSb impurity, a peak ZT of ~ 1.8 at 773 K was achieved in $\text{Mg}_{3.02}\text{Y}_{0.02}\text{Sb}_{1.5}\text{Bi}_{0.5}$. This work suggests a new way of preparing n-type Mg_3Sb_2 -based Zintl compounds with high thermoelectric performances. It was clearly demonstrated that a large amount of extra Mg is not needed to achieve high ZT as long as Mg vacancies are suppressed, and carrier concentration is properly optimized.

Chapter 4 A new way to synthesize robust and porous Ni_{1-x}Fe_x layer double hydroxide for efficient electrocatalytic oxygen evolution

4.1 Introduction

Worldwide consumption of fossil fuels continues to escalate due to societal needs, leading to growing environmental concerns, including global warming and extreme weather. Efforts have been made around the world to develop new eco-friendly and renewable energy sources as possible substitutes for fossil fuel.^[17] Hydrogen generated by electrochemical water splitting is considered to be one of the most promising energy alternatives due to its highest energy content by mass and its eco-friendly emissions.^[137] Water splitting is composed of two half reactions, hydrogen evolution reaction (HER) and oxygen evolution reaction (OER). Noble metals (Pt, Ir, and Ru) and their oxides (IrO₂ and RuO₂) have traditionally been acknowledged as the most efficient catalysts for HER and OER, respectively, but their high cost and scarcity severely hinder widespread applications.^[12] Developing non-precious and earth-abundant electrocatalysts is essential to promote the scale-up of water splitting. Compared with HER, OER suffers from multiple steps of proton-coupled electron transfer and displays a sluggish kinetic process, which is the main bottleneck for overall water splitting. Therefore, it is challenging and desirable to develop efficient OER catalysts in order to match well with HER for overall water splitting.^[138]

Normally, efficient catalysts require intrinsically low overpotentials for the reaction, which suggests suitable free energy of adsorption and desorption, low charge-transfer resistance for charge transport and exchange, and a large exposed surface area with active sites.^[109] Rather than developing new kinds of highly efficient catalysts, tremendous efforts

have been devoted to integrating different kinds of three-dimensional (3D) structures with advantageous surface morphologies, such as nanowires,^[130] nanoribbons,^[139] core-shells,^[102] double layers,^[20] sandwich structures,^[98] *etc.* 3D structures could guarantee enough space and channels for bubbles to be dislodged and to fleet out, which would help the catalysts to work longer under larger current density.^[140] Normally, most of these nanoscale catalysts are synthesized by hydrothermal or chemical vapor deposition methods, and then bound on substrates, such as metal foam, metal mat, or fiber paper, which possibly causes charge transfer resistance at the interfaces and the catalysts peeling off under large current density.^[16] To avoid these disadvantages, developing new methods to synthesize *in situ*-derived 3D catalysts would be more reliable for future applications. Ball milling and hot pressing have been regarded as an efficient approach for synthesizing nanosized alloys materials, which makes them highly stable and robust.^[36, 141] Additionally, Ni/Fe hydroxide has been proved to be one of the most efficient OER catalysts in alkaline electrolyte, with some of their catalytic activities outperforming the noble-metal catalysts of IrO₂ and RuO₂.^[142] Basically, Ni/Fe hydroxides can be obtained directly by synthesizing pure alloy NiFe, followed by *in-situ* water oxidation. It has also been reported that metal sulfides, selenides, tellurides, and phosphides are favorable to be converted to metal oxides and hydroxides during *in-situ* oxidation.^[143, 144] It is also well known that Se evaporates at high temperature due to the high vapor pressure.^[118] All these points inspired us to make Ni/Fe hydroxides from NiFe selenides for OER. The original bulk NiFe selenides were fabricated by ball milling, cold pressing, and sintering, abbreviated as “pressing and sintering”. The geometrical density decreased by 18%~22% after sintering in an evacuated quartz tube, giving rise to the porous structure, which is mainly due to the evaporation of Se. Meanwhile,

a thin layer of NiFe layer double hydroxide (LDH) was successfully introduced to the surface of the NiFe selenide through *in-situ* electrochemical oxidation in alkaline solution. In addition, we further improve the OER performance of the NiFe-LDH by vanadium doping, which achieves 100 mA cm⁻², 500 mA cm⁻², and 1000 mA cm⁻² at overpotentials of 244 mV, 278 mV, and 300 mV, respectively, and accompanied by a low Tafel slope of 58 mV dec⁻¹. The doped vanadium not only facilitates the kinetic reaction, but also promotes the charge transfer at the interface of the electrolyte and the electrode. This work provides a new way to synthesize robust and highly efficient bulk catalysts toward large-scale water splitting to generate H₂ and O₂.

4.2 Experiments

4.2.1 Synthesis

Samples were prepared by a solid-state reaction technique. Nickel powders (99.99%, Alfa Aesar), iron powder (99.99%, Alfa Aesar), vanadium powder (99.99%, Alfa Aesar) and selenium shots (99.9%, Sigma Aldrich) were all used as received. All of the raw materials were weighed according to the required stoichiometric ratio in a glovebox with an argon atmosphere (H₂O < 0.1 ppm and O₂ < 0.1 ppm) and put into a stainless-steel jar (SPEX samplePrep 8007). After high-energy ball milling for 2 hours, the obtained fine powder was loaded into a die with a diameter of 12.7 mm in a glovebox and pressed into a pellet under 1 ton. The dense pellet was then sealed in a quartz tube under a vacuum of 7.3×10^{-5} Torr and sintered at 700 °C in a box furnace for 8 hours. A diamond saw was used to cut the as-prepared bulk into bars of 2 mm × 2 mm × 12 mm for electrochemical tests.

4.2.2 Electrochemical characterization

The electrochemical tests were performed *via* a typical three-electrode configuration in 100 mL 1 M KOH electrolyte. Pt and Hg/HgO were adopted as the counter and reference electrodes, respectively. The polarization curves for OER were recorded by linear sweep voltammetry with a scan rate of 2.0 mV s^{-1} in the range of 1.125 ~ 1.625 V vs. RHE (Reversible Hydrogen Electrode) and a scan rate of 50 mV s^{-1} was used to activate the catalyst before taking the polarization curves. *In-situ* oxidation process was also conducted in this range at a scan rate of 50 mV s^{-1} to introduce NiFe layer double hydroxide. Additionally, all of the electrocatalytic measurements were performed at room temperature and the current interruption method was used to compensate for iR error. To evaluate the electrochemical test system, commercial Ni foam was adopted as a reference for the polarization curves.

4.2.3 Materials characterization

Raman spectra were collected using a Horiba JY T64000 Raman spectrometer employing a He-Ne laser with an excitation wavelength of 632.8 nm at a low power density of $3 \times 10^3 \text{ W cm}^{-2}$. The total acquisition time was 60 s. X-ray photoelectron spectra were collected using a PHI Quantera XPS scanning microprobe with an Al monochromatic K_{α} source (15 KV, 20 mA). The chamber pressure was well controlled above 5×10^{-8} Torr. Powder X-ray diffraction spectra analysis was conducted using a PANalytical multipurpose diffractometer with an X'celerator detector (PANalytical X'Pert Pro). The powder of $\text{Ni}_{1-x}\text{Fe}_x\text{Se}_{1.15}$ before water electrolysis was obtained by grinding the pellets after high-temperature sintering. The powder of $\text{Ni}_{0.75-y}\text{V}_y\text{Fe}_{0.25}$ -LDH was peeled off from the bulk surface using a blade after oxygen evolution reaction for morphology and composition

characterizations using a scanning electron microscope (FE-SEM, LEO 1525) and a transmission electron microscope (JEOL 2010F).

4.2.4 Density functional perturbation theory (DFPT) lattice dynamics of β -Ni(OH)₂

β -Ni(OH)₂ crystalizes in a trigonal structure, space group $P\bar{3}m1$ (No. 164), with lattice parameters $a = b = 3.127 \text{ \AA}$, $c = 4.606 \text{ \AA}$. The DFPT lattice dynamics calculations of β -Ni(OH)₂ were performed within the generalized-gradient approximation (GGA) with PBE functional using the DFPT code as implemented in the Quantum Espresso (QE) suite. In the calculations, we used the projector-augmented-wave (PAW) approach with pseudopotentials generated for use with QE. The geometry optimization of crystal structure, electronic band structure, and related properties were calculated self-consistently (SCF) with 100 Ry kinetic energy cutoff for the plane wave, 400 Ry charge density cut-off, SCF tolerance better than 10^{-12} , and 5.10^{-7} Ry/au total residual force on atoms over $25 \times 25 \times 16$ Monkhorst–Pack (MP) k-point grid. The lattice constants calculated for the fully relaxed structure of β -Ni(OH)₂ are $a = b = 3.124 \text{ \AA}$, $c = 4.129 \text{ \AA}$. The DFPT calculations relax the size and shape of crystallographic unit cell through minimization of all quantum mechanical forces in a static lattice, that is, at $T = 0 \text{ K}$. The calculated frequency of Raman active modes are 294 cm^{-1} (E_g), 474 cm^{-1} (A_{1g}), 864 cm^{-1} (E_g), and 3488 cm^{-1} (A_{1g}), respectively. The calculated longitudinal acoustic mode at the M-point of Brillouin zone, LA(M), frequency is 262 cm^{-1} . The harmonics 2LA(M) and 4LA(M) are Raman active.

4.3 Results and discussion

4.3.1 Effects of Ni/Fe ratio on the performance of oxygen evolution reaction

The initial compositions $\text{Ni}_{1-x}\text{Fe}_x\text{Se}_{1.15}$ ($x = 0.2, 0.25, \text{ and } 0.3$) catalysts were synthesized by pressing and sintering. The extra Se in the composition was optimized to compensate for the Se loss during the ball milling and sintering process. Powder X-ray diffraction patterns of $\text{Ni}_{1-x}\text{Fe}_x\text{Se}_{1.15}$ ($x = 0.2, 0.25, \text{ and } 0.3$) in Fig. 33 show that the dominant peaks of the phase are indexed to NiSe and the Ni-deficiency phase $\text{Ni}_{0.85}\text{Se}$. No impurity phase was observed. It should be noted that NiSe and FeSe exhibit the same hexagonal structure and space group (P63/MMC [194]). Fig. 33 further shows the

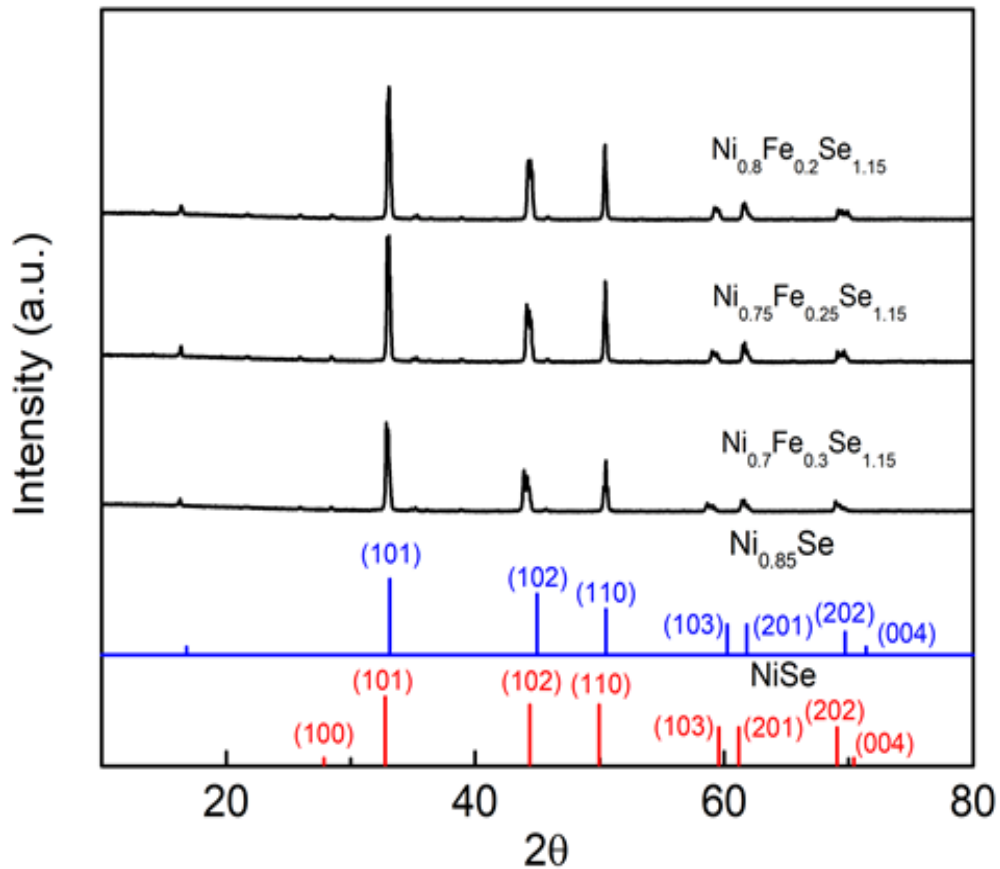


Figure 33 X-ray diffraction patterns of sintered $\text{Ni}_{1-x}\text{Fe}_x\text{Se}_{1.15}$ ($x = 0.2, 0.25, \text{ and } 0.3$) compounds in comparison with those of standard $\text{Ni}_{0.85}\text{Se}$ (solid blue, PDF # 18-0888) and NiSe (solid red, PDF # 020892).



Figure 34 Photograph of $\text{Ni}_{0.75}\text{Fe}_{0.25}\text{Se}_{1.15}$ after oxygen evolution reaction.

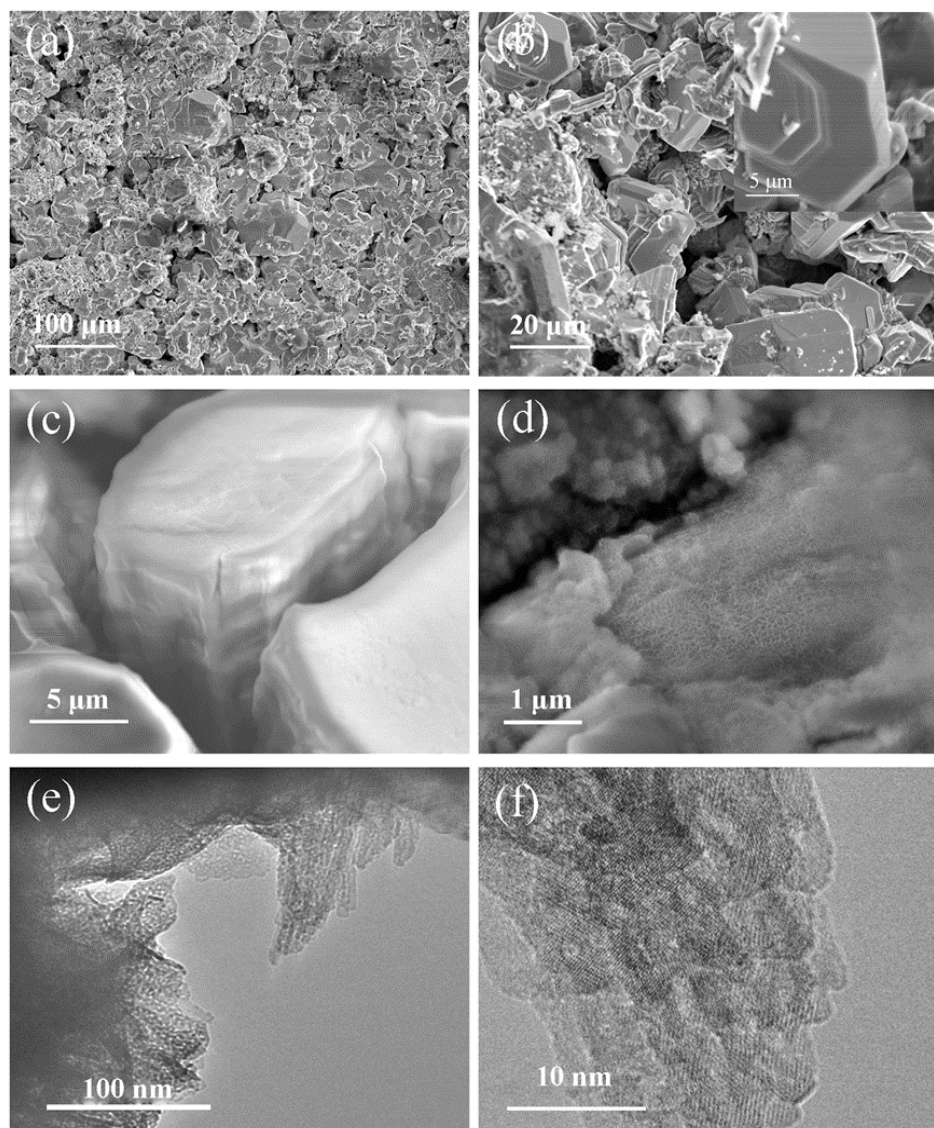


Figure 35 (a) and (b) SEM images of the as-prepared $\text{Ni}_{0.75}\text{Fe}_{0.25}\text{Se}_{1.15}$. (c) and (d) SEM images of $\text{Ni}_{0.75}\text{Fe}_{0.25}\text{Se}_{1.15}$ after oxidation in electrolyte. (e) and (f) TEM images of $\text{Ni}_{0.75}\text{Fe}_{0.25}\text{Se}_{1.15}$ after oxidation in electrolyte.

noticeable positive shift of the main peaks with increased Ni content, which is due to the

smaller lattice constant of NiSe along the c axis ($a = 0.3660$ nm, $c = 0.5330$ nm) and that of $\text{Ni}_{0.85}\text{Se}$ ($a = 0.3624$ nm, $c = 0.5288$ nm) in comparison with that of NiFe ($a = 0.3626$ nm, $c = 0.5940$ nm). The surface morphology of the as-prepared sample was characterized by scanning electron microscopy (SEM). Fig. 34(a) and (b) illustrate that the surface is

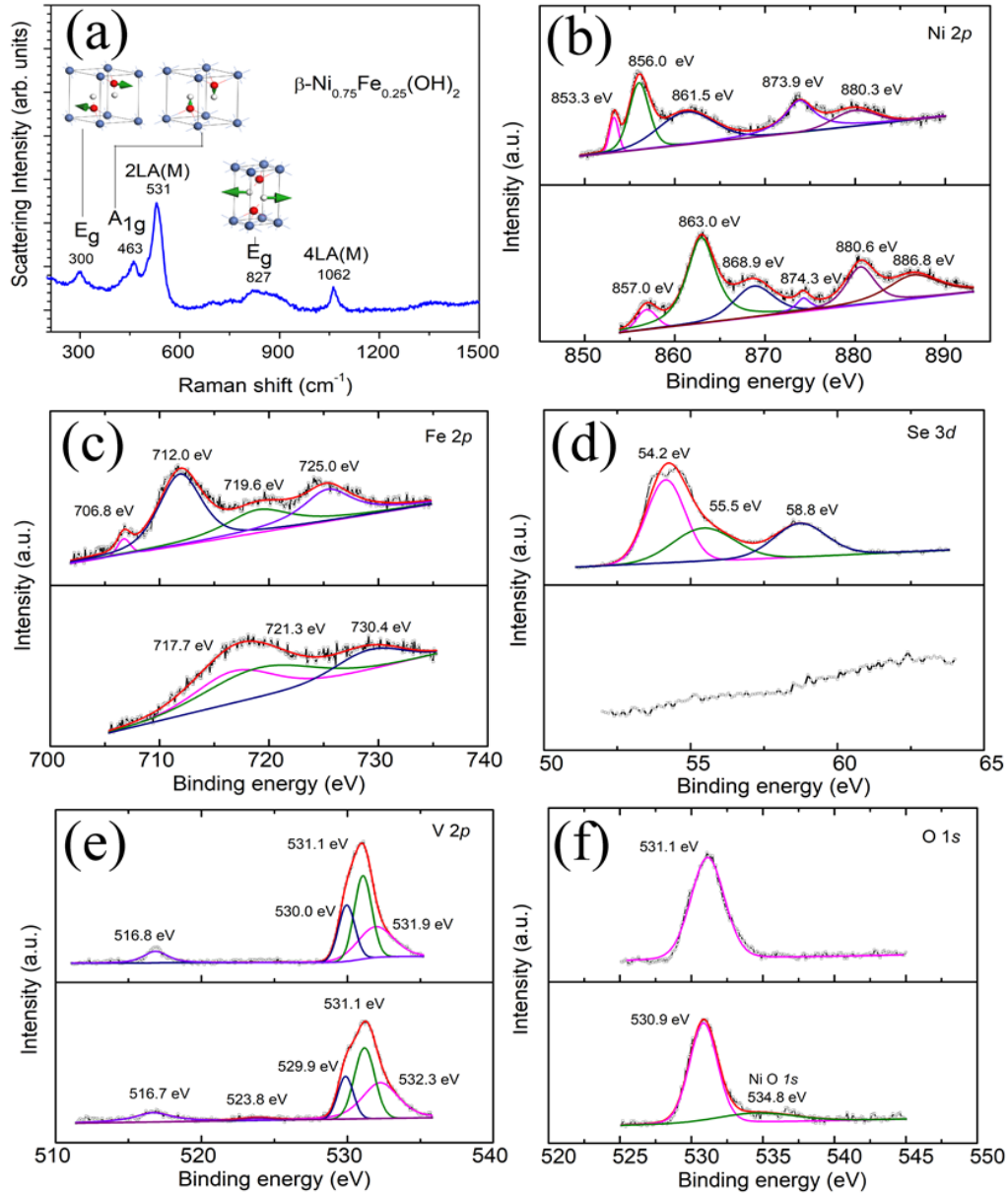


Figure 34 (a) Raman spectrum of $\text{Ni}_{0.75}\text{Fe}_{0.25}\text{Se}_{1.15}$ after water electrolysis. (Atoms: grey - Ni, red - O, and white - H). (b)-(f) High-resolution XPS spectra of as-prepared $\text{Ni}_{0.71}\text{V}_{0.04}\text{Fe}_{0.25}\text{Se}_{1.15}$ (upper panels) and post-OER (lower panels).

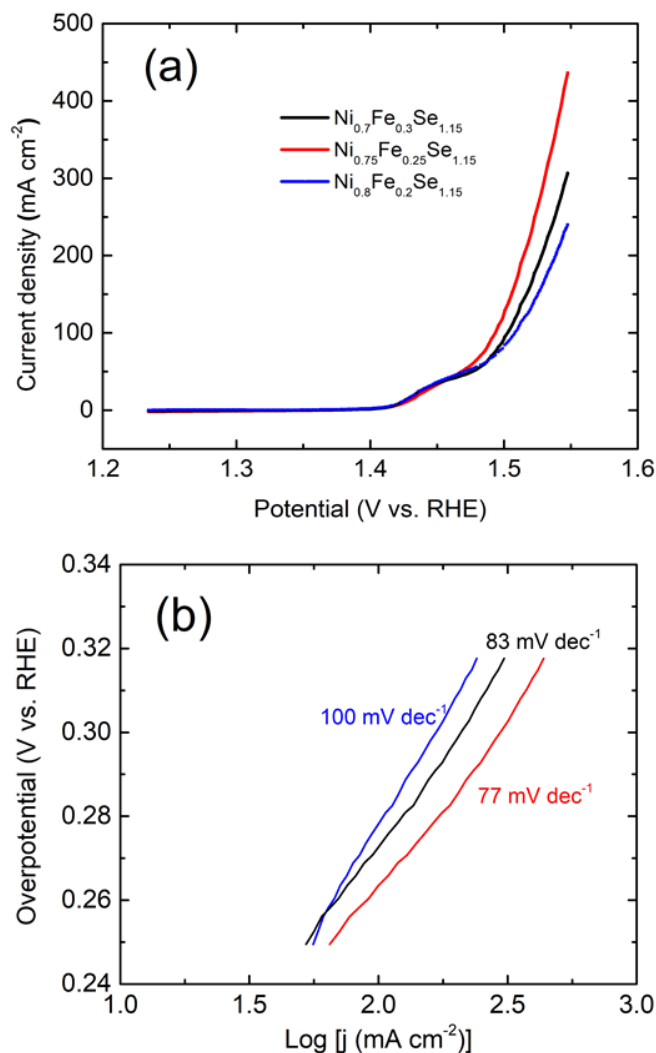
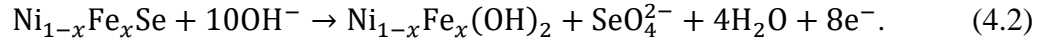
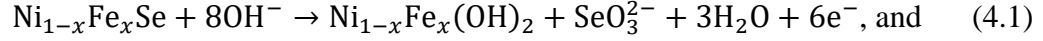


Figure 35 (a) Linear sweep voltammetry curves and (b) the corresponding Tafel plots of Ni_{1-x}Fe_xSe_{1.15} ($x = 0.2, 0.25, \text{ and } 0.3$) compounds after stabilization in 1 M KOH solution.

porous with pores in the range of 10-20 μm , which is due to the Se evaporation and volume expansion at high temperature. It shows that the density of the as-prepared pellets is decreased by 18-22%. The porous structure is advantageous for its larger surface area and exposure of more active sites.^[145] In addition, the grains crystallize well into micro-scale flakes with diameters of 20-30 μm stacked layer by layer, which is consistent with the sharp peak in the X-ray diffraction pattern.

Before conducting the electrochemical activity measurement, cyclic voltammetry (CV) was performed for 1000 cycles in 1 M KOH solution for the catalysts' activation and stabilization, with the potential ranging from 1.4 to 1.8 V vs. RHE and a scan rate of 50 mV s⁻¹. The electrolyte remained crystal clear, and no peeling-off was observed during CV scanning. The polarization curves were measured in alkaline solution, and slightly yellow materials were observed as expected on the surface following OER (Fig. 35), which were investigated by Raman spectroscopy. A typical Raman spectrum of Ni_{0.75}Fe_{0.25}Se_{1.15} after water electrolysis is presented in Fig. 36(a). The spectrum is consistently reproduced at different spots on the samples and reveals Raman lines close to those reported for β-Ni(OH)₂.^[146] The assignment of strongest Raman lines is done in accordance with density functional theory (DFT) lattice dynamics calculations. There are no Raman fingerprints related to any of the Fe hydroxide or oxyhydroxide phases. Fe incorporation of up to 30 at. % in the Ni framework preserves the number and symmetry of Raman lines because the Raman active modes involve only O and H vibrations. The presented Raman characterization indicates that Ni_{1-x}Fe_xSe_{1.15} on the surface is successfully converted to Ni_{1-x}Fe_x(OH)₂ due to electrochemical oxidation during the testing. The surface morphology of the post-OER testing sample was characterized by SEM in Fig. 34(c) and 34(d) and transmission electron microscopy (TEM) in Fig. 34(e) and 34(f). It can be observed that the crystallized micron-sized flakes are fully covered by homogeneous and ultra-thin nanosheets with diameters around 10-20 nm. The morphology of the nanosheets is comparable with that of the previously reported NiFe-LDH.^[147, 148] According to electro-oxidation of metal selenides in alkaline solution, the reactions on the surface during oxidation in water are proposed as following,^[143]



The electrochemical activity of $\text{Ni}_{1-x}\text{Fe}_x\text{Se}_{1.15}$ ($x = 0.2, 0.25, \text{ and } 0.3$) was evaluated by linear sweep voltammetry (LSV) in 1 M KOH solution [Fig. 37(a)]. $\text{Ni}_{0.75}\text{Fe}_{0.25}\text{-LDH}$ exhibits the best performance, achieving current densities of 50 mA cm^{-2} and 100 mA cm^{-2} at overpotentials of 237 mV and 264 mV, respectively, with a high Tafel slope of 77 mV dec^{-1} , shown in Fig. 37 (b). This result prompted us to seek for further improving its catalytic efficiency. The electrochemical impedance spectroscopy (EIS) was conducted to evaluate its capability of charge-transfer capability and Nyquist plots were fitted to a simplified Randles equivalent circuit model. It turns out that as-prepared $\text{Ni}_{0.75}\text{Fe}_{0.25}\text{Se}_{1.15}$ suffers from extremely high charge-transfer resistance at the electrode/electrolyte interface, 90Ω , which is much larger than that of the reported NiFe-LDH.^[149, 150, 151] Thus, the high charge-transfer resistance enlightens us to improve the efficiency of $\text{Ni}_{0.75}\text{Fe}_{0.25}\text{Se}_{1.15}$ by reducing its charge-transfer resistance.

4.3.2 V-doped Ni_{0.75}Fe_{0.25}-LDH for highly efficient OER

The effects of dopants or other transition-metal alloys on NiFe-LDH have been investigated, such as NiFeM ($M = \text{Al}, \text{Mn}, \text{Cr}, \text{and V}$), which show improved OER performance due to the lowering of the free energy of adsorption or desorption or the promotion of charge transfer at the electrode/electrolyte interface.^[152, 153, 154, 155] Jiang *et al.* investigated the effect of Fe and V doping on the OER performance of Ni(OH)₂ by density functional theory (DFT) and *in situ* X-ray absorption spectroscopy and claimed that dopants V and Fe in Ni(OH)₂ offer lower overpotentials and smaller charge-transfer resistance by modifying the catalyst's local coordination environment and electronic structure.^[15] The initial composition Ni_{0.75-y}V_yFe_{0.25}Se_{1.15} ($y = 0.03, 0.04, \text{and } 0.05$) was synthesized by pressing and sintering. The powder X-ray diffraction of the as-prepared

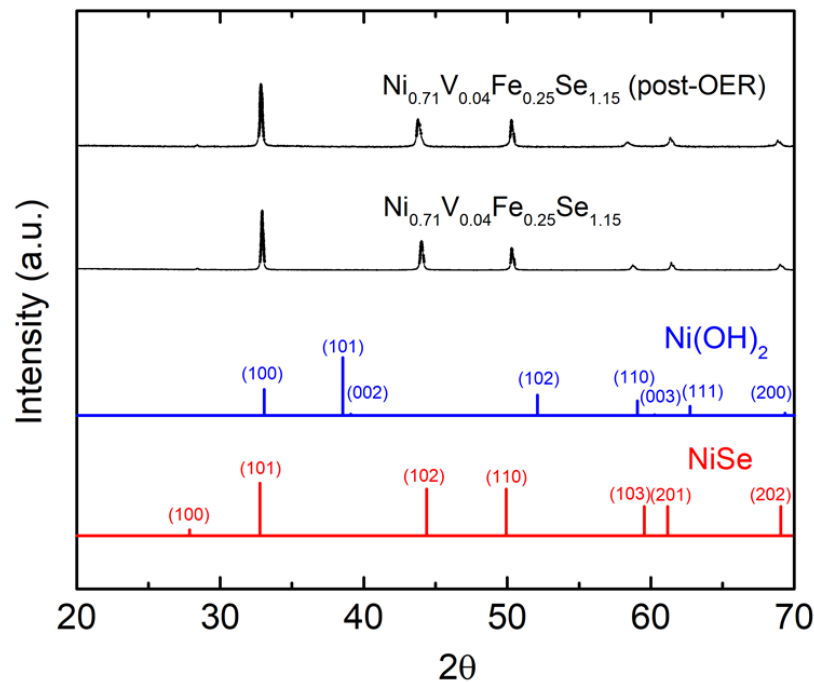


Figure 36 X-ray diffraction patterns of as-prepared $\text{Ni}_{0.71}\text{V}_{0.04}\text{Fe}_{0.25}\text{Se}_{1.15}$ and post-OER $\text{Ni}_{0.71}\text{V}_{0.04}\text{Fe}_{0.25}\text{Se}_{1.15}$.

samples was indexed as NiSe without any impurity phase observed (Fig. 38). After CV scanning, the same slightly yellow products as shown in Fig. 35 were observed on the surface. Ni/Fe hydroxide cannot be identified well by X-ray diffraction, which might be due to the poor crystalline and slight amount. XPS was conducted to investigate the changes of the surface chemical state and the elemental composition of the samples before (upper panels of b-f) and after OER (lower panels of b-f) in Fig. 36. In the upper panel of Fig. 36(b), two characteristic peaks of the as-prepared sample at 853.3 eV and 873.9 eV are assigned to Ni 2p_{3/2} and Ni 2p_{1/2}, respectively, which are followed by two satellite peaks located at 861.5 eV and 880.3 eV. The peak at 856.0 eV indicates the presence of high

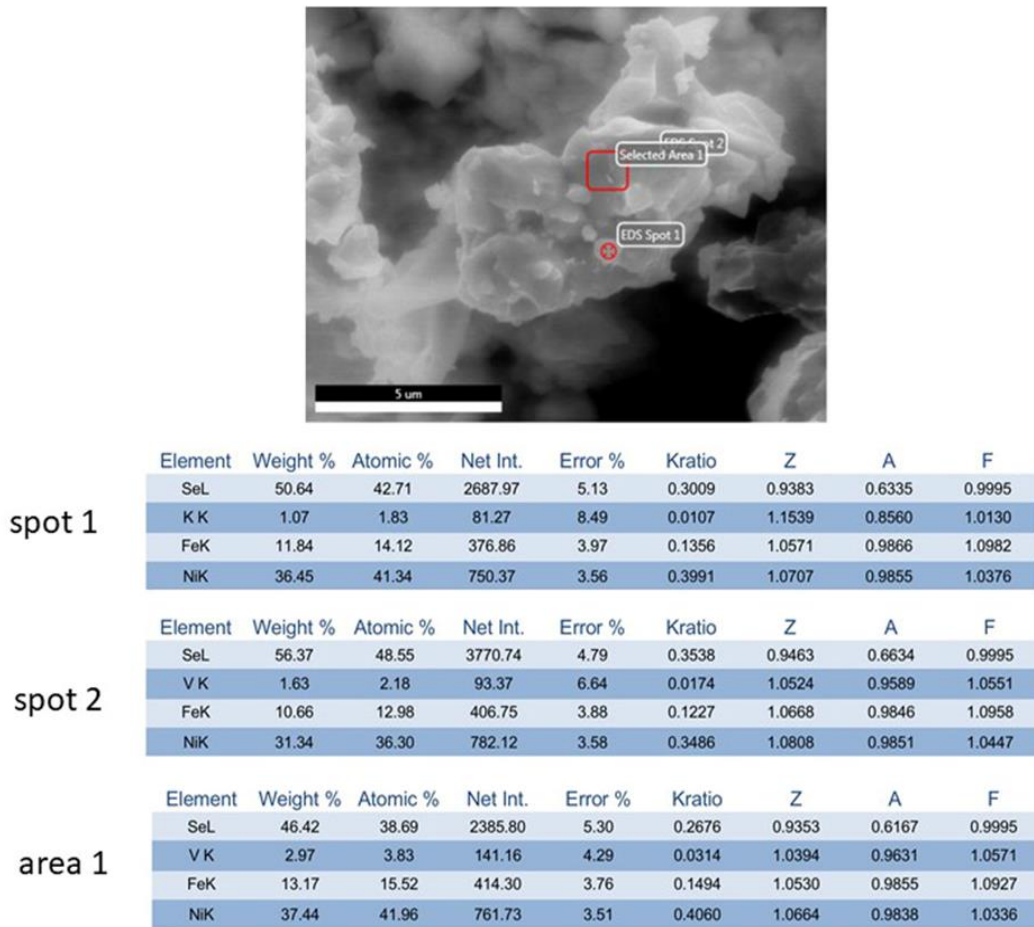
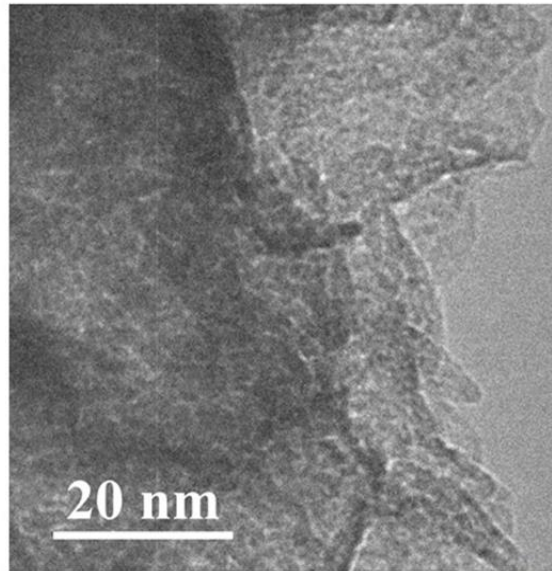


Figure 37 SEM image of the as-prepared Ni_{0.71}V_{0.04}Fe_{0.25}Se_{1.15} and EDS composition analysis of two spots and one area shown in the image

oxidation states Ni^{3+} on the surface. The peaks in the upper panel of Fig. 36(c) at 706.8 eV and 719.6 eV are attributed to Fe $2p_{3/2}$ and Fe $2p_{1/2}$, respectively, and those at 712.0 eV and 725 eV are identified as Fe_2O_3 $2p_{3/2}$ and Fe_2O_3 $2p_{1/2}$, respectively. It is reasonable to detect the high valence states Ni^{3+} and Fe^{3+} on the surface due to the high-temperature preparation process used. In contrast, the binding energy of metal elements exhibits a blue shift after oxidation in water, indicating the increased oxidized states. The peaks in lower panel of



Element	Line Type	k Factor	k Factor type	Absorption Correction	Wt%	Wt% Sigma	Atomic %
O	K series	1.997	Theoretical	1.00	25.58	0.23	56.30
K	K series	1.002	Theoretical	1.00	2.92	0.06	2.63
V	K series	1.127	Theoretical	1.00	0.13	0.03	0.09
Fe	K series	1.165	Theoretical	1.00	11.11	0.12	7.00
Ni	K series	1.202	Theoretical	1.00	34.04	0.20	20.42
Cu	K series	1.297	Theoretical	1.00	19.78	0.17	10.96
Se	K series	1.803	Theoretical	1.00	5.38	0.11	2.40
Pt	L series	2.394	Theoretical	1.00	1.06	0.12	0.19
Total:					100.00		100.00

Figure 38 TEM image of $\text{Ni}_{0.71}\text{V}_{0.04}\text{Fe}_{0.25}\text{Se}_{1.15}$ after OER and EDS composition analysis over the whole image area

Fig. 36(b) at 857.0 eV and 863.0 eV are attributed to Ni 2p_{3/2} and Ni 2p_{1/2} in NiOOH, respectively, accompanied by two satellite peaks at 868.9 eV and 874.3 eV. Peaks at 880.6 eV is assigned to the satellite of Ni³⁺.^[156, 157] The peak in lower panel of Fig. 36(c) between 710.0 eV and 725.0 eV is deconvoluted into two peaks at 717.7 eV and 721.3 eV, which

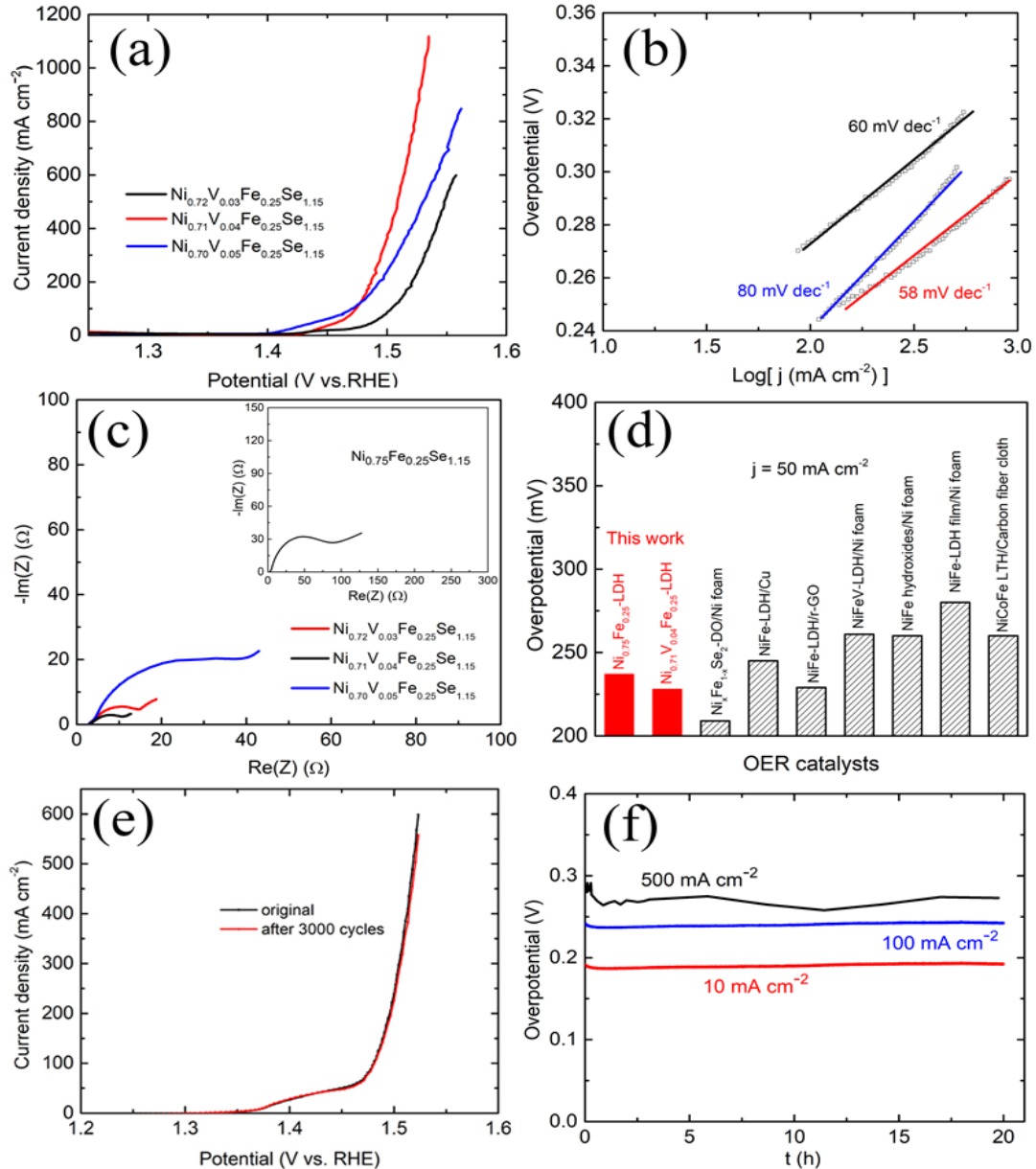


Figure 39 (a) The LSV curves of Ni_{0.75-y}V_yFe_{0.25}Se_{1.15}. (b) The corresponding Tafel slopes. (c) Nyquist plots of Ni_{0.75-y}V_yFe_{0.25}Se_{1.15}. (d) The overpotential comparison at current density of 50 mA cm⁻². (e) and (f) Durability tests.

are attributed to $2p_{3/2}$ and $2p_{1/2}$ of Fe^{3+} , respectively.^[158] The Se $3d$ spectrum shown in the upper panel of Fig. 36(d) exhibits two indistinct peaks at 54.2 eV and 55.5 eV, which are characteristic peaks of Se $3d_{5/2}$ and $3d_{3/2}$, respectively, along with a peak at 58.8 eV, which is possibly related to the selenium oxide. It is noticeable that no distinct Se peak is observed on the surface after oxidation in water, meaning that Se is etched away as indicated in equations 4.1 and 4.2. XPS and energy-dispersive X-ray spectroscopy (EDS) showed that Se content on the surface is decreased from about 50% in the as-prepared sample to less than 5% in the post-OER sample (Fig. 39 and Fig. 40). Fig. 36(e) illustrates the comparison of XPS spectra of V $2p$ for as-prepared (upper panel) and post-OER (lower panel) samples. A pair of peaks separated by around 7.1 eV at 516.7 eV and 523.8 eV are ascribed to V $2p_{3/2}$ and V $2p_{1/2}$, respectively. The peak between 527 eV and 535 eV is attributed to O $1s$, which is deconvoluted into three peaks at 529.9 eV, 531.1 eV, and 532.3 eV. The peak at 529.9 eV might be related to the oxygen in V_2O_5 and the other two are most likely related to the adsorbed oxygen in hydroxide. Moreover, XPS composition analysis shows that the oxygen content in the final product was increased by 20% compared with the as-prepared samples. EDS also verifies that the oxygen content comprises around 56% of the atoms in the specimen after oxidation in water. The ratio of Ni/Fe remains constant at 3/1 after oxidation in water. It can thus be concluded that $\text{Ni}_{0.75}\text{Fe}_{0.25}\text{Se}_{1.15}$ on the surface is converted to $\text{Ni}_{0.75}\text{Fe}_{0.25}$ -LDH during the OER process.

The catalytic activity of $\text{Ni}_{0.75-y}\text{V}_y\text{Fe}_{0.25}\text{Se}_{1.15}$ ($y = 0.03, 0.04, \text{ and } 0.05$) for OER was examined in 1 M KOH solution shown in Fig. 41(a). Commercial Ni foam exhibits trivial OER activity with current density of 10 mA cm^{-2} at overpotential of 340 mV [Fig. 42(a)]. In contrast, porous bulk $\text{Ni}_{0.71}\text{V}_{0.04}\text{Fe}_{0.25}$ -LDH achieved current densities of 100 mA

cm^{-2} , 500 mA cm^{-2} , and 1000 mA cm^{-2} at overpotentials of 244 mV, 278 mV, and 300 mV, respectively, which is better than most reported 3D-structure Ni/Fe(OH)₂ and NiFe-LDH. Fig. 41(b) illustrates the Tafel slope dependence on V dopant content for Ni_{0.75-y}V_yFe_{0.25}Se_{1.15} ($y = 0.03, 0.04, \text{ and } 0.05$). It is notable that the V-doped compound presents lower Tafel slope values compared to Ni_{1-x}Fe_xSe_{1.15}, which indicates that V indeed facilitates the kinetics for OER and improves the catalytic activity. Ni_{0.71}V_{0.04}Fe_{0.25}Se_{1.15} exhibits the lowest Tafel slope of 58 mV dec^{-1} , which is 25% lower than that of Ni_{0.75}Fe_{0.25}Se_{1.15}. To gain a deeper understanding of the mechanism underlying the highly efficient OER of Ni_{0.71}V_{0.04}Fe_{0.25}Se_{1.15}, EIS was carried out to evaluate the charge transfer

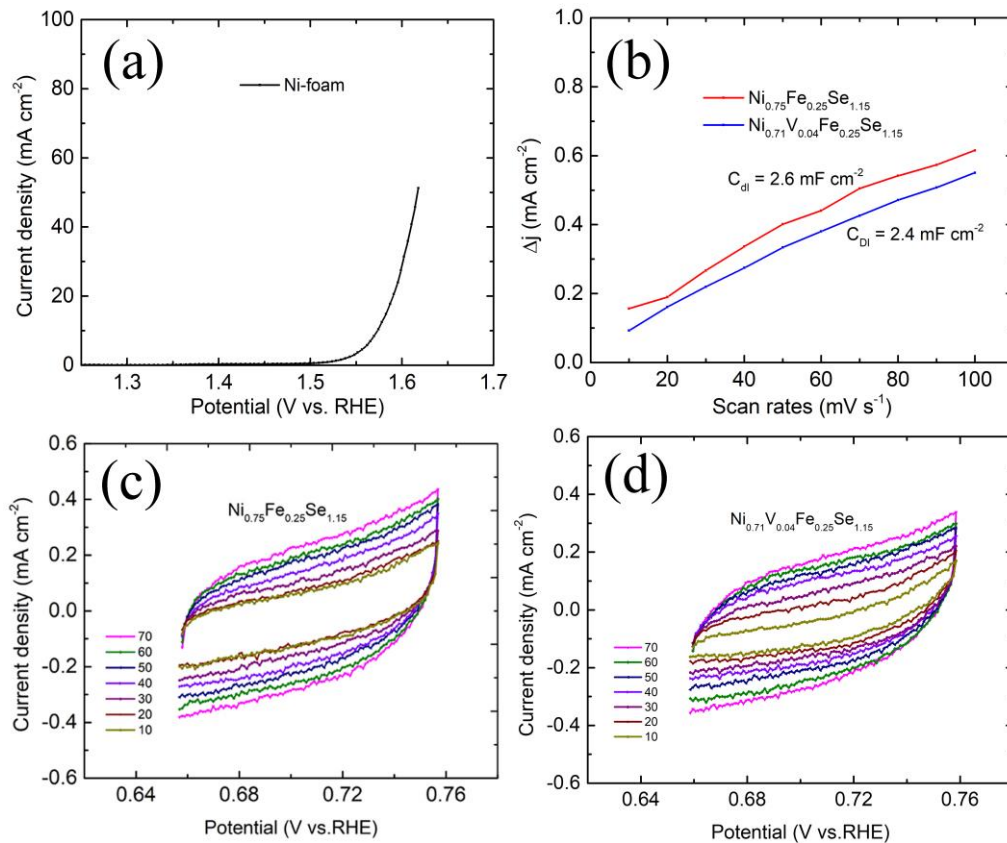


Figure 40 LSV curves of commercial Ni foam. (b) Linear fitting of the capacitive currents as a function of scan rate. (c) Double-layer capacitance (C_{dl}) measurement of Ni_{0.75}Fe_{0.25}Se_{1.15} and (d) Ni_{0.71}V_{0.04}Fe_{0.25}Se_{1.15}.

at the electrode/electrolyte interfaces. It can be observed in Fig. 41(c) that V doping leads to a large decrease in charge-transfer resistance at the electrode/electrolyte interfaces. Compared with resistance of 90 Ω for $\text{Ni}_{0.75}\text{Fe}_{0.25}\text{Se}_{1.15}$, $\text{Ni}_{0.71}\text{V}_{0.04}\text{Fe}_{0.25}\text{Se}_{1.15}$ exhibits resistance of around 9 Ω , which contributes fast charge transfer to the superionic OER performance. $\text{Ni}_{0.71}\text{V}_{0.04}\text{Fe}_{0.25}$ -LDH benefits from the presence of the improved charge-transfer conductance and lower Tafel slope, which is consistent with the previous DFT calculation and experimental demonstration.^[15] Fig. 41(d) also plot the overpotential comparison of our catalysts at 50 mA cm^{-2} with most recently reported NiFe-LDH or NiFeM-layer triple hydroxide supported by different kinds of substrates.

Key aspects of efficient OER electrocatalysts are having a large enough surface area and exposure of as many active sites on the surface as possible. The electrochemically active surface area was estimated by the double-layer capacitance (C_{dl}) [Fig. 42 (b)]. The porous bulk $\text{Ni}_{1-x}\text{Fe}_x\text{Se}_{1.15}$ does not exhibit too distinguished a capacitive current value, less than 3 mF cm^{-2} , and even that with dopant V is much lower in comparison with 3D NiFe-LDH synthesized using hydrothermal methods and electrochemical deposition.^[159, 160] This small electrochemically active surface area most likely results from the fabrication process. On the other hand, it verifies the higher intrinsic catalytic activity for OER that this material exhibits. New methods to expose more active sites are being studied, which may lead to drastic improvement.

Finally, good stability and robustness of catalysts are indispensable requirements for large-scale applications. The stability of $\text{Ni}_{0.71}\text{V}_{0.04}\text{Fe}_{0.25}$ -LDH was assessed by cyclic voltammetry scanning and long-duration chronopotentiometric experiments in Fig. 41(e) and (f). The cyclic voltammetry was conducted over 3000 cycles in 1 M KOH solution

with voltage ranging from 1.175 V to 1.675 V vs. RHE. The polarization curve of the sample after 3000 cycles overlaps very well with the initial one. The sample was then subjected to persistent OER at constant current densities of 10 mA cm⁻², 100 mA cm⁻², and 500 mA cm⁻² for 20 hours, and the recorded voltages are not degraded at all, revealing its excellent stability and robustness under OER conditions, which can most likely be ascribed to its robust mechanical properties of the structure.

4.3.3 Conclusions

This work demonstrated a new route to synthesize highly efficient and robust catalysts for oxygen evolution reaction in alkaline solution. The surface of the porous bulk Ni_{1-x}Fe_xSe_{1.15} was successfully converted to Ni_{0.75}Fe_{0.25}-layer double hydroxide by oxidation in water through cycling voltammetry. Ni_{0.71}V_{0.04}Fe_{0.25}-LDH achieved current densities of 100 mA cm⁻² and 1000 mA cm⁻² at overpotentials of 244 mV and 300 mV vs. RHE, respectively, and displayed a low Tafel slope of 58 mV dec⁻¹. Vanadium doping mainly promotes electron transfer at the electrode/electrolyte interface, thus facilitates the OER kinetics. Its excellent stability and robustness are attributed to the good mechanical properties from the sample preparation method. To further improve the catalytic efficiency of this material, achieving lower charge-transfer resistance and a larger electrochemical active surface area would be feasible.

Chapter 5 Summary

The commercialization of thermoelectric materials is mainly limited in deep-space exploration, or cutting-edge electronics due to their high cost corresponding to the efficiency. Significant improvements of thermoelectric performance have been achieved and the principle have been explained in different kinds of thermoelectric materials. In my work, the anisotropy properties of n-type Mg_3Sb_2 -based compounds are investigated through the grain alignment and the average ZT of 1.1 was demonstrated. Additionally, we realized single crystal of n-type Mg_3Sb_2 would be very important for further investigating the anisotropic properties, and high mobility and power factor could be expected in (001) plane. Due to the low formation energy of Mg vacancies, n-type Mg_3Sb_2 -based single crystal are very challenged for the fabrication process.

We also find out that Y was a strong and effective donor in Mg_3Sb_2 -based compounds. A record ZT value of 1.8 at 773 K was obtained by optimizing the carrier concentration. For further performance enhancement, higher carrier concentration for good electrical conductivity at high temperature are still needed, which might be pursued by modulation doping, emerging filtering or band convergence.

Although water electrolysis has been applied in industry for years, and the mechanisms of hydrogen evolution reaction and oxygen evolution reaction also have been gradually understood in recent years. Cost-effective and highly efficient catalysts or advanced electrolysis technology are still being pursued. We developed a new route to produce catalysts for OER, which is highly active and cost-effective. But the efficiency of porous bulk catalysts is still suppressed by the small electrochemical active surface area and large charge transfer resistance. Further improvement can be carried out by combining

the nano-sized powdery catalysts with three-dimensional metal substrates. In addition, this process can be widely introduced to produce other transition-metal based catalysts or precursor.

Both the fundamental principle investigation and performance pursuit target the materials towards commercialization. Materials exhibit different preferential properties is based on their structure advantages. Either thermoelectric materials or electrochemical catalysts, the advanced production process and precise structure design in micro, nano or atomic scale would be helpful for their purpose in future.

References

- [1] D. Cheikh, B. E. Hogan, T. Vo, P. Von Allmen, K. Lee, D. M. Smiadak, A. Zevalkink, B. S. Dunn, J.-P. Fleurial, S. K. Bux, "Praseodymium telluride: a high-temperature, high-ZT thermoelectric material," *Joule* 2018, 2, 698.
- [2] S. Chen, Z. Ren, "Recent progress of half-Heusler for moderate temperature thermoelectric applications," *Mater. Today* 2013, 16, 387.
- [3] W. Liu, J. Hu, S. Zhang, M. Deng, C.-G. Han, Y. Liu, "New trends, strategies and opportunities in thermoelectric materials: A perspective," *Mater. Today Phys.* 2017, 1, 50.
- [4] Z. Liu, J. Mao, J. Sui, Z. Ren, "High thermoelectric performance of α -MgAgSb for power generation," *Energy Environ. Sci.* 2017, 11, 23.
- [5] J. Shuai, J. Mao, S. Song, Q. Zhang, G. Chen, Z. Ren, "Recent progress and future challenges on thermoelectric Zintl materials," *Mater. Today Phys.* 2017, 1, 74.
- [6] L. Yang, Z.-G. Chen, M. S. Dargusch, J. Zou, "High Performance Thermoelectric Materials: Progress and Their Applications," *Adv. Energy Mater.* 2017, 1701797.
- [7] T. Zhu, Y. Liu, C. Fu, J. P. Heremans, J. G. Snyder, X. Zhao, "Compromise and synergy in high-efficiency thermoelectric materials," *Adv. Mater.* 2017, 29, 1605884.
- [8] X. Zhang, L.-D. Zhao, "Thermoelectric materials: Energy conversion between heat and electricity," *J. Materiomics* 2015, 1, 92.
- [9] X. Shi, L. Chen, C. Uher, "Recent advances in high-performance bulk thermoelectric materials," *Int. Mater. Rev.* 2016, 61, 379.
- [10] http://ieahydrogen.org/pdfs/Global-Outlook-and-Trends-for-Hydrogen_Dec_2017_WEB.aspx.

- [11] F. Yu, L. Yu, I. K. Mishra, Y. Yu, Z. F. Ren, H. Q. Zhou, "Recent developments in earth-abundant and non-noble electrocatalysts for water electrolysis," *Mater. Today Phys.* 2018, 7, 121.
- [12] K. Zeng, D. Zhang, "Recent progress in alkaline water electrolysis for hydrogen production and applications," *Prog. Energy Combust. Sci.* 2010, 36, 307.
- [13] B. You, Y. Sun, "Innovative strategies for electrocatalytic water splitting," *Acc. Chem. Res.* 2018, 51, 1571.
- [14] B. You, G. Han, Y. Sun, "Electrocatalytic and photocatalytic hydrogen evolution integrated with organic oxidation," *Chem. Commun. (Camb)* 2018, 54, 5943.
- [15] J. Jiang, F. Sun, S. Zhou, W. Hu, H. Zhang, J. Dong, Z. Jiang, J. Zhao, J. Li, W. Yan, M. Wang, "Atomic-level insight into super-efficient electrocatalytic oxygen evolution on iron and vanadium co-doped nickel (oxy)hydroxide," *Nat. Commun.* 2018, 9, 2885.
- [16] H. Zhou, F. Yu, Y. Huang, J. Sun, Z. Zhu, R. J. Nielsen, R. He, J. Bao, W. A. Goddard, III, S. Chen, Z. Ren, "Efficient hydrogen evolution by ternary molybdenum sulfoselenide particles on self-standing porous nickel diselenide foam," *Nat. Commun.* 2016, 7, 12765.
- [17] H. Zhou, Y. Wang, R. He, F. Yu, J. Sun, F. Wang, Y. Lan, Z. Ren, S. Chen, "One-step synthesis of self-supported porous NiSe₂/Ni hybrid foam: An efficient 3D electrode for hydrogen evolution reaction," *Nano Energy* 2016, 20, 29.
- [18] C. Tang, L. Gan, R. Zhang, W. Lu, X. Jiang, A. M. Asiri, X. Sun, J. Wang, L. Chen, "Ternary Fe_xCo_{1-x}P nanowire array as a robust hydrogen evolution reaction electrocatalyst with Pt-like activity: experimental and theoretical insight," *Nano Lett.* 2016, 16, 6617.

- [19] M. W. Louie, A. T. Bell, "An investigation of thin-film Ni-Fe oxide catalysts for the electrochemical evolution of oxygen," *J. Am. Chem. Soc.* 2013, 135, 12329.
- [20] M. Gong, Y. Li, H. Wang, Y. Liang, J. Z. Wu, J. Zhou, J. Wang, T. Regier, F. Wei, H. Dai, "An advanced Ni-Fe layered double hydroxide electrocatalyst for water oxidation," *J. Am. Chem. Soc.* 2013, 135, 8452.
- [21] Y. Jin, X. Yue, C. Shu, S. Huang, P. K. Shen, "Three-dimensional porous MoNi₄ networks constructed by nanosheets as bifunctional electrocatalysts for overall water splitting," *J. Mater. Chem. A* 2017, 5, 2508.
- [22] N. T. Suen, S. F. Hung, Q. Quan, N. Zhang, Y. J. Xu, H. M. Chen, "Electrocatalysis for the oxygen evolution reaction: recent development and future perspectives," *Chem. Soc. Rev.* 2017, 46, 337.
- [23] I. Roger, M. A. Shipman, M. D. Symes, "Earth-abundant catalysts for electrochemical and photoelectrochemical water splitting," *Nat. Rev. Chem.* 2017, 1, 0003.
- [24] X. Shi, L. Chen, "Thermoelectric materials step up," *Nat. Mater.* 2016, 15, 691.
- [25] J. He, T. M. Tritt, "Advances in thermoelectric materials research: Looking back and moving forward," *Science* 2017, 357, 1369.
- [26] D.M.Rowe, Thermoelectrics Handbook, CRC Press, Taylor Francis Group, LLC 2006.
- [27] D. Champier, "Thermoelectric generators: A review of applications," *Energy Convers. Manag.* 2017, 140, 167.
- [28] S. D. Kang, J.-H. Pöhls, U. Aydemir, P. Qiu, C. C. Stoumpos, R. Hanus, M. A. White, X. Shi, L. Chen, M. G. Kanatzidis, G. J. Snyder, "Enhanced stability and

thermoelectric figure-of-merit in copper selenide by lithium doping," *Mater. Today Phys.* 2017, 1, 7.

[29] H. Zhou, F. Yu, Y. Liu, J. Sun, Z. Zhu, R. He, J. Bao, W. A. Goddard, S. Chen, Z. Ren, "Outstanding hydrogen evolution reaction catalyzed by porous nickel diselenide electrocatalysts," *Energy Environ. Sci.* 2017, 10, 1487.

[30] S. Song, J. Wang, B. Xu, X. Lei, H. Jiang, Y. Jin, Q. Zhang, Z. Ren, "Thermoelectric properties of n-type $\text{Bi}_2\text{Te}_{2.7}\text{Se}_{0.3}$ with addition of nano-ZnO:Al particles," *Mater. Res. Express* 2014, 1, 035901.

[31] C. B. Vining, "A model for the high-temperature transport properties of heavily doped n-type silicon-germanium alloys," *J. Appl. Phys.* 1991, 69, 331.

[32] E. Flage-Larsen, Ø. Prytz, "The Lorenz function: Its properties at optimum thermoelectric figure-of-merit," *Appl. Phys. Lett.* 2011, 99, 202108.

[33] J. Zhou, H. Zhu, T. H. Liu, Q. Song, R. He, J. Mao, Z. Liu, W. Ren, B. Liao, D. J. Singh, Z. Ren, G. Chen, "Large thermoelectric power factor from crystal symmetry-protected non-bonding orbital in half-Heuslers," *Nat. Commun.* 2018, 9, 1721.

[34] Z. H. Dughaish, "Lead telluride as a thermoelectric materials for thermoelectric power generation," *Phys. B* 2002, 322, 205.

[35] L. You, Y. Liu, X. Li, P. Nan, B. Ge, Y. Jiang, P. Luo, S. Pan, Y. Pei, W. Zhang, G. J. Snyder, J. Yang, J. Zhang, J. Luo, "Boosting the thermoelectric performance of PbSe through dynamic doping and hierarchical phonon scattering," *Energy Environ. Sci.* 2018, 11, 1848.

[36] S. W. Song, J. Mao, M. Bordelon, R. He, Y. M. Wang, J. Shuai, J. Y. Sun, X. B. Lei, Z. S. Ren, S. Chen, S. Wilson, K. Nielsch, Q. Y. Zhang, Z. F. Ren, "Joint effect of

magnesium and yttrium on enhancing thermoelectric properties of n-type $\text{Zintl Mg}_{3+\delta}\text{Y}_{0.02}\text{Sb}_{1.5}\text{Bi}_{0.5}$," *Mater. Today Phys.* 2019, 8, 25.

[37] L. D. Hicks, "Effect of quantum-well structure on the thermoelectric figure of merit," *Phys. Rev. B* 1993.

[38] L. D. Hicks, M. S. Dresselhaus, "Thermoelectric figure of merit of a one-dimensional conductor," *Phys. Rev. B* 1993, 47, 16631.

[39] D. Wu, L. D. Zhao, S. Hao, Q. Jiang, F. Zheng, J. W. Doak, H. Wu, H. Chi, Y. Gelbstein, C. Uher, C. Wolverton, M. Kanatzidis, J. He, "Origin of the high performance in GeTe-based thermoelectric materials upon Bi_2Te_3 doping," *J. Am. Chem. Soc.* 2014, 136, 11412.

[40] J. Shuai, J. Mao, S. Song, Q. Zhu, J. Sun, Y. Wang, R. He, J. Zhou, G. Chen, D. J. Singh, Z. Ren, "Tuning the carrier scattering mechanism to effectively improve the thermoelectric properties," *Energy Environ. Sci.* 2017, 10, 799.

[41] T. Berry, C. Fu, G. Auffermann, G. H. Fecher, W. Schnelle, F. Serrano-Sanchez, Y. Yue, H. Liang, C. Felser, "Enhancing thermoelectric performance of TiNiSn half-Heusler compounds *via* modulation doping," *Chem. Mater.* 2017, 29, 7042.

[42] X. Zhang, M. Yin, D. Wang, Y. Pei, S. Gong, L. Huang, J. He, H. Wu, S. J. Pennycook, "Simultaneously enhancing power factor and reducing thermal conductivity of SnTe *via* introducing its analogues," *Energy Environ. Sci.* 2017, 10, 2420.

[43] M. S. Dresselhaus, G. Chen, M. Y. Tang, R. G. Yang, H. Lee, D. Z. Wang, Z. F. Ren, J. P. Fleurial, P. Gogna, "New directions for low-dimensional thermoelectric materials," *Adv. Mater.* 2007, 19, 1043.

- [44] J. P. Makongo, D. K. Misra, X. Zhou, A. Pant, M. R. Shabetai, X. Su, C. Uher, K. L. Stokes, P. F. Poudeu, "Simultaneous large enhancements in thermopower and electrical conductivity of bulk nanostructured half-Heusler alloys," *J. Am. Chem. Soc.* 2011, 133, 18843.
- [45] K. Berland, X. Song, P. A. Carvalho, C. Persson, T. G. Finstad, O. M. Løvvik, "Enhancement of thermoelectric properties by energy filtering: Theoretical potential and experimental reality in nanostructured ZnSb," *J. Appl. Phys.* 2016, 119, 125103.
- [46] J.-H. Bahk, Z. Bian, A. Shakouri, "Electron transport modeling and energy filtering for efficient thermoelectric $\text{Mg}_2\text{Si}_{1-x}\text{Sn}_x$ solid solutions," *Phys. Rev. B* 2014, 89, 075204.
- [47] T.C. Harman, M. P. Walsh, B. E. LaForge, "Quantum dot superlattice thermoelectric materials and devices," *Science* 2002, 297, 27.
- [48] A. D. LaLonde, Y. Pei, G. J. Snyder, "Reevaluation of $\text{PbTe}_{1-x}\text{I}_x$ as high performance n-type thermoelectric material," *Energy Environ. Sci.* 2011, 4, 2090.
- [49] P. J. Michihiro ohta, A Yamamoto, M.G. Kanatzidis, "Excessively doped PbTe with Ge-Induced nanostructures enables high-efficiency thermoelectric modules," *Joule* 2018, 2, 1339.
- [50] S. Wang, Y. Sun, J. Yang, B. Duan, L. Wu, W. Zhang, J. Yang, "High thermoelectric performance in Te-free $(\text{Bi,Sb})_2\text{Se}_3$ via structural transition induced band convergence and chemical bond softening," *Energy Environ. Sci.* 2016, 9, 3436.
- [51] L. Zhang, Q. Peng, C. Han, J. Wang, Z.-H. Ge, Q. Sun, Z. X. Cheng, S. X. Dou, "Enhanced thermoelectric performance through synergy of resonance levels and valence band convergence via Q/In (Q = Mg, Ag, Bi) co-doping," *J. Mater. Chem. A* 2018, 6, 2507.

- [52] W. Liu, X. Tan, K. Yin, H. Liu, X. Tang, J. Shi, Q. Zhang, C. Uher, "Convergence of conduction bands as a means of enhancing thermoelectric performance of n-type $\text{Mg}_2\text{Si}_{(1-x)}\text{Sn}_{(x)}$ solid solutions," *Phys. Rev. Lett.* 2012, 108, 166601.
- [53] Z. Chen, Z. Jian, W. Li, Y. Chang, B. Ge, R. Hanus, J. Yang, Y. Chen, M. Huang, G. J. Snyder, Y. Pei, "Lattice dislocations enhancing thermoelectric PbTe in addition to band convergence," *Adv. Mater.* 2017, 29.
- [54] Y. Pei, G. Tan, D. Feng, L. Zheng, Q. Tan, X. Xie, S. Gong, Y. Chen, J.-F. Li, J. He, M. G. Kanatzidis, L.-D. Zhao, "Integrating band structure engineering with all-scale hierarchical structuring for high thermoelectric performance in PbTe system," *Adv. Energy Mater.* 2017, 7, 1601450.
- [55] Y. Pei, H. Wang, Z. M. Gibbs, A. D. LaLonde, G. J. Snyder, "Thermopower enhancement in $\text{Pb}_{1-x}\text{Mn}_x\text{Te}$ alloys and its effect on thermoelectric efficiency," *NPG Asia Mater.* 2012, 4, 28.
- [56] J. P. Heremans, V. Jovovic, E. S. Toberer, A. Saramat, K. Kurosaki, A. Charoenphakdee, S. Yamanaka, G. J. Snyder, "Enhancement of Thermoelectric efficiency in PbTe by distortion of the electronic density of states," *Science* 2008, 321, 554.
- [57] Q. Zhang, B. Liao, Y. Lan, K. Lukas, W. Liu, K. Esfarjani, C. Opeil, D. Broido, G. Chen, Z. Ren, "High thermoelectric performance by resonant dopant indium in nanostructured SnTe," *Proc. Natl. Acad. Sci. U.S.A.* 2013, 110, 13261.
- [58] X. Liu, T. Zhu, H. Wang, L. Hu, H. Xie, G. Jiang, G. J. Snyder, X. Zhao, "Low electron scattering potentials in high performance $\text{Mg}_2\text{Si}_{0.45}\text{Sn}_{0.55}$ based thermoelectric solid solutions with band convergence," *Adv. Energy Mater.* 2013, 3, 1238.

- [59] Q. Zhang, H. Wang, W. Liu, H. Wang, B. Yu, Q. Zhang, Z. Tian, G. Ni, S. Lee, K. Esfarjani, G. Chen, Z. Ren, "Enhancement of thermoelectric figure-of-merit by resonant states of aluminium doping in lead selenide," *Energy Environ. Sci.* 2012, 5, 5246.
- [60] K. Biswas, J. He, I. D. Blum, C. I. Wu, T. P. Hogan, D. N. Seidman, V. P. Dravid, M. G. Kanatzidis, "High-performance bulk thermoelectrics with all-scale hierarchical architectures," *Nature* 2012, 489, 414.
- [61] H. Wang, Y. Pei, A. D. LaLonde, G. J. Snyder, "Weak electron-phonon coupling contributing to high thermoelectric performance in n-type PbSe," *Proc. Natl. Acad. Sci. U. S. A.* 2012, 109, 9705.
- [62] Z. Li, C. Xiao, H. Zhu, Y. Xie, "Defect chemistry for thermoelectric materials," *J. Am. Chem. Soc.* 2016, 138, 14810.
- [63] M. Hong, Z. G. Chen, L. Yang, Y. C. Zou, M. S. Dargusch, H. Wang, J. Zou, "Realizing ZT of 2.3 in $\text{Ge}_{1-x-y}\text{Sb}_x\text{In}_y\text{Te}$ via reducing the phase-transition temperature and introducing resonant energy doping," *Adv. Mater.* 2018, 30, 1705942.
- [64] N. Van Nong, N. Pryds, S. Linderoth, M. Ohtaki, "Enhancement of the thermoelectric performance of p-type layered oxide $\text{Ca}_3\text{Co}_4\text{O}_{9+\delta}$ through heavy doping and metallic nano-inclusions," *Adv. Mater.* 2011, 23, 2484.
- [65] Q. Zhang, Q. Zhang, S. Chen, W. Liu, K. Lukas, X. Yan, H. Wang, D. Wang, C. Opeil, G. Chen, Z. Ren, "Suppression of grain growth by additive in nanostructured p-type bismuth antimony tellurides," *Nano Energy* 2012, 1, 183.
- [66] Q. Zhang, E. K. Chere, J. Sun, F. Cao, K. Dahal, S. Chen, G. Chen, Z. Ren, "Studies on thermoelectric properties of n-type Polycrystalline $\text{SnSe}_{1-x}\text{S}_x$ by iodine doping," *Adv. Energy Mater.* 2015, 5, 1500360.

- [67] B. Poudel, Q. Hao, Y. Ma, Y. Lan, A. Minnich, B. Yu, X. Yan, D. Wang, A. Muto, D. Vashaee, "High-thermoelectric performance of nanostructured bismuth antimony telluride bulk alloys," *Science* 2008, 320, 634.
- [68] Z. Chen, B. Ge, W. Li, S. Lin, J. Shen, Y. Chang, R. Hanus, G. J. Snyder, Y. Pei, "Vacancy-induced dislocations within grains for high-performance PbSe thermoelectrics," *Nat. Commun.* 2017, 8, 13828.
- [69] F. Hao, T. Xing, P. Qiu, P. Hu, T. Wei, D. Ren, X. Shi, L. Chen, "Enhanced thermoelectric performance in n-type Bi₂Te₃-based alloys *via* suppressing intrinsic excitation," *ACS Appl. Mater. Interfaces* 2018, 10, 21372.
- [70] T. Berry, C. Fu, G. Auffermann, G. H. Fecher, W. Schnelle, F. Serrano-Sanchez, Y. Yue, H. Liang, C. Felser, "Enhancing thermoelectric performance of TiNiSn half-Heusler compounds *via* modulation doping," *Chem. Mater.* 2017, 29, 7042.
- [71] Y. Tang, X. Li, L. H. J. Martin, E. Cuervo Reyes, T. Ivas, C. Leinenbach, S. Anand, M. Peters, G. J. Snyder, C. Battaglia, "Impact of Ni content on the thermoelectric properties of half-Heusler TiNiSn," *Energy Environ Sci.* 2018, 11, 311.
- [72] G. S. Nolas, D.T. Morelli, Terry M. Tritt, "Skutterudites: a phonon-glass-electron crystal approach to advanced thermoelectric energy conversion application," *Annu. Rev. Mater. Sci.* 1999, 29, 89.
- [73] G. S. Nolas, M. Kaeser, R. T. Littleton, T. M. Tritt, "High figure of merit in partially filled ytterbium skutterudite materials," *Appl. Phys. Lett.* 2000, 77, 1855.
- [74] R. C. Mallik, R. Anbalagan, G. Rogl, E. Royanian, P. Heinrich, E. Bauer, P. Rogl, S. Suwas, "Thermoelectric properties of Fe_{0.2}Co_{3.8}Sb_{12-x}Te_x skutterudites," *Acta Mater.* 2013, 61, 6698.

- [75] M. Rull-Bravo, A. Moure, J. F. Fernández, M. Martín-González, "Skutterudites as thermoelectric materials: revisited," *RSC Adv.* 2015, 5, 41653.
- [76] B. C. Sales, D. Mandrus, B. C. Chakoumakos, V. Keppens, J. R. Thompson, "Filled skutterudite antimonides: Electron crystals and phonon glasses," *Phys. Rev. B* 1997, 56, 15081.
- [77] S. Wang, J. Yang, L. Wu, P. Wei, W. Zhang, J. Yang, "On intensifying carrier impurity scattering to enhance thermoelectric performance in Cr-doped $\text{Ce}_y\text{Co}_4\text{Sb}_{12}$," *Adv. Funct. Mater.* 2015, 25, 6660.
- [78] L.-J. Zhang, B.-P. Zhang, Z.-H. Ge, C.-G. Han, N. Chen, J.-F. Li, "Synthesis and transport properties of AgBi_3S_5 ternary sulfide compound," *Intermetallics* 2013, 36, 96.
- [79] H. Tamaki, H. K. Sato, T. Kanno, "Isotropic conduction network and defect chemistry in $\text{Mg}_{3+\delta}\text{Sb}_2$ -based layered Zintl compounds with high thermoelectric performance," *Adv. Mater.* 2016, 28, 10182.
- [80] F. Li, J.-F. Li, L.-D. Zhao, K. Xiang, Y. Liu, B.-P. Zhang, Y.-H. Lin, C.-W. Nan, H.-M. Zhu, "Polycrystalline BiCuSeO oxide as a potential thermoelectric material," *Energy Environ. Sci.* 2012, 5, 7188.
- [81] B. Yu, W. Liu, S. Chen, H. Wang, H. Wang, G. Chen, Z. Ren, "Thermoelectric properties of copper selenide with ordered selenium layer and disordered copper layer," *Nano Energy* 2012, 1, 472.
- [82] J. Li, J. Sui, Y. Pei, C. Barreateau, D. Berardan, N. Dragoë, W. Cai, J. He, L.-D. Zhao, "A high thermoelectric figure of merit $ZT > 1$ in Ba heavily doped BiCuSeO oxyselenides," *Energy Environ. Sci.* 2012, 5, 8543.

- [83] J. D. Sugar, D. L. Medlin, "Precipitation of Ag_2Te in the thermoelectric material AgSbTe_2 ," *J. Alloy Compd.* 2009, 478, 75.
- [84] H. Wang, J.-F. Li, M. Zou, T. Sui, "Synthesis and transport property of AgSbTe_2 as a promising thermoelectric compound," *Appl. Phys. Lett.* 2008, 93, 202106.
- [85] D. R. Brown, T. Day, T. Caillat, G. J. Snyder, "Chemical Stability of $(\text{Ag,Cu})_2\text{Se}$: a historical overview," *J. Electro. Mater.* 2013, 42, 2014.
- [86] D. Li, X. Y. Qin, Y. F. Liu, C. J. Song, L. Wang, J. Zhang, H. X. Xin, G. L. Guo, T. H. Zou, G. L. Sun, B. J. Ren, X. G. Zhu, "Chemical synthesis of nanostructured Cu_2Se with high thermoelectric performance," *RSC Adv.* 2014, 4, 8638.
- [87] Y. Choquette, H. Ménard, L. Brossard, "Electrocatalytic performance of composite-coated electrodes for alkaline water electrolysis," *International J. Hydrogen Energy* 1990, 15, 21.
- [88] R. N. Singh, D. Mishra, Anindita, A. S. K. Sinha, A. Singh, "Novel electrocatalysts for generating oxygen from alkaline water electrolysis," *Electrochem. Commun.* 2007, 9, 1369.
- [89] X. Li, F. C. Walsh, D. Pletcher, "Nickel based electrocatalysts for oxygen evolution in high current density, alkaline water electrolyzers," *Phys Chem Chem Phys* 2011, 13, 1162.
- [90] P. Chen, K. Xu, Z. Fang, Y. Tong, J. Wu, X. Lu, X. Peng, H. Ding, C. Wu, Y. Xie, "Metallic Co_4N porous nanowire arrays activated by surface oxidation as electrocatalysts for the oxygen evolution reaction," *Angew Chem. Int. Ed. Engl.* 2015, 54, 14710.

- [91] O. Diaz-Morales, I. Ledezma-Yanez, M. T. M. Koper, F. Calle-Vallejo, "Guidelines for the rational design of Ni-based double hydroxide electrocatalysts for the oxygen evolution reaction," *ACS Catalysis* 2015, 5, 5380.
- [92] H. Zhou, F. Yu, Q. Zhu, J. Sun, F. Qin, L. Yu, J. Bao, Y. Yu, S. Chen, Z. Ren, "Water splitting by electrolysis at high current densities under 1.6 volts," *Energy Environ. Sci.* 2018, 11, 2858.
- [93] J. Sun, M. Ren, L. Yu, Z. Yang, L. Xie, F. Tian, Y. Yu, Z. Ren, S. Chen, H. Zhou, "Highly efficient hydrogen evolution from a mesoporous hybrid of nickel phosphide nanoparticles anchored on cobalt phosphosulfide/phosphide nanosheet arrays," *Small* 2019, 1804272.
- [94] Y. Li, H. Wang, L. Xie, Y. Liang, G. Hong, H. Dai, "MoS₂ nanoparticles grown on graphene: an advanced catalyst for the hydrogen evolution reaction," *J. Am. Chem. Soc.* 2011, 133, 7296.
- [95] E. J. Popczun, J. R. McKone, C. G. Read, A. J. Biacchi, A. M. Wiltrout, N. S. Lewis, R. E. Schaak, "Nanostructured nickel phosphide as an electrocatalyst for the hydrogen evolution reaction," *J. Am. Chem. Soc.* 2013, 135, 9267.
- [96] J. Kibsgaard, T. F. Jaramillo, "Molybdenum phosphosulfide: an active, acid-stable, earth-abundant catalyst for the hydrogen evolution reaction," *Angew. Chem. Int. Ed. Engl.* 2014, 53, 14433.
- [97] C. Xu, S. Peng, C. Tan, H. Ang, H. Tan, H. Zhang, Q. Yan, "Ultrathin S-doped MoSe₂ nanosheets for efficient hydrogen evolution," *J. Mater. Chem. A* 2014, 2, 5597.

- [98] I. K. Mishra, H. Zhou, J. Sun, F. Qin, K. Dahal, J. Bao, S. Chen, Z. Ren, "Hierarchical CoP/Ni₅P₄/CoP microsheet arrays as a robust pH-universal electrocatalyst for efficient hydrogen generation," *Energy Environ. Sci.* 2018, 11, 2246.
- [99] X. Lu, C. Zhao, "Electrodeposition of hierarchically structured three-dimensional nickel-iron electrodes for efficient oxygen evolution at high current densities," *Nat. Commun.* 2015, 6, 6616.
- [100] J. Tian, Q. Liu, A. M. Asiri, X. Sun, "Self-supported nanoporous cobalt phosphide nanowire arrays: an efficient 3D hydrogen-evolving cathode over the wide range of pH 0-14," *J. Am. Chem. Soc.* 2014, 136, 7587.
- [101] J. Hao, W. Yang, Z. Zhang, J. Tang, "Metal-organic frameworks derived Co_xFe_{1-x}P nanocubes for electrochemical hydrogen evolution," *Nanoscale* 2015, 7, 11055.
- [102] L. Yu, H. Zhou, J. Sun, I. K. Mishra, D. Luo, F. Yu, Y. Yu, S. Chen, Z. Ren, "Amorphous NiFe layered double hydroxide nanosheets decorated on 3D nickel phosphide nanoarrays: a hierarchical core-shell electrocatalyst for efficient oxygen evolution," *J. Mater. Chem. A* 2018, 6, 13619.
- [103] F. Wang, Y. Li, T. A. Shifa, K. Liu, F. Wang, Z. Wang, P. Xu, Q. Wang, J. He, "Selenium-enriched nickel selenide nanosheets as a robust electrocatalyst for hydrogen generation," *Angew. Chem. Int. Ed. Engl.* 2016, 55, 6919.
- [104] H. Zhou, F. Yu, J. Sun, R. He, S. Chen, C. W. Chu, Z. Ren, "Highly active catalyst derived from a 3D foam of Fe(PO₃)₂/Ni₂P for extremely efficient water oxidation," *Proc. Natl. Acad. Sci. U. S. A.* 2017, 114, 5607.

- [105] M. A. R. Anjum, M. H. Lee, J. S. Lee, "BCN network-encapsulated multiple phases of molybdenum carbide for efficient hydrogen evolution reactions in acidic and alkaline media," *J. Mater. Chem. A* 2017, 5, 13122.
- [106] J. Zhang, T. Wang, P. Liu, Z. Liao, S. Liu, X. Zhuang, M. Chen, E. Zschech, X. Feng, "Efficient hydrogen production on MoNi₄ electrocatalysts with fast water dissociation kinetics," *Nat. Commun.* 2017, 8, 15437.
- [107] F. Song, W. Li, J. Yang, G. Han, P. Liao, Y. Sun, "Interfacing nickel nitride and nickel boosts both electrocatalytic hydrogen evolution and oxidation reactions," *Nat. Commun.* 2018, 9, 4531.
- [108] K. Y. Ma, S. I. Yoon, A. R. Jang, H. Y. Jeong, Y.-J. Kim, P. K. Nayak, H. S. Shin, "Hydrogenation of monolayer molybdenum diselenide via hydrogen plasma treatment," *J. Mater. Chem. C* 2017, 5, 11294.
- [109] M. Caban-Acevedo, M. L. Stone, J. R. Schmidt, J. G. Thomas, Q. Ding, H. C. Chang, M. L. Tsai, J. H. He, S. Jin, "Efficient hydrogen evolution catalysis using ternary pyrite-type cobalt phosphosulphide," *Nat. Mater.* 2015, 14, 1245.
- [110] Y. Hou, M. Qiu, T. Zhang, X. Zhuang, C. S. Kim, C. Yuan, X. Feng, "Ternary porous cobalt phosphoselenide nanosheets: an efficient electrocatalyst for electrocatalytic and photoelectrochemical water splitting," *Adv. Mater.* 2017, 29.
- [111] A. Bhardwaj, A. Rajput, A. K. Shukla, J. J. Pulikkotil, A. K. Srivastava, A. Dhar, G. Gupta, S. Auluck, D. K. Misra, R. C. Budhani, "Mg₃Sb₂-based Zintl compound: a non-toxic, inexpensive and abundant thermoelectric material for power generation," *RSC Adv.* 2013, 3, 8504.

- [112] S. Kim, C. Kim, Y.-K. Hong, T. Onimaru, K. Suekuni, T. Takabatake, M.-H. Jung, "Thermoelectric properties of Mn-doped Mg–Sb single crystals," *J. Mater. Chem. A* 2014, 2, 12311.
- [113] J. Zhang, L. Song, A. Mamakhel, M. R. V. Jørgensen, B. B. Iversen, "High-performance low-cost n-type Se-doped Mg₃Sb₂-based Zintl compounds for thermoelectric application," *Chem. Mater.* 2017, 29, 5371.
- [114] J. Zhang, L. Song, S. H. Pedersen, H. Yin, L. T. Hung, B. B. Iversen, "Discovery of high-performance low-cost n-type Mg₃Sb₂-based thermoelectric materials with multi-valley conduction bands," *Nat. Commun.* 2017, 8, 13901.
- [115] S. Ohno, K. Imasato, S. Anand, H. Tamaki, S. D. Kang, P. Gorai, H. K. Sato, E. S. Toberer, T. Kanno, G. J. Snyder, "Phase boundary mapping to obtain n -type Mg₃Sb₂-based thermoelectrics," *Joule* 2018, 2, 141.
- [116] S. H. Kim, C. M. Kim, Y.-K. Hong, K. I. Sim, J. H. Kim, T. Onimaru, T. Takabatake, M.-H. Jung, "Thermoelectric properties of Mg₃Sb_{2-x}Bi_x single crystals grown by Bridgman method," *Mater. Res. Express* 2015, 2, 055903.
- [117] J. Mao, J. Shuai, S. Song, Y. Wu, R. Dally, J. Zhou, Z. Liu, J. Sun, Q. Zhang, C. dela Cruz, S. Wilson, Y. Pei, D. J. Singh, G. Chen, C.-W. Chu, Z. Ren, "Manipulation of ionized impurity scattering for achieving high thermoelectric performance in n-type Mg₃Sb₂-based materials," *Proc. Natl. Acad. Sci.* 2017, 114, 10548.
- [118] L. D. Zhao, S. H. Lo, Y. Zhang, H. Sun, G. Tan, C. Uher, C. Wolverton, V. P. Dravid, M. G. Kanatzidis, "Ultralow thermal conductivity and high thermoelectric figure of merit in SnSe crystals," *Nature* 2014, 508, 373.

- [119] Y. S. Susumu Miura, Katsushi Fukuda, Keio Nishimura, Keisuke Ikeda, "Texture and thermoelectric properties of hot extruded Bi_2Te_3 compound," *Mater. Sci. Eng. A* 2000, 277,244.
- [120] G. Li, U. Aydemir, M. Wood, Q. An, W. A. Goddard Iii, P. Zhai, Q. Zhang, G. J. Snyder, "Deformation mechanisms in high-efficiency thermoelectric layered Zintl compounds," *J. Mater. Chem. A* 2017, 5, 9050.
- [121] L. D. Zhao, B. P. Zhang, J. F. Li, H. L. Zhang, W. S. Liu, "Enhanced thermoelectric and mechanical properties in textured n-type Bi_2Te_3 prepared by spark plasma sintering," *Solid State Sci.* 2008, 10, 651.
- [122] Z. C. Chen, K. Suzuki, S. Miura, K. Nishimura, K. Ikeda, "Microstructural features and deformation-induced lattice defects in hot-extruded Bi_2Te_3 thermoelectric compound," *Mater. Sci. Eng. A* 2009, 500, 70.
- [123] X. Yan, B. Poudel, Y. Ma, W. S. Liu, G. Joshi, H. Wang, Y. Lan, D. Wang, G. Chen, Z. F. Ren, "Experimental studies on anisotropic thermoelectric properties and structures of n-type $\text{Bi}_2\text{Te}_{2.7}\text{Se}_{0.3}$," *Nano Lett.* 2010, 10, 3373.
- [124] J. Sui, J. Li, J. He, Y.-L. Pei, D. Berardan, H. Wu, N. Dragoe, W. Cai, L.-D. Zhao, "Texturation boosts the thermoelectric performance of BiCuSeO oxyselenides," *Energy Environ. Sci.* 2013, 6, 2916.
- [125] J. Mao, Y. Wu, S. Song, Q. Zhu, J. Shuai, Z. Liu, Y. Pei, Z. Ren, "Defect engineering for realizing high thermoelectric performance in n-type Mg_3Sb_2 -based materials," *ACS Energy Lett.* 2017, 2, 2245.
- [126] X. Chen, H. Wu, J. Cui, Y. Xiao, Y. Zhang, J. He, Y. Chen, J. Cao, W. Cai, S. J. Pennycook, Z. Liu, L.-D. Zhao, J. Sui, "Extraordinary thermoelectric performance in n-

type manganese doped Mg_3Sb_2 Zintl: high band degeneracy, tuned carrier scattering mechanism and hierarchical microstructure," *Nano Energy* 2018, 52, 246.

[127] K. Imasato, S. Ohno, S. D. Kang, G. J. Snyder, "Improving the thermoelectric performance in $\text{Mg}_{3+x}\text{Sb}_{1.5}\text{Bi}_{0.49}\text{Te}_{0.01}$ by reducing excess Mg," *APL Mater.* 2018, 6, 016106.

[128] T. Kanno, H. Tamaki, H. K. Sato, S. D. Kang, S. Ohno, K. Imasato, J. J. Kuo, G. J. Snyder, Y. Miyazaki, "Enhancement of average thermoelectric figure of merit by increasing the grain-size of $\text{Mg}_{3.2}\text{Sb}_{1.5}\text{Bi}_{0.49}\text{Te}_{0.01}$," *Appl. Phys. Lett.* 2018, 112, 033903.

[129] P. Gorai, B. R. Ortiz, E. Toberer, V. Stevanovic, "Investigation of n-type doping strategies for Mg_3Sb_2 ," *J. Mater. Chem. A* 2018, 6, 13806.

[130] X. Xiao, L. Tao, M. Li, X. Lv, D. Huang, X. Jiang, H. Pan, M. Wang, Y. Shen, "Electronic modulation of transition metal phosphide via doping as efficient and pH-universal electrocatalysts for hydrogen evolution reaction," *Chem. Sci.* 2018, 9, 1970.

[131] R. Santos, S. Aminorroaya Yamini, S. X. Dou, "Recent progress in magnesium-based thermoelectric materials," *J. Mater. Chem. A* 2018, 6, 3328.

[132] J. Shuai, B. Ge, J. Mao, S. Song, Y. Wang, Z. Ren, "Significant role of mg stoichiometry in designing high thermoelectric performance for $\text{Mg}_3(\text{Sb,Bi})_2$ -based n-type Zintl," *J. Am. Chem. Soc.* 2018, 140, 1910.

[133] S. Song, J. Mao, J. Shuai, H. Zhu, Z. Ren, U. Saparamadu, Z. Tang, B. Wang, Z. Ren, "Study on anisotropy of n-type Mg_3Sb_2 -based thermoelectric materials," *Appl. Phys. Lett.* 2018, 112, 092103.

- [134] S. Ohno, K. Imasato, S. Anand, H. Tamaki, S. D. Kang, P. Gorai, H. K. Sato, E. S. Toberer, T. Kanno, G. J. Snyder, "Phase boundary mapping to obtain n-type Mg_3Sb_2 -based thermoelectrics," *Joule* 2018, 2, 141.
- [135] R. Asahi, T. Morikawa, H. Hazama, M. Matsubara, "Materials design and development of functional materials for industry," *J. Phys. Condens. Matter.* 2008, 20, 064227.
- [136] T. J. Zhu, K. Xiao, C. Yu, J. J. Shen, S. H. Yang, A. J. Zhou, X. B. Zhao, J. He, "Effects of yttrium doping on the thermoelectric properties of $\text{Hf}_{0.6}\text{Zr}_{0.4}\text{NiSn}_{0.98}\text{Sb}_{0.02}$ half-Heusler alloys," *J. Appl. Phys.* 2010, 108, 044903.
- [137] X. Cui, P. Ren, D. Deng, J. Deng, X. Bao, "Single layer graphene encapsulating non-precious metals as high-performance electrocatalysts for water oxidation," *Energy Environ. Sci.* 2016, 9, 123.
- [138] M. Gong, H. Dai, "A mini review of NiFe-based materials as highly active oxygen evolution reaction electrocatalysts," *Nano Res.* 2014, 8, 23.
- [139] F. Wang, J. Li, F. Wang, T. A. Shifa, Z. Cheng, Z. Wang, K. Xu, X. Zhan, Q. Wang, Y. Huang, C. Jiang, J. He, "Enhanced electrochemical H_2 evolution by few-layered metallic $\text{WS}_{2(1-x)}\text{Se}_{2x}$ Nanoribbons," *Adv. Func. Mater.* 2015, 25, 6077.
- [140] L. Su, X. Cui, T. He, L. Zeng, H. Tian, Y. Song, K. Qi, B. Y. Xia, "Surface reconstruction of cobalt phosphide nanosheets by electrochemical activation for enhanced hydrogen evolution in alkaline solution," *Chem. Sci.* 2019, 9, 1970.
- [141] B. Poudel, Q. Hao, Y. Ma, Y. Lan, A. Minnich, B. Yu, X. Yan, D. Wang, A. Muto, D. Vashaee, X. Chen, J. Liu, M. S. Dresselhaus, G. Chen, Z. Ren, "High-thermoelectric

performance of nanostructured bismuth antimony telluride bulk alloys," *Science* 2008, 320, 634.

[142] A. Grimaud, O. Diaz-Morales, B. Han, W. T. Hong, Y. L. Lee, L. Giordano, K. A. Stoerzinger, M. T. M. Koper, Y. Shao-Horn, "Activating lattice oxygen redox reactions in metal oxides to catalyse oxygen evolution," *Nat. Chem.* 2017, 9, 457.

[143] W. K. A. Thomas C. Franklin, and Remi Nnodimele, "The electro-oxidation of some insoluble inorganic sulfides, selenides, and tellurides in cationic surfactant-aqueous sodium hydroxide systems," *J. Electro. Soc.* 1990, 137.

[144] X. Xu, F. Song, X. Hu, "A nickel iron diselenide-derived efficient oxygen-evolution catalyst," *Nat. Commun.* 2016, 7, 12324.

[145] S. A. Chala, M.-C. Tsai, W.-N. Su, K. B. Ibrahim, A. D. Duma, M.-H. Yeh, C.-Y. Wen, C.-H. Yu, T.-S. Chan, H. Dai, B.-J. Hwang, "Site activity and population engineering of NiRu-layered double hydroxide nanosheets decorated with silver nanoparticles for oxygen evolution and reduction reactions," *ACS Catalysis* 2018, 9, 117.

[146] D. S. Hall, D. J. Lockwood, S. Poirier, C. Bock, B. R. MacDougall, "Raman and infrared spectroscopy of alpha and beta phases of thin nickel hydroxide films electrochemically formed on nickel," *J. Phys. Chem. A* 2012, 116, 6771.

[147] K. N. Dinh, P. Zheng, Z. Dai, Y. Zhang, R. Dangol, Y. Zheng, B. Li, Y. Zong, Q. Yan, "Ultrathin porous NiFeV ternary layer hydroxide nanosheets as a highly efficient bifunctional electrocatalyst for overall water splitting," *Small* 2018, 14, 1703257.

[148] S. Fu, J. Song, C. Zhu, G.-L. Xu, K. Amine, C. Sun, X. Li, M. H. Engelhard, D. Du, Y. Lin, "Ultrafine and highly disordered Ni₂Fe₁ nanofoams enabled highly efficient oxygen evolution reaction in alkaline electrolyte," *Nano Energy* 2018, 44, 319.

- [149] Y. Liu, X. Liang, L. Gu, Y. Zhang, G. D. Li, X. Zou, J. S. Chen, "Corrosion engineering towards efficient oxygen evolution electrodes with stable catalytic activity for over 6000 hours," *Nat. Commun.* 2018, 9, 2609.
- [150] Z. Lu, W. Xu, W. Zhu, Q. Yang, X. Lei, J. Liu, Y. Li, X. Sun, X. Duan, "Three-dimensional NiFe layered double hydroxide film for high-efficiency oxygen evolution reaction," *Chem. Commun. (Camb)* 2014, 50, 6479.
- [151] L. Yu, H. Zhou, J. Sun, F. Qin, F. Yu, J. Bao, Y. Yu, S. Chen, Z. Ren, "Cu nanowires shelled with NiFe layered double hydroxide nanosheets as bifunctional electrocatalysts for overall water splitting," *Energy Environ. Sci.* 2017, 10, 1820.
- [152] J. Y. C. Chen, J. T. Miller, J. B. Gerken, S. S. Stahl, "Inverse spinel NiFeAlO₄ as a highly active oxygen evolution electrocatalyst: promotion of activity by a redox-inert metal ion," *Energy Environ. Sci.* 2014, 7, 1382.
- [153] E. Detsi, J. B. Cook, B. K. Lesel, C. L. Turner, Y.-L. Liang, S. Robbennolt, S. H. Tolbert, "Mesoporous Ni₆₀Fe₃₀Mn₁₀-alloy based metal/metal oxide composite thick films as highly active and robust oxygen evolution catalysts," *Energy Environ. Sci.* 2016, 9, 540.
- [154] K. Fan, H. Chen, Y. Ji, H. Huang, P. M. Claesson, Q. Daniel, B. Philippe, H. Rensmo, F. Li, Y. Luo, L. Sun, "Nickel-vanadium monolayer double hydroxide for efficient electrochemical water oxidation," *Nat. Commun.* 2016, 7, 11981.
- [155] C. Schwanke, H. S. Stein, L. Xi, K. Sliozberg, W. Schuhmann, A. Ludwig, K. M. Lange, "Correlating oxygen evolution catalysts activity and electronic structure by a high-throughput investigation of Ni_{1-y-z}Fe_yCr_zO_x," *Sci. Rep.* 2017, 7, 44192.
- [156] D. Friebel, M. W. Louie, M. Bajdich, K. E. Sanwald, Y. Cai, A. M. Wise, M. J. Cheng, D. Sokaras, T. C. Weng, R. Alonso-Mori, R. C. Davis, J. R. Bargar, J. K. Norskov,

- A. Nilsson, A. T. Bell, "Identification of highly active Fe sites in (Ni,Fe)OOH for electrocatalytic water splitting," *J. Am. Chem. Soc.* 2015, 137, 1305.
- [157] B. J. Trzesniewski, O. Diaz-Morales, D. A. Vermaas, A. Longo, W. Bras, M. T. Koper, W. A. Smith, "In situ observation of active oxygen species in Fe-containing Ni-based oxygen evolution catalysts: the effect of pH on electrochemical activity," *J. Am. Chem. Soc.* 2015, 137, 15112.
- [158] W. D. Chemelewski, H. C. Lee, J. F. Lin, A. J. Bard, C. B. Mullins, "Amorphous FeOOH oxygen evolution reaction catalyst for photoelectrochemical water splitting," *J. Am. Chem. Soc.* 2014, 136, 2843.
- [159] A.-L. Wang, H. Xu, G.-R. Li, "NiCoFe layered triple hydroxides with porous structures as high-performance electrocatalysts for overall water splitting," *ACS Energy Lett.* 2016, 1, 445.
- [160] P. Zhang, L. Li, D. Nordlund, H. Chen, L. Fan, B. Zhang, X. Sheng, Q. Daniel, L. Sun, "Dendritic core-shell nickel-iron-copper metal/metal oxide electrode for efficient electrocatalytic water oxidation," *Nat. Commun.* 2018, 9, 381.

List of Publications

- [1] Shaowei Song, Luo Yu, Viktor G. Hadjiev, Wenyu Zhang, Dezhi Wang, Xin Xiao, Shuo Chen, Qinyong Zhang, Zhifeng Ren, A new way to synthesize robust and porous V-doped $\text{Ni}_{1-x}\text{Fe}_x$ layered double hydroxide for efficient electrocatalytic oxygen evolution (submitted).
- [2] Shaowei Song, Bifunctional electrocatalysts metal phosphate for highly efficient overall water splitting in alkaline solution (in preparation).
- [3] Shaowei Song, Stainless-steel (SS) based efficient oxygen evolution reaction catalysts towards potential commercialization (in preparation).
- [4] Shaowei Song, Jun Mao, Mitchell Bordelon, Ran He, Yumei Wang, Jing Shuai, Jingying Sun, Xiaobo Lei, Zhensong Ren, Shuo Chen, Stephen Wilson, Kornelius Nielsch, Qinyong Zhang, Zhifeng Ren, Joint effect of magnesium and yttrium on enhancing thermoelectric properties of n-type Zintl $\text{Mg}_{3+\delta}\text{Y}_{0.02}\text{Sb}_{1.5}\text{Bi}_{0.5}$, *Materials Today Physics* 2019, 8, 25.
- [5] Shaowei Song, Jun Mao, Jing Shuai, Hangtian Zhu, Zhensong Ren, Udara Saparamadu, Zhongjia Tang, Bo Wang, Zhifeng Ren, Study on anisotropy of n-type Mg_3Sb_2 -based thermoelectric materials, *Applied Physics Letters* 2018, 112, 092103.
- [6] Qing Zhu, Shaowei Song, Hangtian Zhu, Zhifeng Ren, Realizing high conversion efficiency of Mg_3Sb_2 -based thermoelectric materials, *Journal of Power Sources* 2019, 414, 393.

- [7] Ting Zhou, Jun Mao, Jing Jiang, Shaowei Song, Hangtian Zhu, Qing Zhu, Qinyong Zhang, Wuyang Ren, Zhiming Wang, Chao Wang, Zhifeng Ren, Large reduction of thermal conductivity leading to enhanced thermoelectric performance in p-type $\text{Mg}_3\text{Bi}_{2-y}\text{Mg}_2\text{Bi}_y$ solid solutions, *Journal of Materials Chemistry C* 2019, 7, 434.
- [8] Jun Mao, Yixuan Wu, Shaowei Song, Jing Shuai, Zihang Liu, Yanzhong Pei, Zhifeng Ren, Anomalous electrical conductivity of n-type Te-doped $\text{Mg}_{3.2}\text{Sb}_{1.5}\text{Bi}_{0.5}$, *Materials Today Physics* 2017, 3, 1.
- [9] Jing Shuai, Binghui Ge, Jun Mao, Shaowei Song, Yumei Wang, Zhifeng Ren, Significant role of Mg stoichiometry in designing high thermoelectric performance for $\text{Mg}_3(\text{Sb},\text{Bi})_2$ -based n-type Zintl, *Journal of American Chemical Society* 2018, 140, 1910.
- [10] Zhensong Ren, Jing Shuai, Jun Mao, Qing Zhu, Shaowei Song, Yizhou Ni, Shuo Chen, Significantly enhanced thermoelectric properties of p-type Mg_3Sb_2 via co-doping of Na and Zn, *Acta Materialia* 2018, 143, 265.
- [11] Jun Mao, Jing Shuai, Shaowei Song, Yixuan Wu, Rebecca Dally, Jiawei Zhou, Zihang Liu, Jifeng Sun, Qinyong Zhang, Clarina dela Cruz, Stephen Wilson, Yanzhong Pei, David J. Singh, Gang Chen, Ching-Wu Chu, Zhifeng Ren, Manipulation of ionized impurity scattering for achieving high thermoelectric performance in n-type Mg_3Sb_2 -based materials, *Proceedings of the National Academy of Sciences* 2017, 114, 10548.
- [12] Jun Mao, Yixuan Wu, Shaowei Song, Qing Zhu, Jing Shuai, Zihang Liu, Yanzhong Pei, Zhifeng Ren, Defect engineering for realizing high thermoelectric performance in n-type Mg_3Sb_2 -based materials, *ACS Energy Letters* 2017, 2, 2245.

- [13] Jing Shuai, Jun Mao, Shaowei Song, Qinyong Zhang, Gang Chen, Zhifeng Ren, Recent progress and future challenges on thermoelectric Zintl materials, *Materials Today Physics* 2017, 1, 74.
- [14] Jing Shuai, Jun Mao, Shaowei Song, Qing Zhu, Jifeng Sun, Yumei Wang, Ran He, Jiawei Zhou, Gang Chen, David J. Singh, Zhifeng Ren, Tuning the carrier scattering mechanism to effectively improve the thermoelectric properties, *Energy Environmental Science* 2017, 10, 799.
- [15] Udara Saparamadu, Johannes de Boor, Jun Mao, Shaowei Song, Fei Tian, Weishu Liu, Qinyong Zhang, Zhifeng Ren, Comparative studies on thermoelectric properties of p-type $\text{Mg}_2\text{Sn}_{0.75}\text{Ge}_{0.25}$ doped with lithium, sodium, and gallium, *Acta Materialia* 2017, 141, 154.
- [16] Udara Saparamadu, Jun Mao, Keshab Dahal, Hao Zhang, Fei Tian, Shaowei Song, Weishu Liu, Zhifeng Ren, The effect of charge carrier and doping site on thermoelectric properties of $\text{Mg}_2\text{Sn}_{0.75}\text{Ge}_{0.25}$, *Acta Materialia* 2017, 124, 528.

